Remote Optical Detection of Uranium and Plant Response to Uranium Exposure

by

Lauren A. Ibon

A dissertation submitted in partial fulfillment
of the requirements for the degree of
Doctor of Philosophy
(Nuclear Engineering and Radiological Sciences)
in The University of Michigan
2022

Doctoral Committee:

Professor Igor Jovanovic, Chair
Associate Professor Gretchen Keppel-Aleks
Professor Alec Thomas
Doctor Laura Tovo, Savannah River National Laboratory

Lauren A. Ibon
lafinney@umich.edu
ORCID ID: 0000-0002-1811-4968

ACKNOWLEDGEMENTS

I would like to thank my advisor, Professor Igor Jovanovic. Your guidance, advice, and encouragement helped me prosper as scientist and deepen my knowledge and enjoyment of research. I appreciate all of the lessons, opportunities, and support over the past five years which help me navigate to where I am today. I would also like to thank my committee members, Professor Alec Thomas, Professor Gretchen Keppel-Aleks, and Dr. Laura Tovo, for advice, encouragement, and fruitful discussions which have improved my understanding and the impact of my work. I thank Dr. Miloš Burger, who provided experimental guidance since the beginning of my graduate studies. I would like to thank Dr. Patrick Skrodzki, whose friendship and mentorship encouraged me from my first year of graduate school, and also provided experimental assistance over the years. I thank John Nees for his contributions to my understanding of laser science and constant willingness to help with experiments as needed. I would also like to thank Dr. Sivanandan Harilal for his assistance in the work on single-shot, standoff detection of uranium via FIBS.

I would also like to thank two of my mentors in my undergraduate studies, Professor Tessa Calhoun from the Chemistry Department and Professor David Donovan from the Nuclear Engineering Department at the University of Tennessee, for believing in my abilities as a scientist and encouraging me to attend graduate school. Both of your guidance and kind words have stuck with me, and inspired me through out the past five years. I would like to thank Xuan Xiao, Felicia Sutanto, Tingshiuan Wu, Nicholas Peskosky, Jinpu Lin, and Lonnie Garrett for their friendship and support. I

would like to thank Nicholas Peskosky for his contributions to laser maintenance that was pertinent to my plant monitoring work. I would like to thank Jinpu Lin for his assistance in the genetic algorithm work and contributions to data interpretation from filament optimization experiments. I thank Cassara Higgins and Professors Frederic Poineau, David Hatchett, and Ken Czerwinski at the University of Nevada Las Vegas for providing uranyl nitrate for the biota-stress work. I thank Dr. Wendy Kuhne for fruitful discussions on uranium exposure in biota.

I would like to thank my friends I have met in the department who continually supported me. I would like to thank my family, in particular, my parents – Larry and Barbara Finney – who always encouraged me to pursue my passions. Lastly, I would like to thank my husband, Matthew Ibon, for being by my side through all of the ups and downs.

I thank also the funding sources which made this research possible. My research was supported by the National Science Foundation Graduate Research Fellowship Program (DGE 1256260). The work presented in this dissertation was partially supported by the Consortium for Verification Technology (DE-NA0002534) and Consortium for Monitoring, Verification, and Technology (DE-NE000863) sponsored by the Department of Energy National Nuclear Security Administration as well as the Air Force Office of Scientific Research (AFOSR) FA9550-16-1-0121 and the Department of Defense, Defense Threat Reduction Agency (HDTRA1-20-2-0002).

TABLE OF CONTENTS

LIST OF FIGURES

Figure

LIST OF TABLES

Table

LIST OF ABBREVIATIONS

BBO β-$Ba(BO_2)_2$

CCD charge-coupled devices

ChlF chlorophyll fluorescence

CMOS complementary metal-oxide-semiconductor

CPA chirped-pulse amplification

DM deformable mirror

DU depleted uranium

EM-ICCD electron-multiplying intensified charge-coupled device

FIBS filament-induced breakdown spectroscopy

F-IF filament-induced fluorescence

FOM figure of merit

fs femtosecond

FWHM full-width at half-maximum

GA genetic algorithm

ICCD intensified charge-coupled device

LA laser ablation

LIBS laser-induced breakdown spectroscopy

LIDAR light detection and ranging

LIF laser-induced fluorescence

LPP laser-produced plasma

LTE local thermal equilibrium

NPQ nonphotochemical quenching

ns nanosecond

OES optical emission spectroscopy

OPA optical parametric amplifier

PQ photochemical quenching

ps picosecond

PAM-F pulse amplitude modulated fluorometry

PMT photomultiplier tubes

ROC Receiver operating characteristic

SBR signal-to-background ratio

SIF solar-induced fluorescence

SLM spatial light modulator

SPM self-phase modulation

ABSTRACT

Ultrafast laser-based spectroscopy is of interest for nuclear nonproliferation monitoring because it holds promise for in-field, rapid, and remote detection of nuclear materials. One of its features is the ability to elicit atomic and molecular signatures from solids, liquids, and gases. Because optical spectroscopy is not reliant on radioactive decay, both the radioactive and nonradioactive materials can be detected. The existence of atomic and molecular isotope shift can also offer isotopic sensitivity. Lastly, at high peak powers, ultrafast lasers can undergo filamentation, which can enable optical excitation at long distances. One challenge with generation of filaments at high peak powers is the formation of multiple competing filaments that can be seeded by beam aberrations or, in general, its amplitude and phase structure. This work investigates the properties of filaments in the multi-filament regime via non-invasive optical emission spectroscopy (OES). The spatiotemporal molecular transitions and excitation/ionization mechanisms that occur are described. A genetic algorithm (GA) is used to manipulate the beam spatial phase and, therefore, the resulting multi-filament structure such that the filament-induced breakdown spectroscopy (FIBS) signal generation is optimized. FIBS is demonstrated for single-shot detection of uranium atomic and molecular spectral features that could also be suitable for measurements with isotopic discrimination.

While direct detection of uranium is indispensable, there has been recent interest in using plants' response to their environment as an indirect sensor of nuclear activity. Current techniques used in-field to monitor plant health are either limited in their measurement distance or are significantly inhibited by large solar background. The

use of pulsed laser-based methods provides a distinct time structure that accompanies optical signatures and also allows for powerful background rejection when used in conjunction with gated detectors. Filament-induced fluorescence (F-IF) is used for the first time to excite chlorophyll fluorescence (ChlF) in green algae, and the temporal profile is found to be a distinguishing characteristic between healthy and uranium-exposed samples. It is extrapolated from the experimental results that remote discrimination of uranium-exposed algae can be achieved up to 125 m within a $\sim$1-s measurement time. Ultrashort pulse duration lasers enable resolution of rapid molecular dynamics which influence the fluorescence lifetime. Specifically, two primary nonphotochemical quenching (NPQ) mechanisms that alter the fluorescence lifetime can be interrogated via pump-probe transient absorption spectroscopy. The design, construction, and characterization of the system is discussed, and the predicted observation is presented based on the previous results from F-IF of uranium-exposed algae. This work further strengthens the case for the use laser-based spectroscopy, including the special case of filament-induced breakdown spectroscopy, for nuclear nonproliferation measurements and more broadly in environmental monitoring.

CHAPTER 1

Nuclear Material Detection for Nonproliferation and Security

1.1 Introduction

Detection of nuclear materials is a serious societal concern due to national security and energy implications. Most commonly used for safeguards and treaty verification purposes are ionizing radiation detectors, which can be used to detect atoms that undergo nuclear decay. Ionizing radiation detection typically offers isotope sensitivity, but is fundamentally constrained by the fact that it can only be employed for identification of radioactive materials. Furthermore, ionizing radiation is limited in the distance it can propagate from the source in air. Laser-based methods, on the other hand, offer several benefits that could potentially overcome these challenges. One such benefit is that lasers can excite signatures characteristic of isotopes, atoms, and molecules. High repetition rates of pulsed laser systems facilitate rapid measurement times. Lastly, the use of ultrashort laser pulses with femtosecond (fs) durations at high intensities enables remote excitation of optical signatures through a process called filamentation. Filaments are a subject of active research due to their complex physics and potential wide application space. The major variants of laser-based spectroscopy discussed in this dissertation are laser-induced breakdown spectroscopy

(LIBS) and laser-induced fluorescence (LIF), and their filamentation counterparts, where the filament is used to induce breakdown or fluorescence. This dissertation presents a study of the fundamental properties of filaments at high peak powers needed for remote sensing, as well as the use of filaments for detection and excitation of various materials, such as metallic uranium, metallic copper, and plants.

1.2 Nuclear nonproliferation and security

Since the development and use of nuclear weapons in World War II, there has been an international urgency for monitoring nuclear activities. Although nuclear materials have the disturbing potential for use in international conflicts, they have also found widespread use in energy production and medical diagnostics and treatment. For example, nuclear energy production contributes to approximately 20% of the total U.S. energy production [4], and is one of the most promising ways to generate reliable and carbon-free energy [140]. In the medical field, ionizing radiation is used to identify and treat different illnesses, one of the most well-known being cancer. It is necessary, therefore, to have appropriate verification and safeguards measures in place to ensure there is no illicit diversion or use of nuclear materials. The International Atomic Energy Agency (IAEA) and the Treaty on the Nonproliferation of Nuclear Weapons, or Nonproliferation Treaty (NPT), are two major agreements put in place to promote nuclear science while prohibiting the development and testing of nuclear weapons. In particular, the NPT was drawn with the goal of total nuclear weapons disarmament. The known nuclear weapons states that have agreed to no longer test nuclear weapons are the United States, Russia, United Kingdom, France, and China. However, there are several other countries, such as Pakistan, India, and North Korea, that have developed and tested nuclear weapons and have not signed the NPT [180]. Their continued nuclear proliferation-prone activities motivate the continued advancement in nuclear activity monitoring technologies. Tracking the clandestine enrichment,

transportation, and use of nuclear materials is crucial for ensuring their peaceful use. One concern is establishing a system that accounts for the enrichment uranium in U-235 from mined naturally occurring uranium. U-235 is the fissile isotope used in nuclear fuel and weapons and makes up approximately 0.7% of natural uranium. U-235 is commonly enriched via the centrifuge process since it is well-established and relatively inexpensive compared to other enrichment methods, such as gaseous diffusion [117]. The centrifuge enrichment process uses UF_6 gas, which has been shown to leak from facilities in small quantities [109]. UF_6 is highly reactive with water and is known to form uranyl fluoride (UO_2F_2) after interacting with water vapor in the atmosphere. Simulations predict that this compound can be found hundreds of kilometers away from the original site in varying concentrations, as shown in Fig. 1.1. Due to the low background concentration of UO_2F_2, it is promising as a signature of uranium enrichment activities.

Ionizing radiation methods commonly used for nuclear material detection rely on radioactive decay. To enhance the signal from weak or shielded sources, active interrogation methods are often employed [105]. Active interrogation sources for inducing fission of uranium include neutron sources that can propagate a few m [111, 115] and high-energy photons from linear accelerators [104], which are not portable. A serious drawback to these methods are that they do not provide molecular information specific to the enrichment process. None of the aforementioned methods are suitable for detecting the *molecular* structure of UO_2F_2.

Laser-based spectroscopy, on the other hand, can excite the atomic, molecular, and isotopic signatures. Laser-induced fluorescence of uranyl fluoride in the atmosphere could provide direct evidence for enrichment activities since the fluorescence signature is unique to this compound. Furthermore, LIBS is sensitive to the isotopic shift between U-235 and U-238 for ionic and atomic lines on the order of 5–10 pm [148] and molecular features on the order of 50 pm [86]. The versatility of optical spectroscopy

is one of its major benefits since it can be used for material identification, to explore the physics of LPPs including filament formation and evolution, and the atomic and molecular dynamics that governs the generation of identifiable features in the spectra. This dissertation examines the feasibility of direct filament excitation of uranium, and which controllable parameters can reduce the detection time. Furthermore, there has been recent interest in using plants' optical properties as indirect sensors of nuclear activity. Plants' high sensitivity to their growth conditions and environment make them promising for detecting low concentrations of materials. Understanding plants' response to uranium exposure and discerning potential signatures that can indicate uranium contamination in the environment is the second major topic studied in this dissertation.

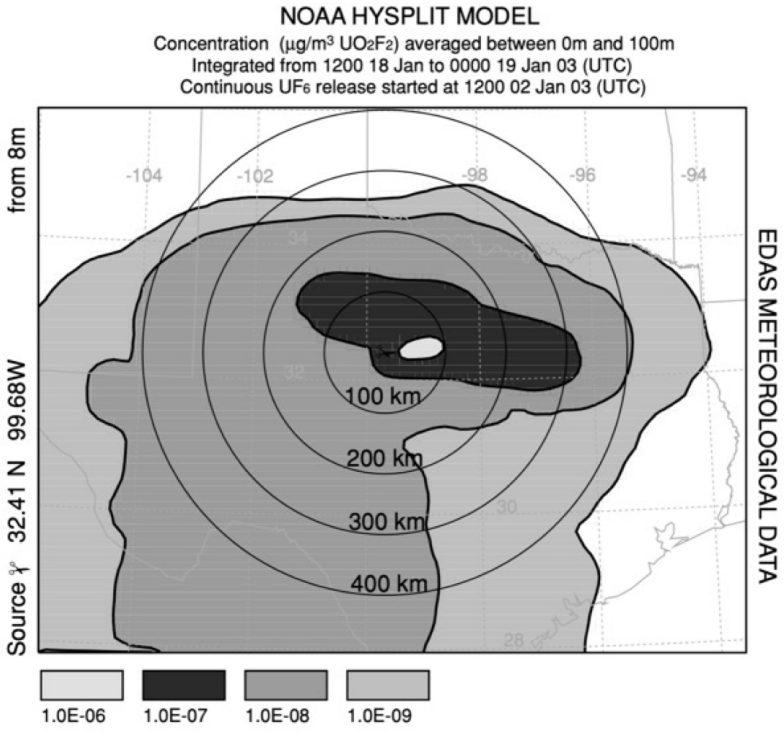

Figure 1.1: Map of UO_2F_2 concentration surrounding a centrifuge enrichment facility [109].

1.3 Remote laser-based spectroscopy for nuclear material detection

While there are many benefits of laser-based spectroscopy for detection of nuclear proliferation-relevant materials, there are also some challenges. One challenge is that laser beams are limited by diffraction in the distance at which they can deliver the laser energy with a high fluence. However, at high peak powers, a process known as filamentation can occur [22]. Filamentation is the formation of a confining plasma column in air which has been shown to extend as far as kilometers away from the laser source [154] with sufficient laser energy, and has enabled remote detection on the order of 100's m [155, 175]. This discovery enables active excitation of optical emission over large distances, exceeding that of ionizing radiation detection and active interrogation methods. However, at high peak powers needed for filamentation over great distances, instabilities, aberrations in the beam profile, and air turbulence lead to the breakup of a single filament core into multiple filaments. These multiple filaments are in competition with each other, making their formation rather sporadic in nature. Multiple filaments can influence the efficiency and reproducibility of signals produced via filament excitation of a target. This dissertation explores the properties of filaments in the multi-filament regime, and how the control of multi-filament structures can improve the analytical capabilities of filament-based spectroscopy.

There are two main methods studied in this dissertation, LIBS and LIF. Both rely on optical emission, either from a LPP or from de-excitation of molecules in a sample. The signatures observed with OES are inherently specific to a given atom or compound because the wavelength of the light emitted is determined by the gap between the two energy levels involved in a transition, and the electronic structure is unique for different elements and molecules. Atoms undergo electronic transitions, while molecules can undergo a combination of rotational, vibrational, and electronic

transitions. A distinct combination of wavelengths that appear in a spectrum are what allows for material identification. Additionally, the intensity of spectral features is generally proportional to the concentration of a species in the target material, which can enable quantitative measurements. Chapter 2 provides an in-depth overview of the foundations of LIBS and LIF. Briefly, with LIBS a laser is focused to a high intensity onto a surface in order to remove and/or excite a fraction of material in the form a luminous plasma. The emitted light is characteristic of the material composition. The environment of LPPs formed under different laser ablation conditions result in different time- and space-dependent spectral signatures. The intensity and width of spectral lines allow for temperatures and densities to be diagnosed, which can inform on the thermodynamic conditions that lead to species formation in LPPs.

Uranium is one of the main materials related to nuclear nonproliferation and security. The complexity of its optical emission spectrum makes its analysis arduous. It is a high-Z element, with many electronic transitions appearing as a dense set of spectral lines in the visible region of the spectrum [144]. Furthermore, uranium is highly reactive with oxygen, and the contribution of uranium oxide optical emission additionally complicates the spectrum with broad spectral background. Recent work presents the identification of UO_2 and U_xO_y as the origin of previously unknown spectral features [170, 171]. The results in this work aid in finding signatures that are most promising for in-field detection. Remote ns-LIBS of uranium has been demonstrated over $\sim$50 m [38]. In scenarios where the detection of undeclared activities is sought, the ability to have on-site access within 10's of m may not be achievable. Therefore, the use of FIBS needs to be further established in uranium detection. Previous work employing FIBS introduces the UO molecular emission at 593.55 nm as promising for isotopic measurements over standoff distances [86]. Here, the influence of filament formation conditions on the optical signatures observed upon uranium ablation is explored, as well as the ability of FIBS to remotely detect uranium.

LIF directly excites molecular signatures, which can be beneficial over LIBS when preserving the original molecular structure of the material is important. One example is the fluorescence of uranyl fluoride, which can indicate enrichment activities. Another is the fluorescence of chlorophyll, the main pigment involved in light capture for photosynthesis, which is often used to interrogate plant health and environmental surroundings [137, 138]. In this dissertation, the fluorescence of chlorophyll in live algae is investigated as a potential biosensor for uranium exposure. Current methods that use plants' optical properties for environmental monitoring are limited in their measurement distance or are significantly inhibited by large solar background, leading to long measurement times. LIF provides a pathway for active excitation of chlorophyll that can be employed over large distances and may improve detection. Furthermore, changes in plants' environment have been found to manifest in chlorophyll fluorescence lifetime [167, 195, 196]. Photosynthesis, the concentration of various pigments in the plant cell, chemical environment, and stress influence the chlorophyll fluorescence lifetime, and are investigated in this dissertation. Furthermore, LIF of chlorophyll may be beneficial over both ionizing radiation methods and the currently employed plant health monitoring methods due to the increased sensitivity and quick measurement times. The work presented herein explores the feasibility of filament-induced fluorescence (F-IF) for remote sensing applications in plant stress monitoring.

1.4 Dissertation structure

Each chapter in this dissertation consists of standalone contributions to the advancement of remote optical sensing of uranium and improving analytical capabilities of laser-based methods to support nuclear nonproliferation efforts. Chapter 2 and 3 provide guiding principles and a foundational overview of methods used in this dissertation. There are four chapters containing experimental development and results

that can be divided into two relevant topics: (1) investigation and manipulation of filaments under the multi-filament regime and direct detection of uranium and (2) indirect monitoring by investigating plants response to uranium exposure. Chapters 4 and 5 focus on the investigation of ultrafast-laser filaments, filament-induced breakdown spectroscopic signal enhancement, and determination of FIBS detection capabilities for uranium atomic and molecular signals. Chapter 6 explores the feasibility of fs-LIF and F-IF in distinguishing uranium exposure in plants. Chapter 7 presents the construction and characterization of an ultrafast transient absorption pump-probe spectroscopy experiment that will enable interrogation of specific quenching mechanisms that influence the observed fluorescence parameters in Chapter 6. Understanding these quenching mechanisms may help determine how uranium exposure manifests in plants' optical properties. The experiments presented in this dissertation were conducted at the University of Michigan in facilities of the Gérard Morou Center for Ultrafast Optical Science. Chapter 8 provides a conclusion, presents potential opportunities to expand on the work, and discusses the scaling this work from a laboratory setting to in-field technology. This dissertation compiles the results from the following recent publications along with results that have yet to be published:

[61] L. A. Finney, N. Peskosky, P. J. Skrodzki, M. Burger, J. Nees, K. Krushelnick, and I. Jovanovic. Identification of stress in plants via femtosecond laser-induced fluorescence and steady-state absorption spectroscopy. *2021 Institute for Nuclear Materials Management Join Meeting & European Safeguards Research and Development Association*, 1–8, 2021.

[60] L. A. Finney, J. Lin, P. J. Skrodzki, M. Burger, J. Nees, K. Krushelnick, and I. Jovanovic. Filament-induced breakdown spectroscopy signal enhancement using optical wavefront control. *Optics Communications*, 490(126902)1–5, 2021.

[24] M. Burger, L. A. Finney, L. Garrett, S. S. Harilal, K. C. Hartig, J. Nees, P.

J.Skrodzki, X. Xiao, and I. Jovanovic. Laser ablation spectrometry for studies of uranium plasmas, reactor monitoring, and spent fuel safety. *Spectrochimica Acta Part B: Atomic Spectroscopy*, 179:106095, 2021.

[62] L. A. Finney, P. J. Skrodzki, M. Burger, J. Nees, S. S. Harilal, and I. Jovanovic. Single-shot, multi-signature remote detection of uranium by filament-induced breakdown spectroscopy. *Optics Letters*, 44(11):2783–2786, 2019.

[64] L. A. Finney, P. J. Skrodzki, M. Burger, X. Xiao, J. Nees, and I. Jovanovic. Optical emission from ultrafast laser filament-produced air plasmas in the multiple filament regime. *Optics Express*, 26(22):29110–29122, 2018.

CHAPTER 2

Laser-Based Spectroscopy

This dissertation describes the use of two laser-based optical techniques, laser-induced breakdown spectroscopy (LIBS) and laser-induced fluorescence (LIF), that were used to excite solid and liquid targets. Both the laser ablation (LA) and nondestructive excitation via LIF are introduced in this chapter, together with the fundamental background on optical transitions. The parameters that dictate properties of LPPs, such as the pulse duration of the laser used for LA or atmospheric conditions, are discussed. The remote counterparts to LIBS and LIF require ultrafast laser filamentation, and thus the physics behind filament formation is also introduced. Experimental design considerations for different optical spectroscopy techniques are discussed. Lastly, the spectroscopy of uranium and the associated challenges are introduced as a motivation for a fraction of the studies presented in this dissertation.

2.1 Introduction to laser ablation and optical spectroscopy

2.1.1 Fundamentals of optical transitions

Optical transitions occur in essentially all materials. The term "optical" refers to electromagnetic radiation that has a wavelength between the ultraviolet and the infrared, or from ∼100 nm to ∼1 µm. Photons in this wavelength range can excite electrons to populate a higher energy level depending on the electronic structure of

the material. The opposite effect can also occur if a material already has electrons in an excited state, where photons are emitted upon de-excitation. The wavelength (λ_γ), or frequency (ν_γ), of radiation required to excite an electron from a lower level to a higher level is

$$h\nu_\gamma = \frac{hc}{\lambda_\gamma} = E_{\text{upper}} - E_{\text{lower}}, \tag{2.1}$$

where E is the energy of the upper or lower excited state, h is Planck's constant, and c is the speed of light. Transitions can be rotational, vibrational, or electronic. Atoms are only able to undergo electronic transitions, whereas molecules can also support rotational and vibrational transitions. Transitions are "allowed" to occur if the selection rules based on quantum mechanics are met. Quantum numbers are assigned to every electron in a given state, and no electron in a single system can have the same set of quantum numbers according to the Pauli exclusion principle. The primary quantum numbers are n, ℓ, m_ℓ, and m_s, where n is the principal quantum number that defines the electron shell or energy level, ℓ is the orbital angular momentum quantum number which can be 0 up to $n-1$, m_ℓ is the magnetic quantum number which can range from $-\ell$ to ℓ, m_s is the spin quantum number which can range from $-s$ to s, and s is the spin associated with a given subshell. There is further a total angular momentum quantum number, j, defined as $|\ell - s|$. The total angular momentum J can then be calculated from $\hbar^2 j(j+1)$. As an example, the first atomic orbital is the "s" orbital, where $n = 0$, and therefore $\ell = 0$, $m_\ell = 0$, and two electrons can occupy this orbital, one with $m_s = 1/2$ and the other with $m_s = -1/2$.

For atomic transitions, the selection rules are (1) the total spin cannot change, (2) the change in orbital angular momentum can be 0, -1, or $+1$, but the transition from $\ell = 0$ to $\ell = 0$ is forbidden, (3) the change in total angular momentum J must be 0, -1, or $+1$, but the transition $J = 0$ to $J = 0$ is not allowed, and (4) the initial and final wavefunctions must change parity. For molecules, there are additional selection rules. Transitions that follow the selection rules are considered "allowed", meaning

that there is a high probability that they will occur. "Forbidden" transitions have a calculable probability of occurring; however, this probability is very small. Transition probability is determined by first calculating the transition dipole moment, defined as

$$M_{u,\ell} = \int \Psi_u \vec{\mu} \Psi_\ell, \tag{2.2}$$

where Ψ_u is the wavefunction for the upper level, Ψ_ℓ is the wavefunction for the lower level, and $\vec{\mu}$ is the electric dipole moment operator. The probability of the transition can be calculated as $|M_{u,\ell}|^2$.

While atoms can only undergo electronic transitions, molecules can have rotational and vibrational transitions governed by the coupling of atomic orbitals when they form a bond. Molecular energy levels are represented by the harmonic oscillator in the ideal case, but more realistically can be described by the anharmonic oscillator, which takes into account the dissociation of bonds. This anharmonic oscillator is referred to as the "Morse potential well". Figure 2.1(a) shows an example two-tier diatomic molecular energy level diagram. Two electronic levels are shown in Fig. 2.1(a); the vibrational levels are labeled, and there are rotational levels within those vibrational states. Depending on the molecule, different types of rotations and vibrations can occur.

With high resolution instruments, the fine lines from molecular vibrational and rotational transitions can be observed via OES; however, with poorer resolution instrumentation, they appear as broad features. An example optical emission spectrum for N_2 is shown in Fig. 2.1(b), measured from optical emission in air upon excitation with ultrafast laser-induced plasma column [64]. The labels are denoted as (x_u, x_ℓ), where highest intensity peaks are the bandheads of the electronic transitions from the specified vibrational level of the upper electronic state (x_u) to the vibrational level of the lower electronic state (x_ℓ). The fine rotational transitions can be seen in the lower wavelengths from the main bandhead vibronic transition. In many-atom molecules,

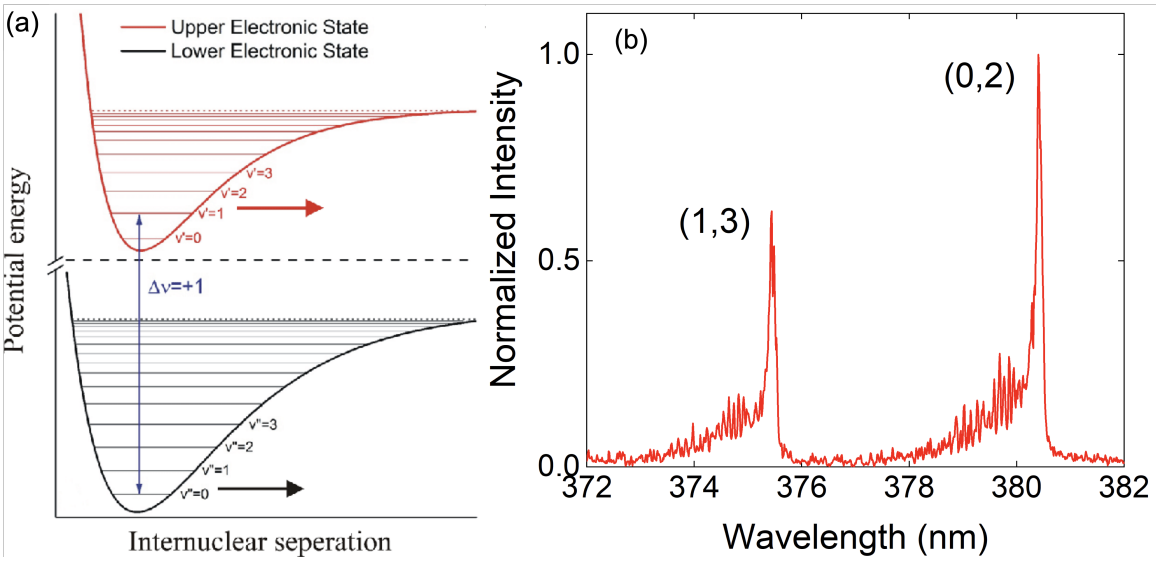

Figure 2.1: (a) Example energy level schematic for a diatomic molecule [81]; (b) N_2 molecular optical emission spectra upon excitation in air via ultrafast laser filamentation, adapted from Ref. [64].

there are more rotational degrees of freedom that can complicate the optical emission spectrum. The following section introduces the methods and background for forming of LPPs and their properties.

2.1.2 Principles of laser ablation

Laser ablation (LA) has been of interest over the past several decades due to its broad application space including pulsed-laser deposition of nanofilms, LIBS, micromachining, and medical science. It is a multi-faceted process in which the laser intensity is high enough to cause optical breakdown, heating, excitation, and removal of material from a surface. The ablation process depends on the material being irradiated and the pulse duration of the laser used. Here, the focus is primarily on solid metal and semiconductor materials. In general, ablation consists of energy absorption by free electrons on the surface, thermal vaporization, and energy transfer in the material lattice [36, 81]. The intense thermalization and energy absorption lead to removal of material from the surface in the form of excited electrons, ions,

and clusters that form a dynamic micro-plasma. In most cases, these plasmas are characterized by their electron temperature (T_e). The magnitude of thermalization, or thermal diffusion length (l_{th}), is dependent on the pulse-duration of the laser used:

$$l_{th} = 2\sqrt{D\tau_p}, \tag{2.3}$$

where τ_p is the pulse duration and D is the thermal diffusivity [134]. The thermal effects vary significantly depending on the pulse duration, especially between nanosecond (ns) and fs pulses, because the electron cooling time (τ_e) for most metals is on the order of a picosecond (ps), which is much longer than the fs pulse duration [36].

With ns-LA, there is significant damage due to thermal and nonthermal heating of the material. First, the laser pulse causes melting of the surface and eventually reaches vaporization temperature. After this, the plasma begins to form while the laser pulse is still actively irradiating the target, which leads to heating of the LPP [81]. Once the laser pulse passes, there are interactions between the plasma and ambient atmosphere, confinement of the plasma, shockwave expansion, and plasma cooling. Finally, around 500 ns–1 µs after the laser pulse, the plasma enters the LIBS-regime, in which the ions, excited atoms, and molecules in the plasma are able to undergo recombination and de-excitation, which leads to the emission of light. For ultrashort pulses, $\lesssim$ps durations, the process of ablation is different, and the LIBS-regime is accessible much sooner after the laser pulse arrives. There are essentially negligible thermal heating effects, and the initial breakdown occurs through inverse bremsstrahlung absorption, multiphoton absorption, and Coulomb explosion [82], *i.e.*, direct solid to vapor transition. At this point, plasma formation, expansion, and cooling occur. Approximately 10's of ns after the laser pulse, the plasma enters the LIBS-regime. Since ns-LPPs interact with the laser pulse during plasma formation, the plasmas are much hotter than those

produced by ultrashort pulses. This results in different plasma expansion dynamics and LIBS spectra. There is a dynamic interplay between radiative and non-radiative processes that lead to plasma formation and plasma expansion. These differences in plume and shockwave expansion are determined to be a result of Coulomb explosion for fs-LA and increased rate of elastic collisions in ns-LPPs. More information on the formalism that describes these processes can be found in Refs. [30, 36, 134].

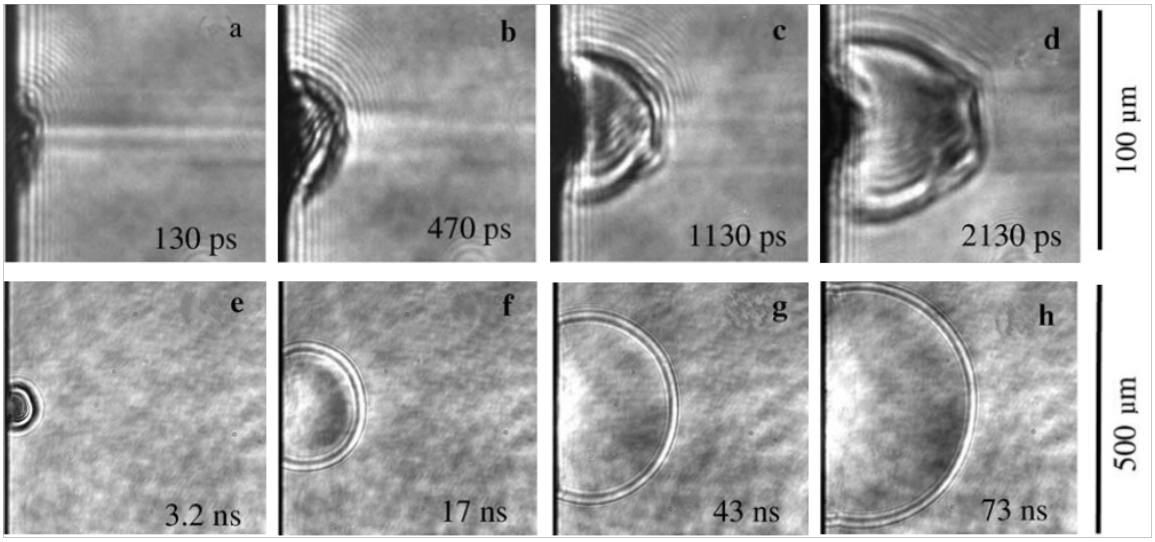

Figure 2.2: Plasma expansion after fs-LA of silicon (a–d) and ns-LA of silicon (e–h) adapted from Ref. [202].

Many previous studies investigated the plasma expansion through shadowgraphy, such as that shown in Fig. 2.2. Shadowgraphy employs a probing light source that backlights the plasma, and this transmitted light is imaged onto a camera. The interference that the probe experiences by passing through the LPP results in a "shadow"-like image since the plasma has a different refractive index than its surroundings. Time-resolved shadowgraphy allows for the expansion dynamics to be studied under different atmospheric conditions, ablation conditions, and in different materials. In general, it is found that LPP plume size (L) follows either the drag model [79, 80], $L = A - B\exp(Ct)$, and the spherical blast-Sedov model [163, 199], $L = At^{2/5}$, where t is time, while A, B, and C are shape parameters found through

fitting. Along with the plasma plume is the formation of a shockwave which confines the plasma. The time-dependent shockwave radius, $R(t)$, as it expands is defined by

$$R(t) = \left(\frac{E_d}{K(\gamma)\rho_0} \right)^{\frac{1}{2+\xi}} t^{\frac{2}{2+\xi}} \tag{2.4}$$

where E_d is the detonation energy, $K(\gamma)$ is a constant dependent on the specific heat of the ambient gas, γ, ρ_0 is the initial ambient gas density, and ξ is the geometrical parameter, where $\xi = 1$, 2, and 3 for a plane wave, cylindrical wave, and spherical wave, respectively [30]. In general for LA plumes, the plasma and shockwave is assumed to have a spherical geometry, as shown in Fig. 2.2. However, it is not always the case that the shockwave has a perfectly spherical geometry, as it is influenced by several factors such as the material, matrix effects, chemistry in the plasma plume, and laser fluence. For example, previous work has found that with fs-LA, there is a preferential expansion in the direction of the target normal where as for ns-LA it is generally observed to see greater lateral expansion of the plume [79]. The expansion of shockwaves and the information retrievable from their dynamics is an area of ongoing study for fundamental physics and modeling of large-scale explosions. In the next subsection, optical spectroscopy and diagnostic methods of LPPs are discussed.

2.1.3 Optical emission spectra of laser-produced plasmas

Plasma formation and shockwave expansion processes differ in ns- and fs-LA. The plasma formation conditions also influence the optical emission spectrum and its time-dependent dynamics. Figure 2.3 shows a general depiction of when optical signatures of different species can be observed. In ns-LA, continuum emission is observed at early times, immediately after the laser pulse arrives on the sample due to the high initial temperature of the plasma. Continuum is a result of bremsstrahlung and recombination of free electrons and can be nearly described by the Boltzmann

distribution:

$$B_\nu(T) = \frac{2\nu^2}{c^2} \frac{h\nu}{e^{h\nu/kT} - 1}, \tag{2.5}$$

where B_ν is the light intensity at a given frequency ν, c is the speed of light, h is Planck's constant, k is Boltzmann's constant of 1.38×10^{-23} J/K or 8.62×10^{-5} eV/K, and T is the temperature [9]. Due to the laser pulse interacting with the plasma during ns-LA, the initial temperatures are significantly higher, resulting in more persistent and higher intensity broadband radiation. However, for fs-LA, this broadband emission is much less intense and lasts much shorter. Depending on the application, fs-LA may be preferred over ns-LA for this reason, where minimizing the continuum and background during a measurement is preferred. As the plasma expands and cools, optical emission from ions can be observed, followed by atoms, and finally molecular optical emission can be seen once the plasma is sufficiently cool.

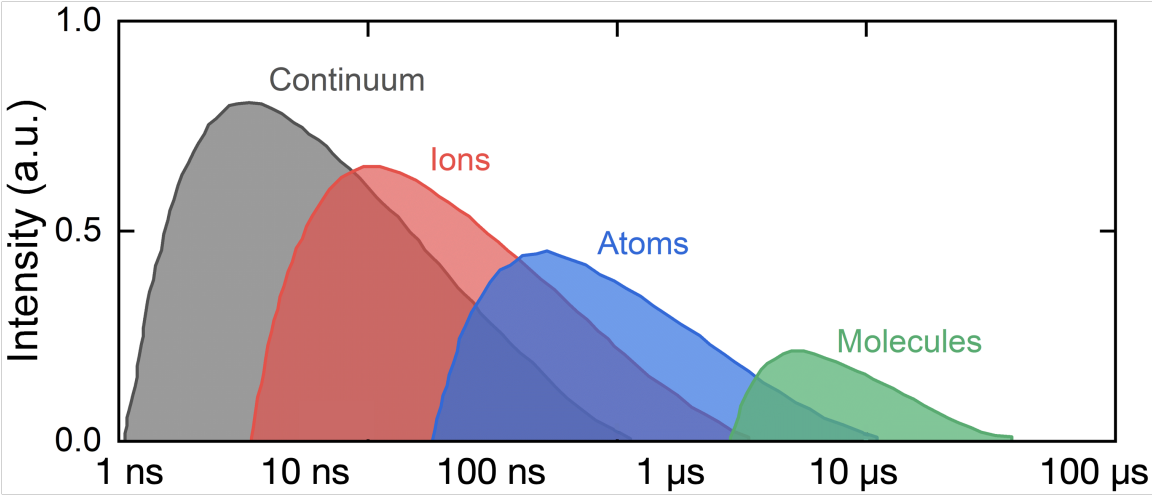

Figure 2.3: General timescale for continuum emission in the plasma: ionic optical emission begins when the plasma is sufficiently cool and starts to recombine. This is followed by atomic and molecular emission, as the molecules form at the latest stage of plasma expansion and cooling.

The observed optical emission spectrum can provide information about the target being ablated because the light emitted by the LPP is representative of the material's constituents. This makes LIBS a promising technique for trace material detection,

as the presence of explosive or pollutant signatures in the spectrum at known wavelengths can be used to distinguish it from a background. For example, two well-known features in the uranium optical emission spectrum appear at 591.54 nm and 593.55 nm; the appearance of peaks at these two wavelengths can be used to identify the presence of uranium. Another application of LIBS are the studies of plasma chemistry in controlled environments. Many studies have used LIBS as a surrogate for large-scale explosions [190, 191], including nuclear explosions and the production of surrogate signatures for nuclear forensics studies [83, 86, 192]. In many cases, it is beneficial to understand the conditions under which different species form, as well as their temporal structure. The following subsection introduces several of the common plasma diagnostic methods.

2.1.4 Plasma diagnostic techniques

There are two properties used to diagnose plasmas, their electron temperature (T_e) and their electron density (n_e). For LPPs, which usually have initial temperatures on the order of 10^4 K, the most common analysis methods to extract T_e and n_e from the optical emission spectrum are are based on the Boltzmann line distributions and Stark broadening effects.

The previously discussed Boltzmann distribution describes the shape and temperature dependence of the continuum emission that appears early during the LPP formation. The line intensities, which correspond to the population of electrons transitioning between states, can provide the information on the plasma temperature. For a single species in the plasma, *i.e.*, atomic transitions of a single element, the plasma temperature can be found from

$$I_{u,\ell}\lambda_{u,\ell} = \frac{n}{U(T)} A_{u,\ell} g_u \exp\left(-\frac{E_u}{kT}\right), \tag{2.6}$$

where $I_{u,\ell}$ is the line intensity of a transition from an upper level u to a lower level ℓ, λ is the wavelength of light emitted during the transition, n is the plasma density, $U(T)$ is the partition function for the emitting species, $A_{u,\ell}$ is the transition rate (Einstein's coefficient), g_u is the degeneracy of the upper excited state, k is Boltzmann's constant, and T is the plasma temperature. Most of these values are known from the experimental measurement or can be found in databases, such as the NIST atomic spectral database [113]. Upon rearranging Eq. 2.6, the equation takes the form of a linear function, $y = mx + b$:

$$\ln\left(\frac{I_{u,\ell}\lambda_{u,\ell}}{A_{u,\ell}g_u}\right) = -\frac{1}{kT}E_u + \frac{n}{U(T)}. \tag{2.7}$$

One can plot the left side of the equation, containing all known and calculable parameters as y and E_u as x, and the linear fit to this data yields the temperature. An example spectrum from a copper LPP is shown in Fig. 2.4(a), and a corresponding Boltzmann distribution is shown in (b), using atomic transitions found in the optical emission spectrum. It is important to note that the line intensity must be calibrated for the instrumental response, which takes into account the wavelength-dependent quantum efficiency of the optical sensor and the diffraction efficiency. With the slope of -1.30 ± 0.27 in Fig. 2.4(b), this results in a plasma temperature of $\sim$9000 K$\pm$2000 K. The error in these calculations can be large due to the rapidly transient nature of the LPPs. For example, the spectrum used for this Boltzmann plot was integrated over 1 µs, where the plasma is likely to have cooled and expanded significantly during this time. Shorter integration times reduce the error; however, this can introduce noise due to limited light collection. Furthermore, if the target material is a composition of multiple elements, each species have different heat capacities, which can result in multiple distinct temperatures calculated within the same plasma.

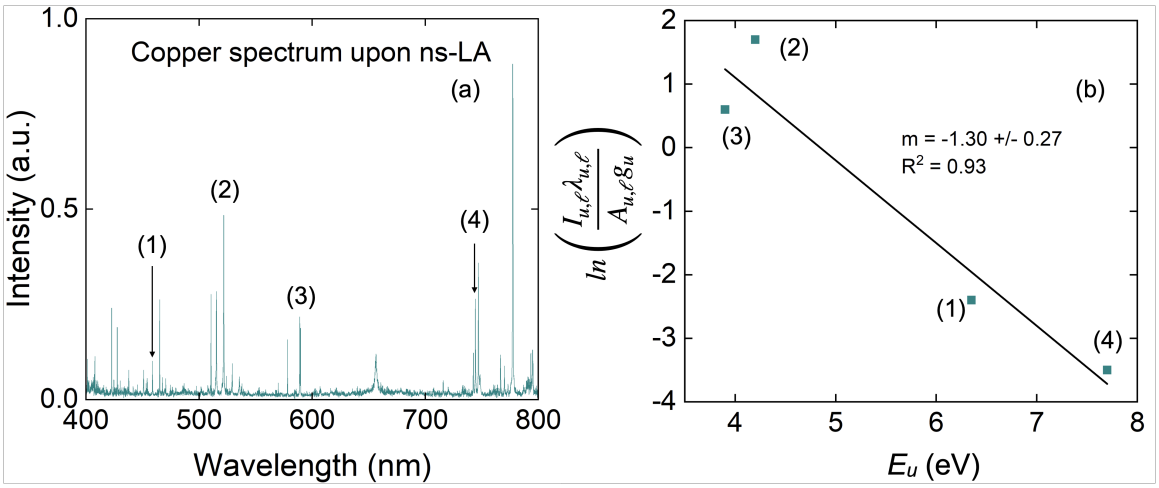

Figure 2.4: (a) Copper optical emission spectrum measured at a delay of 2 µs after ns-LA of a solid metal copper target, with 1 µs gate width. This spectrum is an average of 20 laser shots. (b) Boltzmann plot distribution using four of the known copper atomic lines found in the optical emission spectrum shown in (a).

In some cases, both ionic and atomic lines are visible in same time-integration window. Therefore, another approach is to calculate temperature with the Saha ionization equation. This equation describes the relationship between the ionization availability of a gas in thermal equilibrium at a given temperature and pressure, and the ionization state can be defined if the temperature and pressure are known:

$$\frac{n_{i+1}n_e}{n_i} = \frac{2}{\lambda^3}\frac{g_{i+1}}{g_i}\exp\left[-\frac{(\epsilon_{i+1}-\epsilon_i)}{kT}\right]. \tag{2.8}$$

Here, ϵ is the energy required to remove i electrons from a neutral atom, λ is the thermal de Broglie wavelength defined as $\sqrt{\frac{h^2}{2\pi m_e kT}}$, m_e is the mass of an electron, and the other variables are defined as above for Eq. (2.6). Both the Boltzmann and Saha equations assume local thermal equilibrium (LTE) for the plasma. LTE can be determined for a plasma given the McWhirter criterion is satisfied [75, 76]: $n_e \gtrsim 1.6\times10^{12}T_e^{1/2}(\Delta E)^3$, where ΔE is the largest gap between adjacent energy levels. In general, this criterion is used to justify the use of Saha-Boltzmann relationships in LPPs.

LTE is dependent primarily on the electron density at a given temperature. One of the most common ways to calculate the plasma density is the use of Stark broadening [75, 76]:

$$n_e = \left(\frac{\Delta\lambda_s}{2a}\right) \times 10^{16}\text{cm}^{-3} \tag{2.9}$$

where $\Delta\lambda_s$ is the Stark-broadened contribution to the full-width at half-maximum (FWHM) (nm) and a is the electron broadening parameter (nm) for that species at a particular wavelength. The Stark effect occurs as a result of spectral line splitting and shifting from the application of an external electric field. In the case of a plasma, this spectral broadening, often called Stark broadening or pressure broadening, results from charged particles in the plasma and is related to the plasma density. The direct width of an atomic line is the combination of multiple other broadening effects, including natural broadening, instrumental broadening, and Doppler (temperature) broadening. The Heisenberg's uncertainty principle defines the natural broadening and is generally considered to be negligible. Instrumental broadening can be measured directly with the same system that is used for experimental measurements and a known light source, such as a Hg-Ar lamp, to determine the wavelength-dependent instrumental broadening. Broadening from the Doppler effect, which occurs as a result of varying velocities of the emitting particles within the plasma, can be determined using the calculated plasma temperature:

$$\omega_{\text{Doppler}} = \sqrt{\frac{8kT\ln 2}{mc^2}}, \tag{2.10}$$

or simplified, $\omega_{\text{Doppler}} = 7.2 \times 10^{-7}\lambda_0\sqrt{T_e/M}$, where M is the mass of the emitter, and ω_{Doppler} is the contribution of Doppler broadening to the FWHM. As described previously, the temperature can be estimated from the optical emission spectrum; therefore, all contributions of broadening can be measured or calculated such that the remaining FWHM, after subtracting instrumental and Doppler broadening, is

$\Delta\lambda_s$ in Eq. 2.9. The total linewidth is measured as the FWHM of a Voigt fit to atomic spectral lines. Figure 2.5 shows a simulated example of line broadening effects and their respective shape. Instrumental and Doppler broadening are known to form a Gaussian distribution, Stark (pressure) broadening results in a Lorentz line shape, and the final spectral line shape is a Voigt function, which is a convolution of the Lorentz and Gaussian functions. Each is normalized in Fig. 2.5 so that the shape can be compared. For ns- and fs-LPPs, typical electron densities are in the range of $10^{17} - 10^{19}$ cm^{-3}, and is generally found to be large enough to consider LTE satisfied.

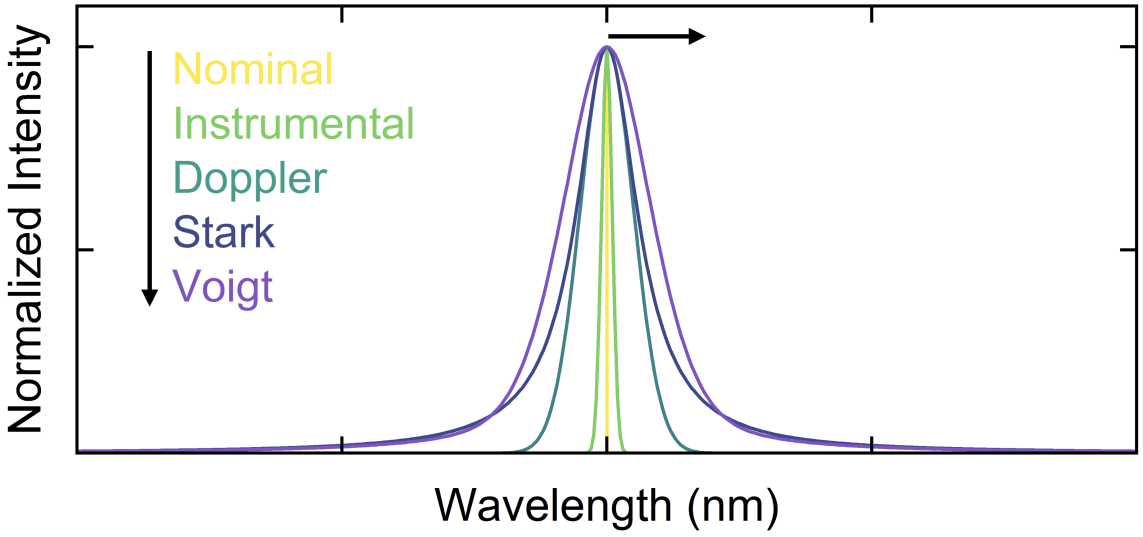

Figure 2.5: Simulated example of line broadening effects and their respective shape. The instrumental and Doppler broadening are shown with a Gaussian shape, while Stark (pressure) broadening is shown with a Lorentz shape. The Voigt distribution resembles a measured atomic spectral line in an optical emission spectrum.

2.1.5 Laser-induced fluorescence and absorption spectroscopy

Laser ablation is a destructive method, which inherently breaks down the integrity of a sample. This can result in loss of information, for example, the original molecular structure of the target material. For certain applications it is useful to retain molecular structure, in which case other techniques for measuring composition are preferred. One method commonly used is LIF. Fluorescence is a type of lumines-

cence, where upon exposure of a sample to light there is a corresponding immediate and rapidly decaying light emission from the sample. The characteristic difference between fluorescence and phosphorescence is that phosphorescence has a much longer lifetime than fluorescence. In other words, even after a material is no longer being illuminated, it will emit light due to the long lifetime of the excited state. Fluorescence lifetimes are on the order of ns and generally de-excite from a singlet state, whereas phosphorescence can last µs or longer, and de-excitation occurs from a triplet excited state [9].

In general, fluorescence is emitted at a longer wavelength than the light absorbed. This is because the emitted light is Stokes shifted, which occurs when non-radiative transitions happen prior to emission of a photon. Kasha's rule states that electrons de-excite to the lowest vibrational energy level after excitation, and therefore non-radiative decay from excited vibrational levels often occurs prior to fluorescence [9]. The fluorescence spectrum is a mirror image of the absorbance spectrum of a given molecule. The mirror image is due to the symmetric shape of the potential wells (anharmonic oscillator structure of molecular energy levels described previously) in the upper and lower electronic states. The Franck-Condon principle describes the magnitude of a vibronic transition, or simultaneous electronic and vibrational transition [9]. The magnitude is determined by the overlap integral, which is the amount of overlap over all space of the wavefunctions in two vibronic energy levels. An example is given in Fig. 2.6(a), where a photon excites an electron from (E_0, $v'' = 0$) to (E_1, $v' = 2$). The wavefunctions shown in the vibrational levels as sinusoidal functions have significant overlap, whereas the transition from (E_0, $v'' = 0$) to (E_1, $v' = 1$) is much less likely to occur because the wavefunction overlap is smaller. Figure 2.6(b) shows the manifestation of the difference in magnitude between the (E_0, $v'' = 0$) to (E_1, $v' = 1$) and (E_0, $v'' = 0$) to (E_1, $v' = 2$) transitions, where the magnitude of the latter is greater than the former. When non-radiative de-excitation from (E_1, $v' = 2$)

to (E_1, $v' = 0$) occurs, the greatest overlap for the wavefunction in the latter state appears with (E_0, v_2''). This results in mirrored absorption and emission, which is shown in Fig. 2.6(b).

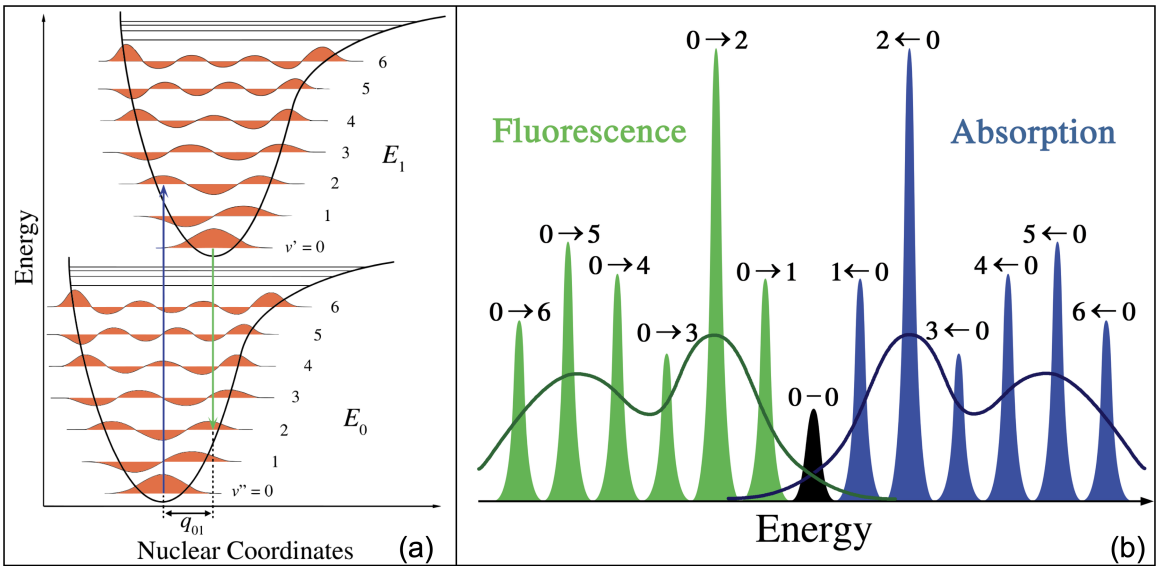

Figure 2.6: (a) Example Morse potentials for two electronic states with the wavefunctions for each vibrational level [160]. Transitions that have significant wavefunction overlap have a higher probability of occurring than those with minimal overlap. (b) Absorption and fluorescence spectra for the example given, demonstrating the mirror-image effect and Stokes shift upon de-excitation from higher vibronic energy levels to lower vibronic energy levels [161].

Analytical methods which employ fluorescence and absorbance spectroscopy can be preferred over LA since they inform on the molecular structure of a material. Fluorescence kinetics depend on the lifetime of a given excited state, and total quantum yield can be influenced by quenching parameters. Quenching can be a result of material concentration or other external factors, such as interactions with surrounding materials and chemical environment. Absorbance is directly related to the material concentration through the following relationship:

$$A = \epsilon\, b\, c = -\log(I/I_0), \tag{2.11}$$

where A is the absorbance, ϵ is the molar extinction coefficient that is wavelength

and molecule specific, b is the path length, and c is the concentration of the molecule being interrogated. A is also related to the total transmitted light, where I_0 is the initial light intensity and I is the transmitted light intensity. The parameters ϵ and b must be known to determine the concentration of a given molecule. Absorbance spectroscopy is not often used as an in-field technique, but it is a common lab-based analytical method that is frequently used to better understand material properties. In the following section, instrumentation and typical experimental schematics for the optical spectroscopy techniques that were discussed in this section will be introduced.

2.2 Instrumentation and experimental schemes for optical spectroscopy

In a typical setup, optical spectra are recorded with a spectrograph and pixelated detector such as a CCD. This arrangement can be optimized depending on the application, for example by the use of bandpass filters to isolate a specific wavelength range, and the use of photomultiplier tubes (PMT)s to measure photons with high sensitivity. The majority of work in this dissertation employs a spectrograph-pixelated camera configuration for spectroscopy measurements and is therefore described in greater detail in this section. A spectrograph is a device that consists of a dispersive element, either a grating or a prism, and focusing optics that images the entrance slit onto a focal plane; most modern spectrographs use reflective gratings. The dispersive element spatially separates out the incident light into constituent wavelengths. The degree to which wavelengths are spatially resolved depends on the density of ridges or *lines* in the diffraction grating. Another property of the grating is the angle at which the lines are cut with respect to the surface normal. This angle determines the wavelength at which diffraction of a specific order of reflected light is optimized and is termed the "blaze angle". Grating function can be described in a similar form as

the well-known double-slit experiment, which demonstrated that the electrons exhibit particle-wave duality [197]. In this work, Young sent a collimated beam of electrons through a screen with two slits, and found that an interference pattern appeared on the screen. The relationship between the slit separation d with the wavelength λ of the light or particle is

$$d \sin \theta = m\lambda, \tag{2.12}$$

where θ is the angle between the diffracted wave and the normal of the plane of the slit, while m is the integer order (± 0, ± 1, ± 2,...). For a monochromatic source, this interference pattern would be observed as fringes with periods of bright spots, where the greatest intensity is at $m = 0$, separated by dark spots that form as a result of destructive interference. From Eq. (2.12), it can be seen that there is a wavelength dependence, and therefore if a polychromatic light source is used, the different wavelengths are spatially separated. The separation of the fringes w at a distance z is related to the slit separation distance d by $w = z\lambda/d$. Therefore, a greater density of slits results in greater separation between the fringes. These slits function the same as the lines on a diffraction grating, and thus higher groove density gratings provide better spectral resolution. Although $m = 0$ generally results in the highest light intensity, the wavelength dependence is lost; therefore, most spectrographs are operated at $m = \pm 1$. An example of grating diffraction lines at a given blaze angle is shown in Fig. 2.7(a). When a grating with a blaze angle is considered, Eq. (2.12) becomes $d \sin(\theta_i - \theta_m) = m\lambda$, where θ_i is the incident angle and θ_m is the reflected angle.

Spectrographs also use an entrance slit, which can further influence the instrumental resolution and the light throughput efficiency. A large slit allows more light to be collected, but results in poorer spatial resolution as the focus formed by the spectrograph is an image of the entrance slit. Generally, a balance between the entrance slit size and spectral resolution is decided based on the goal of the experiment. One

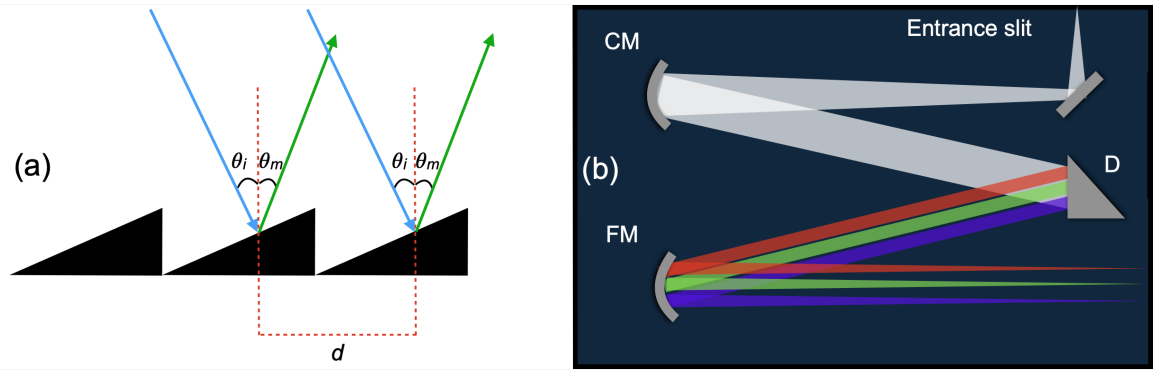

Figure 2.7: (a) An example of a grating and the incident and reflected light. (b) Schematic of a Czerny-Turner spectrograph. CM: collimating mirror; FM: focusing mirror; D: diffraction grating.

example of a common spectrograph is a Czerny-Turner style, which consists of an entrance slit, a collimating mirror, diffraction grating, and focusing mirror. A simplified schematic is shown in Fig. 2.7(b). There are other types of spectrographs optimized to achieve greater throughput efficiency, higher resolution, or broad spectral range within a small spatial window, but they share the same operating principle. A pixelated detector or camera is placed at the focal plane, and the spatially and spectrally spread light can be measured and calibrated from the pixel(s) illuminated. With a light source that has well-defined lines, for example a Hg-Ar lamp, peaks will appear in the spectrum. The most common cameras are charge-coupled devices (CCD) or complementary metal-oxide-semiconductor (CMOS), which use semiconductor chip that converts the light into an electrical signal such that the signal is proportional to light intensity. In some cases, amplification or gating of weak signal is necessary. In this case, intensifying- (I-) or electron multiplying- (EM-)CCDs are used, which can apply time-dependent gain to the electronic signal.

Figure 2.8 shows example schematics for (a) LIBS and optical emission spectroscopy, (b) LIF, and (c) absorption spectroscopy. For the LIBS schematic, a pulsed laser is used to induce breakdown on a solid surface and produce a luminous plasma. The light emitted from the plasma is collected with a lens and focused directed to the

Czerny-Turner style spectrograph. In place of a lens, a telescope or other focusing optic can be used depending on the experimental configuration. Similarly in LIF, a laser is used to excite fluorescence in an aqueous sample, which is collected with a lens or focusing optic. One difference is the use of an optical fiber that can be used to guide the collected signal to the entrance slit of the spectrograph. This allows for more flexible arrangement of the instrumentation. In absorption measurements, it is common to employ either a broadband or tunable light source and measure the wavelength-dependent transmission. The change in intensity is dependent on the concentration or population density of the absorbing species and the path length, as described by Eq. (2.11).

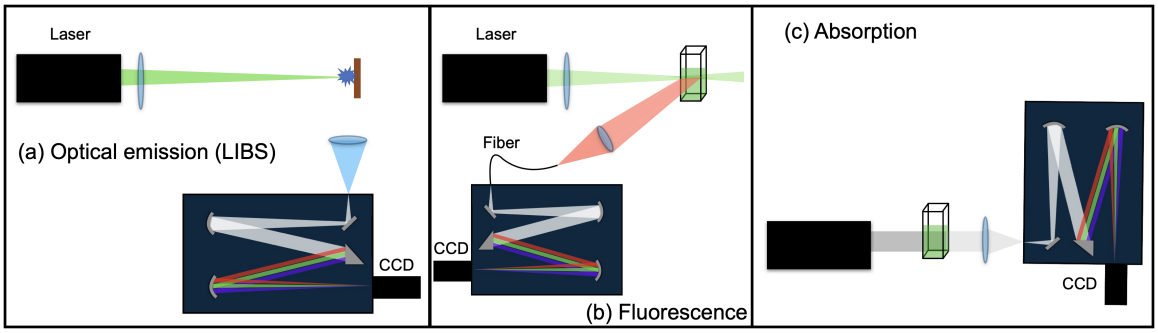

Figure 2.8: Simplified experimental schemes for (a) LIBS, (b) LIF spectroscopy, and (c) absorption spectroscopy. These schemes contain the basic instrumentation requirements for making these common optical spectroscopy measurements.

2.3 Nonlinear propagation of ultrafast lasers and filamentation

2.3.1 Filament formation conditions

One limitation of laser-based analytical techniques is the distance at which the laser energy can be delivered to a target. In particular, for LA, diffraction becomes the limiting factor as it prevents focusing to a small spot size, such that high enough intensity to cause breakdown cannot be reached. As the beam propagates, the beam

waist expands due to the beam divergence and diffraction. The distance over which the beam expands to 2× its initial beam waist is referred to as the Rayleigh range (z_R), defined as

$$z_R = \frac{\pi\omega_0}{\lambda}, \tag{2.13}$$

where ω_0 is the initial beam waist or radius and λ is the wavelength.

Work done by Donna Strickland and Gérard Mourou [176] paved the way for high peak power laser technology to be advanced. They developed a method to generate ultrashort laser pulses with high peak powers through a process called chirped-pulse amplification (CPA). This process consists of expanding a low power, ultrashort pulse by its spectral components in time (or making a "chirped" pulse) using a diffractive optical arrangement, passing that pulse through amplification stage(s) to produce a high-energy, long-duration pulse, and finally compressing it using an inverse diffractive optical arrangement. The first diffractive arrangement used to expand the pulse in time is referred to as the "stretcher", while the second arrangement that compresses the pulse is called the "compressor". Prior to CPA, the laser peak power was severely limited by optical damage in the amplification stage. By chirping the pulse prior to amplification, this damage occurs at a much greater fluence. With this new technology came a new era of optical physics, and this contribution resulted in the 2018 Nobel Prize in Physics awarded to Donna Strickland and Gérard Mourou.

One phenomenon of nonlinear propagation of high-peak power pulses has allowed for focusing to extend beyond the diffraction limit, such that a beam can maintain a small beam waist at long distances. This phenomenon is called *filamentation* [22] and occurs as the result of a third-order nonlinear effect referred to as the Kerr effect:

$$n = n_0 + n_2 I, \tag{2.14}$$

where n is the refractive index, n_0 is the linear refractive index, n_2 is the nonlinear

refractive index, and I is the electric field intensity [37]. This n_2 becomes amplified with increased laser intensity as a result of an induced nonlinear polarizability (or induced dipole moment in molecules) in the propagation medium. For high-intensity lasers propagating in air, the change in refractive index mimics the beam intensity profile, which is normally peaked near its center. Therefore, the refractive index change forms a virtual lens in the medium and causes the beam to self-focus even without the use of an external lens. Once the beam self-focuses, it reaches a high enough intensity to ionize the propagation medium. This results in the formation of a plasma column referred to as a *filament*. There is a dynamic interplay between the Kerr effect, diffraction, and defocusing as a result of the plasma formation that allows the filament to form and persist over large distances. Filaments have been shown to extend as far as kilometers away from the laser source [154]. Mathematical descriptions and derivations of the electric-field dependent polarizability of materials and nonlinear optical effects can be found in Refs. [102], [165], and [37]. The balance among these three effects can be described as

$$n_2 I = \frac{4\pi N_e}{2m_e\omega_0} + \frac{1.22\lambda_0^2}{8\pi n_0\omega_0}, \tag{2.15}$$

where $n_2 I$ is the nonlinear refractive index and intensity, the first term on the right-hand side is the plasma defocusing term, and the second term on the right-hand side describes the effect of diffraction. Therefore, as long as $n_2 I$ outweighs the plasma defocusing and diffraction, self-focusing will occur. Figure 2.9 shows a schematic which demonstrates this cyclic balance. Interestingly, because of the relationship shown in Eq. (2.15), it is found that the filament intensity is clamped and cannot be greater than approximately 5×10^{13} W cm^{-2}, even with increased laser energy [12].

Many physical processes of filaments were unknown, and a large focus of has been on understanding its complex physics, namely the dependence of the laser wavelength

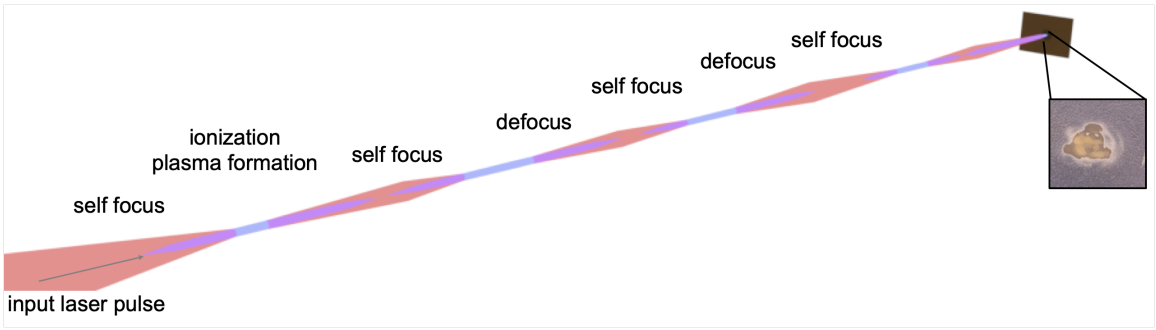

Figure 2.9: Schematic representation of the dynamic balance between self-focusing, plasma defocusing, and diffraction resulting in extended propagation of filaments.

on filament formation. It was found that the wavelength influences the critical peak power (P_{cr}) needed for Kerr self-focusing:

$$P_{cr} = \frac{C\lambda^2}{8\pi n_2 n_0}, \tag{2.16}$$

where λ is the laser wavelength, n_2 is the nonlinear refractive index, n_0 is the linear refractive index of the medium, and C is a constant dependent on the beam profile ($C = 3.77$ for a Gaussian) [141]. P_{cr} is proportional to λ^2, and with decreasing λ, the individual photons have a higher energy and therefore can increase ionization probability of the medium. When comparing filamentation for various wavelengths, it has been found that the shorter wavelengths result in longer filaments [26, 64].

Another phenomenon associated with filamentation is the spectral broadening, or supercontinuum, as the beam propagates and forms the filament. This spectral broadening is a result of self-phase modulation (SPM), where the laser accumulates self-generated phase as a function of time. Generally, the spectrum is red- and blue-shifted from the index change caused by both the beam and the plasma [37, 154]. The self-generated accumulated phase is $\frac{\omega_0 \Delta n(t)}{c} z$, where ω_0 is the angular frequency, $\Delta n(t)$ is the change in refractive index as a function of time t, c is the speed of light, and z is the distance over which the beam has traveled. The plasma formation generally results in a blue-shifted spectrum. A red-shift is observed from the front portion of the

pulse interacting with primarily neutral gas, but the back portion of the pulse interacts with excited gas. Spectral broadening is visibly observed upon filament collapse, where diffraction and defocusing counteract the Kerr effect, and a radial distribution of spectrally broadened light is observed [130]. This is referred to as conical emission. A more detailed description of the radial distribution of the broadened spectrum can be found in Ref. [37]. Conical emission has been demonstrated to be useful for light detection and ranging (LIDAR) applications, as the filament allows for remote excitation with a broadband, ultrashort pulse [27, 200]. This capacity for remote optical detection initiated a new field of applications. For this reason, the investigation of filament properties is essential to understanding their application space.

2.3.2 Applications and challenges of filaments in remote optical detection

While LIDAR is a promising application of filaments, it has also been shown that filaments can enable remote LIBS, also known as FIBS. Previously, clamped intensity was introduced, which affects the ability of filaments to induce breakdown on a solid target. It has been found that filament ablation produces even cooler plasmas than fs-LA [84]. However, the driving laser wavelength for filament formation is found to also significantly influence in the ablation efficiency. Burger *et al.* investigated the influence of peak power on FIBS for 0.4-, 0.8-, and 2.0-µm wavelengths [26]. They found that both 0.4-µm and 0.8-µm laser sources produced LPPs with a greater optical emission intensity than the 2.0-µm filament upon ablation of a metal copper target. Therefore, laser wavelength still plays a important role in the ionization and breakdown affects of materials in FIBS.

Filaments are known to be surrounded by an energy reservoir that feeds the filament formation over extended distances as energy loss occurs through atmospheric absorption, ionization of air, and transmission through the plasma. In many studies, external focusing of the beam is used to force filamentation over a specified length.

The effect of self-focusing is still observed, where the filament visibly forms prior to geometric focus of the focusing optic. However, because of the energy reservoir, differences in optical emission intensity from LPPs formed from filament ablation with both external focusing and free-propagation have been observed [25, 62, 84]. Previous work has found that external focusing used to initiate filamentation results in higher temperature and greater optical emission intensity from filament-produced plasmas [84]. This is because the energy reservoir is also being focused and can contribute to ablation; however, in free-propagating filamentation, the energy reservoir feeds the filaments over a given distance and does not reach a high enough intensity to cause breakdown. Even with free-propagating filaments, the energy reservoir plays an important role in sustaining the extended confinement of laser energy. Previous work has shown that if the energy reservoir is blocked, the filament collapses almost immediately [37, 124, 125]. Therefore, the energy reservoir is essential for extended propagation of filaments.

With increasing peak power above P_{cr}, another phenomenon known as multiple filamentation can occur. Multiple filament formation has been found to occur once the peak power reaches $\sim 10 \times P_{cr}$, and is seeded by modulation instabilities in the laser beam, laser wavefront aberrations, and air turbulence [13, 201]. For these reasons, the multi-filament structure is rather sporadic in nature. An example of a multi-filament pattern is shown in Fig. 2.9, where the magnified inset is a filament profile recorded on burn paper. It has been shown that the filament structure can be controlled using a spatial light modulator (SLM) [20, 90], adaptive optics such as deformable mirrors [53, 106, 112], and axicon lenses [166]. Multi-filaments can be suppressed to form a single *superfilament* through wavefront corrections and smoothing of the beam profile [78, 149]. Despite efforts to control filament patterns, there is a competition among these multiple filaments. Previous work found that with increasing peak power, the optical emission intensity from filament ablation of a solid copper target increases despite

the formation of multiple filaments [169]. While this finding is important to remote FIBS applications, it is still beneficial to investigate the formation of a multi-filament structure optimal for FIBS or for other applications, such optical waveguides [31, 103, 116, 119, 158, 168].

One application of interest has been the use of remote FIBS for nuclear non-proliferation purposes, for example the monitoring of uranium enrichment activities. Centrifuge enrichment facility emissions that were mentioned in Chapter 1 are an example of a scenario where remote optical spectroscopy may be beneficial over traditional ionizing radiation measurements that are commonly used for nuclear material monitoring. The ability to make isotopic measurements via FIBS and to resolve molecular structure with F-IF provide two potential technologies that may be used for this purpose. The following section introduces the present work and challenges associated with optical spectroscopy of uranium and uranium plasmas produced from laser ablation.

2.4 Spectroscopy of uranium-containing laser produced plasmas

One objective of this dissertation is to investigate how the optical spectroscopy of uranium and uranium-containing molecules may provide identifying signatures for nuclear security. Natural uranium consists of primarily U-238 (99.3%) and U-235 (0.7%). Enrichment of uranium can increase the fraction of U-235 for use in nuclear reactors (usually several % U-235), but can also be used to produce highly enriched uranium ($\gtrsim$90%) for nuclear weapons. Therefore, being able to measure the isotopic composition of uranium is essential for distinguishing peaceful from potential military applications. Accompanied by high-resolution spectrometers, optical emission spectroscopy of LPPs can provide isotopic information about the target material. Isotopic

shifts in optical emission spectra arise from differences in hyperfine splitting, which occurs from the interaction of the nucleus with the surrounding electron cloud. The mass of the nucleus can influence the binding of the electrons to the nucleus, and therefore the hyperfine splitting and spacing between electronic levels [9]. For atomic and ionic uranium lines, the isotope shifts when comparing U-238 to U-235 are on average ∼7–8 pm [148]. One major challenge with isotopic measurements of uranium is the complexity of the spectrum. An example is shown in Fig. 2.10(a), where a uranium LPP is formed in a low-pressure environment with minimal contaminants. A combination of fine, closely-spaced atomic and ionic lines can make it difficult to distinguish isotopic shifts. In remote applications, the weak signal can make it more difficult to distinguish dense lines from noise.

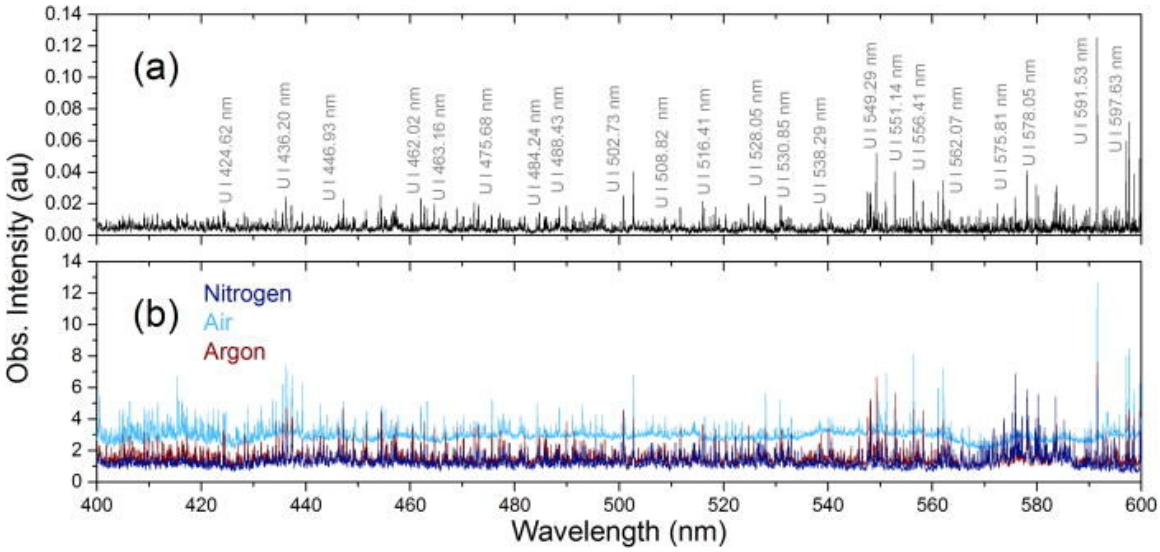

Figure 2.10: (a) Optical emission spectrum a uranium LPP in low (5 mTorr) pressure environment and (b) in 100 Torr air, nitrogen and argon environments [171].

Another added complication arises when the uranium plasma is exposed to contaminants such as air, as shown in Fig. 2.10(b). It can be seen that when in an argon and nitrogen environment, the baseline is relatively flat and near-zero. However, when exposed to air, the baseline is elevated along with the atomic and ionic lines. This elevation is due to the formation of uranium oxide molecules as the LPP expands

and cools. Without properly understanding the background, the observed signal-to-background ratio (SBR) can be low, leading to a poor detection prospects. Several works have presented the identification of many uranium-oxide spectral features in this elevated baseline [83, 86, 170, 171], such as that of UO, UO_2, and potential other U_xO_y. One of such signatures promising for uranium isotopic analysis is UO, which appears at 593.55 nm. This emission feature was found to have a much larger isotope shift than atomic and ionic lines [86], on the order of 50 pm, making uranium isotopic measurements via LIBS and FIBS more feasible.

In practical scenarios of *in-situ* monitoring, only the ablation of uranium in air is practical. Therefore, understanding the uranium LPP optical emission spectrum in air is important to identify promising signatures for rapid detection of uranium. In many cases, ns-lasers are used to investigate the conditions under which molecular signatures form in LPPs [108, 171, 192]. This provides fundamental thermodynamic information on the formation of uranium-oxide species. However, as previously discussed in Sec. 2.3 and 2.1, fs- and filament-ablation of metals results in cooler temperatures which favor the formation of molecules in the plasma. Therefore, the need for understanding filament properties at high peak powers required for remote excitation, and the influence of filament formation conditions on optical spectra observed after filament ablation is the motivation for Chapters 4 and 5.

CHAPTER 3

Optical Properties of Plants

Plant health monitoring has been an area of interest in various fields, such as agriculture and crop growth [162], algae biofuel development [114], pollution monitoring [8], biosensor development [6, 107, 186], and assessment of nuclear remediation [51, 110]. The majority of studies have focused on understanding how various plant species respond to natural stresses, like drought, or heavy metal stress of common industrial pollutants such as lead, cadmium, and arsenic. Several methods are commonly used to asses plant health, such as protein sequencing and genomics [10, 101, 131, 205], pulse amplitude modulated fluorometry (PAM-F) [138], reflectance spectroscopy and hyperspectral imaging [182], and solar-induced fluorescence (SIF) of chlorophyll [137]. Each of these techniques have unique benefits, such as the information that they provide on the plant or photosynthetic function and in-field measurement capability. For example, protein and mRNA sequencing are able to provide an in-depth analysis of the plants' function at a cellular level, photosynthetic function, communication processes, and stress response [21, 188]. The drawbacks to this method are that it requires sample preparation, and data analysis can be intensive and time consuming, making it unsuitable for real-time, in-field monitoring.

Methods which use plants' optical properties, on the other hand, are much more promising for *in-situ* monitoring. PAM-F is commonly used for rapid assessment of

plant photosynthetic function. This method uses Kautsky kinetics [138] of ChlF to obtain information on the fluorescence quantum yield, inhibition of the photosystems, total photosynthetic efficiency, and NPQ of the ChlF by energy transfer between Chl and carotenoids (Car). The main drawback of this technique is that it is limited in the distance at which measurements are attainable. Reflectance and SIF are the most adaptable to remote sensing. Reflectance spectroscopy of a broadband light source or solar radiation can be used to gain insight into the water content, pigment content, and biomass of the plant, all of which are useful in auditing the environment. SIF is commonly implemented for climate monitoring by associating the magnitude of the fluorescence signal with CO_2 or H_2O content in the air [137]. The main drawback to both of these techniques is that they are inhibited by large solar background, which can lead to long measurement times, especially when the density of plant material is low.

Despite these drawbacks, each of these techniques have impacted the progress of basic and applied science in plant function and environmental monitoring. However, it is still necessary to identify a method that could be used for in-field monitoring and overcome the limitations of large solar background and weak signal in the scenario of limited biological material. One method that may be useful in plant health monitoring is that of LIF of Chl. There have been several works using ns-laser excitation to detect overall fluorescence intensity at different times of day, and found that this corresponded well with the results of PAM-F in terms of fluorescence quantum yield [157]. Short-pulse lasers, which have been less commonly reported in the literature for plant health monitoring, offer two primary benefits to ns-lasers: (1) the ability to undergo filamentation at high peak powers, thus enabling remote excitation, and (2) the ability to resolve rapid molecular dynamics. There have been a few reports that explored the feasibility of fs-LIF to excite *in-vivo* ChlF in moss [167, 195, 196]; however further work is needed to better understand the signatures measured via

fs-LIF. The use of filaments to excite plant material non-destructively had not been reported to date, and is explored in this dissertation.

3.1 Photosynthesis and the relation to plant optical properties

3.1.1 Photosynthetic chain

The process and function of the photosynthetic chain are fundamental to the manifestation of plants' optical properties. There are several references that provide in-depth reviews of the Calvin cycle and photosynthesis [28, 153]. Here, only those functions known to be directly relevant to measurable optical signatures are discussed. All biological species that undergo photosynthesis contain chloroplasts, which have thylakoid membranes consisting of two main photosystems (PS), PSI and PSII, as shown in Fig. 3.1. Chloroplasts consists of chlorophyll *a*, chlorophyll *b*, carotenoids, and xanthophylls. Chl *a* and Chl *b* have a similar molecular structure, but they have different roles in plant function. Chl *a* is the main pigment involved in light capture for photosynthesis, whereas Chl *b* and carotenoids are accessory pigments that can assist in either light capture and transfer to Chl *a* or dissipate of excess light energy captured by Chl *a*. Under most healthy conditions, approximately 80% of the light absorbed by green plants is used for photosynthesis [198]. The thylakoid membrane is the location of the photosynthetic chain, where PSII is the first step and is involved in converting water to H^+, O_2, and free electrons. This site referred to as the oxygen-evolving complex. The free electrons produced in PSII are transferred to the first open electron acceptor, quinone-A (QA). While QA occupies this electron, the first reaction center is considered to be "closed". Once QA is able to pass its electron to the second electron-accepting site, QB, the reaction center becomes open again. The steps following this electron transfer in the photosynthetic chain influence the

availability of QA and QB. If light is collected by Chl *a* in PSII while the reaction center is closed, it must dissipate of this energy either through NPQ or fluorescence. These processes are constantly in competition with each other, where fluorescence occurs approximately 3% of the time that Chl *a* is excited [28].

PSI also collects light, but the main function is to convert NADP to NADPH. NADPH is essential in signalling the beginning of the Calvin cycle, the second stage of photosynthesis. The Calvin cycle is the step in which NAPDH fuels the conversion of CO_2 into sugars which provide energy for plant growth and development. PSI has iron-containing molecules that assist in the process; therefore, iron deficiencies or other changes to these molecules may influence the activity of PSI. Since PSII is involved in water processing, it is often most sensitive to natural stresses, which primarily involve water and light stress. The function of PSII is often the main photosystem discussed when assessing stress response due to its important role as the first step in the photosynthetic chain.

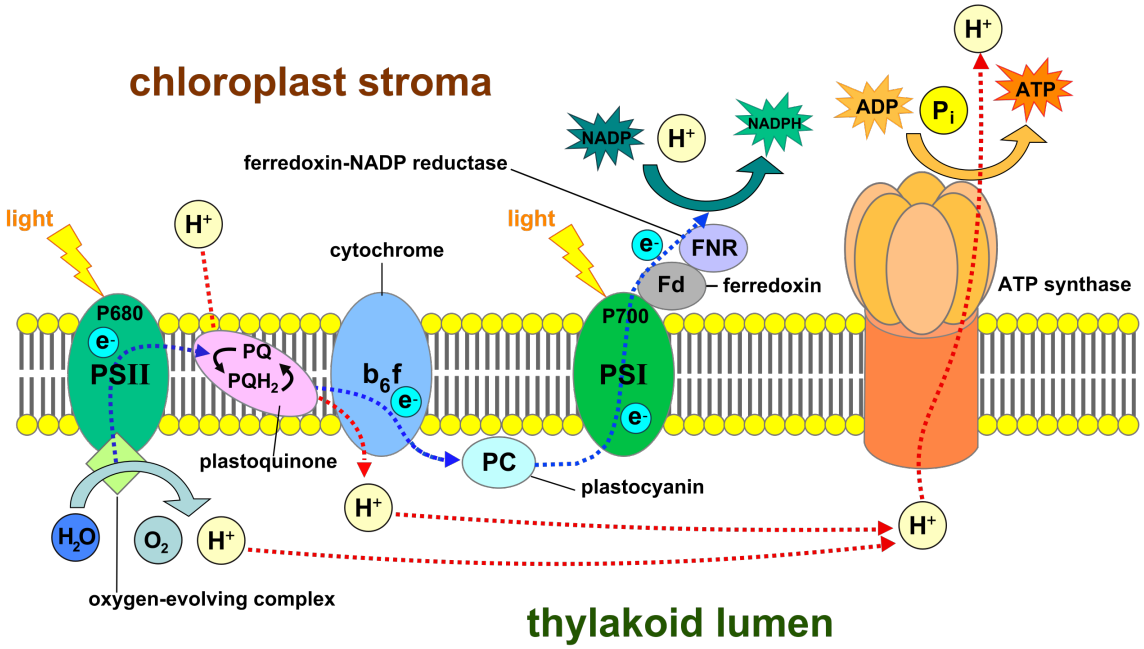

Figure 3.1: Photosynthetic chain in the thylakoid membrane of plant cells, original artwork created by [172].

Disruptions and changes in the photosynthetic activity generally occur as a result of stress, either from natural occurrences like excess light exposure and drought or from external factors such as pollution. Radical or reactive oxygen species (ROS) often form as a result of stress, first from oxidation of O_2 either by photo-oxidation or oxidation by excited Chl *a* [164]. The most common ROS are $O_2^{\bullet -}$, $^{\bullet}OH$, H_2O_2, $^1O_2$. ROS can form along the photosynthetic chain; approximately 1% of O_2 in plants is converted to ROS in a healthy plant. Oxidative stress occurs when the ROS level is above the natural defense mechanism. Carotenoids are non-enzymatic antioxidants that can protect against ROS and oxidative stress. Singlet oxygen, $^1O_2$, can form in the chloroplast via triplet-excited chlorophyll (^{3}Chl) in PSII. ^{3}Chl forms when there is excess energy in the reaction center through light-induced charge recombination, allowing the following reaction to occur: $^3\text{Chl}+^3O_2 \rightarrow \text{Chl}+^1O_2$. β-carotene and other antioxidants can quench $^1O_2$. In many studies that explore stress, an increased level of carotenoids when there is excess $^1O_2$ is observed, in particular under stress conditions which lead to elevated likelihood of ^{3}Chl. $O_2^{\bullet -}$ can lead to the formation of secondary ROS, like H_2O_2. While these latter two ROS are moderately nonreactive, but can lead to the formation of $^{\bullet}OH$ which is highly reactive and can cause damage since plants have very limited protection against it.

Metal stress has shown to significantly affect overall photosynthetic efficiency by deteriorating the metabolism and electron transport chain. Redox-active metals, such as iron, copper, and chromium, undergo redox cycling producing ROS, whereas redox-inactive metals, such as lead, cadmium, mercury, and others deplete cell's major antioxidants, particularly thiol (-SH) containing antioxidants and enzymes (not carotenoids). Plants have three potential pathways to fight ROS formed under stress: (1) diminish electron transport chain; (2) enhanced use of xanthophyll cycle-dependent thermal dissipation to minimize damage to LHCII antennae; and (3) produce enzymatic and non-enzymatic antioxidants to scavenge ROS [164]. The

series of conjugated double bonds in Car allow for easy capture of excess energy that can be redistributed and emitted as heat, which is why in many cases an increase in Car or xanthyophyll content is observed when a plant is under stress. Changes in pigment content is one way to assess early stages of plant stress. The following section discusses the most common ways to quantify plant pigments.

3.1.2 Photosynthetic pigment quantification

Plant pigments, such as chlorophylls, carotenoids, and xanthophylls, reside in the chloroplast. These pigments are "prenyl pigments", meaning that they have hydrophobic functional groups attached to proteins. Chlorophylls and carotenoids are fat-soluble, and can be extracted from water-containing plant tissue with polar organic solvents. Methanol, ethanol, diethyl ether, and acetone are the most common extraction solvents. Water content of the extraction solvents must be less than 10%, otherwise the extraction efficiency is poor due to the hydrophobicity. The steady-state UV-VIS-NIR absorption spectrum of these extracted pigments can be used to quantify the abundance of certain pigments. Spectrophotometers are used to perform these measurements, where a dual-beam light source is selectively scanned across a wavelength range, and the difference in light intensity from the "blank", or sample containing only the extraction solution, and the sample containing the pigments is used to calculate absorbance. Absorbance is defined as

$$A_\lambda = -\log(I_\lambda / I_{0,\lambda}) \text{ and } A_\lambda = \epsilon_\lambda bc, \tag{3.1}$$

where A_λ is the absorbance at a given wavelength λ, I is the light intensity of the pigment containing sample, I_0 is the light intensity for the blank sample, ϵ is the molar extinction coefficient of a specific molecule in a given solution, b is the path length, and c is the concentration. It can be seen from Eq. (3.1) that once the

molar extinction coefficient is measured for a specific molecule and b is known, the absorbance is proportional to the concentration of the given molecule. Example absorption spectra of Chl a and Chl b in ethanol and lutein, a type of xanythophyll, in diethyl ether are shown in Fig. 3.2(a). These pigments have distinct, but overlapping spectral features which can make it challenging to extract information about each separately. It is particularly difficult to identify specific carotenoids as they have very similar absorption spectra that overlap significantly, which is why in almost all cases it is common to refer to the total carotenoid concentration. Porra *et al.* [151] and Lichtenthaler [120] provide derivations of equations which can be used to calculate the concentration of Chl a, Chl b, and total carotenoids in the extracted solution based on each pigments specific wavelength-dependent molar extinction coefficients. The polarity of the extraction solvent can cause shifts and intensity changes in the absorption spectrum; therefore, the exact equations differ slightly depending on the solvent used. The total concentration and ratios of certain pigments can provide information about plant health. Figure 3.2 shows an example absorption spectrum of pigments extracted with 190 proof ethanol from leaves of *Pachira aquatica*, where the chlorophylls and carotenoids are mixed.

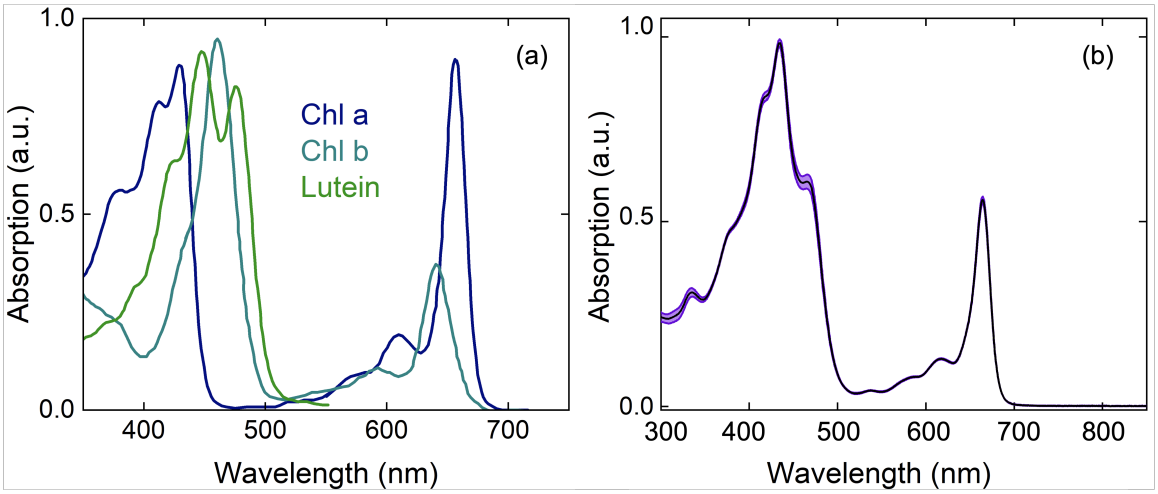

Figure 3.2: Example absorption by Chl a and Chl b in 95% ethanol and lutein in diethyl ether, digitized and adapted from Ref. [120] (a). Pigments extracted from *Pachira aquatica* leaves in 95% ethanol (b).

Table 3.1: Common equations used to extract information on pigment content from the broadband reflectance spectrum of higher plants. More relations can be found in Ref. [18].

Species	Relation
Chl *a*	R_{800}/R_{680}
Chl *b*	R_{800}/R_{635} or R_{800}/R_{650}
Car	R_{470} or R_{800}/R_{470}

The absorbance spectrum and reflectance spectrum are complementary to each other, and therefore pigment content can also be quantified through reflectance spectroscopy. An example reflectance spectrum of healthy green grass is shown in Fig. 3.3. Because pigments do not strongly absorb light above approximately 705 nm, the NIR wavelengths provide information about leaf tissue, cellular structure, and deeper into the mid-IR contains signatures of water content. The drastic increase in reflectance at 705 nm is referred to as the "red edge" in the literature, and may be used to infer about the chlorophyll content [182]. There are many different relationships that have been derived and tested for best quantifying Chl *a*, Chl *b*, and Car concentration from reflectance spectra. Some of the most common correlations are shown in Table 3.1; R is the magnitude of the reflectance at the specified wavelengths. In general, the [Car] using these relationships have lower R^2 when performing regression analysis on the relationship between reflectance and concentration measured using absorption spectroscopy from extracted pigments. In general, good agreement is found for [Chl *a*] and [Chl *b*] in green plants. More relationships from the reflectance spectra for quantification of pigment content can be found in Refs. [18] and [71].

The concentration of plant pigments provides complementary information to ChlF and allows for a better understanding of the relationship between plant function and fluorescence parameters. Signatures specific to various stresses that would allow discrimination of natural stresses such as drought from heavy metal stress, or even distinguish between different metal stresses, may exist and may be extracted from a comprehensive set of data that combines the pigment quantification with ChlF

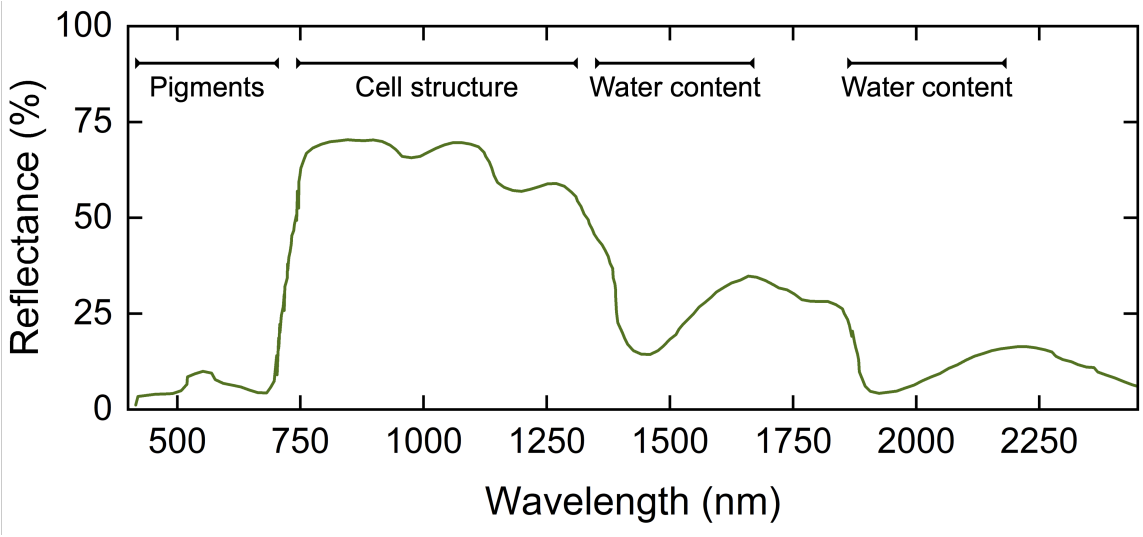

Figure 3.3: Example reflectance spectrum of green grass, adapted from Ref. [73].

parameters. The following section discusses the main ChlF techniques currently used in-field and how they are implemented to monitor plant health and stress response.

3.2 Chlorophyll fluorescence for plant health monitoring: background

Chl *a* is the main pigment involved in light capture for photosynthesis, and the kinetics of its fluorescence can provide information on the photosynthetic chain and function. Ref. [28] and Ref. [138] provide a detailed review over the photosynthetic chain and the roles of different Chl molecules. Here, several points relevant to ChlF are introduced. Chl *a* resides in two main sites along the photosynthetic chain in light harvesting complexes or photosystems, as reaction centers in PSI and PSII. The light collected by these light harvesting complexes can undergo three different processes in the reaction centers: drive photosynthesis, dissipate the energy as heat, or emit energy as fluorescence. Under normal conditions, fluorescence from Chl occurs approximately 3% of the time, while photosynthesis is the dominant process occurring approximately 80% of the time that light is collected, and NPQ occurs with the

remainder of the light collected [198]. There is a continuous competition among these three processes, making fluorescence informative on the photosynthetic efficiency of the plant. The chemical environment and function of the two photosystems are different, and this influences the ChlF spectrum. PSII predominantly fluoresces at approximately 675 nm and PSI fluoresces at approximately 720–740 nm. Therefore, the overall intensity and lifetime of these two fluorescence bands can be used to gain information on the function of the two photosystems. This is of particular interest in identifying how different stressors influence the photosynthetic chain. Both PAM-F and SIF are used in-field regularly to monitor the environment. However, the two provide different information and also vary in their limitations as in-field techniques.

3.2.1 Pulse-Amplitude Modulated Fluorometry

3.2.1.1 Technology of PAM-F

PAM-F is one of the most commonly used in-field detection methods for plant health monitoring due to the abundance of information it provides and because it can be performed with a handheld, easy to transport device. PAM-F consists of a clip mount that attaches to the leaf, fiber optics that deliver excitation light, and long-pass or band-pass filters to select a part of the spectrum, generally between 630 nm and 740 nm. An example schematic for a generic PAM-F system can be found in Fig. 3.4(a). In most cases, an LED is used as the excitation source, either blue (445 nm), white (445 nm and 545 nm maximum emission), or far-red (745 nm) with a pulse duration on the order of µs. The different wavelengths can allow for selective study of specific photosystems, where the far-red excitation LED is used to study PSI function. The LEDS have varying light intensity, from very low intensity (25 µmol photons m^{-2} s^{-1} or approximately 5.5 W m^{-2}) up to saturating intensity for the photosystems (10000 µmol photons m^{-2} s^{-1} or approximately 2200 W m^{-2}). The fluorescence is collected by another optical fiber which consists of a filter to block any

reflected light from the leaf surface, a collimator for optimizing the collection efficiency into the fiber, a pulse amplifier, and the signal readout as a function of delay with respect to the LED pulse. A real handheld system with leaf clip attachment is shown in Fig. 3.4(b). The compact size makes it an ideal system for in-field deployment.

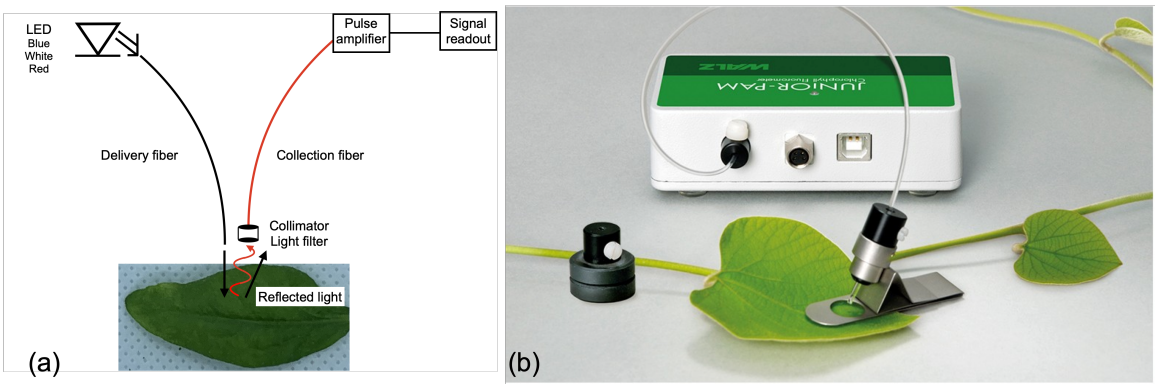

Figure 3.4: Example schematic for handheld PAM-F system (a). Field-deployable handheld PAM-F system by Walz [3] (b).

3.2.1.2 Fundamentals of PAM-F

The variable light intensity of the excitation LED in the PAM-F system allows for exploration of fluorescence kinetics and quenching mechanisms, referred to as Kautsky kinetics [138]. These can be studied in several scenarios by measuring the fluorescence intensity when a plant is dark adapted or exposed to actinic light (light peaking around 420 nm), and comparing that to the fluorescence intensity at different time delays after being exposed to a saturating pulse of light [23]. When adapted to darkness, all of the reaction centers in the photosynthetic chain are open, and therefore photosynthesis will occur upon exposure to light. However, when exposed to actinic light, the reaction centers are closed and the influence of NPQ on ChlF can be studied. An example PAM-F trace is shown in Fig. 3.5. There are two main types of quenching parameters that can be investigated with PAM-F: photochemical quenching (PQ) and NPQ. PQ occurs when the energy absorbed by Chl a is used for electron transfer and oxidation of water. The photosynthetic efficiency can be measured by comparing

the minimum fluorescence of the dark-adapted leaf to the maximum fluorescence once all the reaction centers are closed. The difference between the maximum fluorescence yield with the reaction centers open (F_m) and reaction centers closed upon exposure to saturating light source (F'_m) is related to the magnitude of NPQ. More specifics about the parameters measurable via PAM-F can be found in Ref. [23]. PAM-F is favorable due to its accuracy in providing an abundance of information on plant function in conjunction with being a relatively quick measurement. The main drawback of this method is that the hand-held device requires the user to physically be on-site, and it is limited in the distance at which the measurements can be made. These are impediments in scenarios where large-area monitoring is necessary, and particularly related to nonproliferation monitoring, where on-site access may not always be permitted.

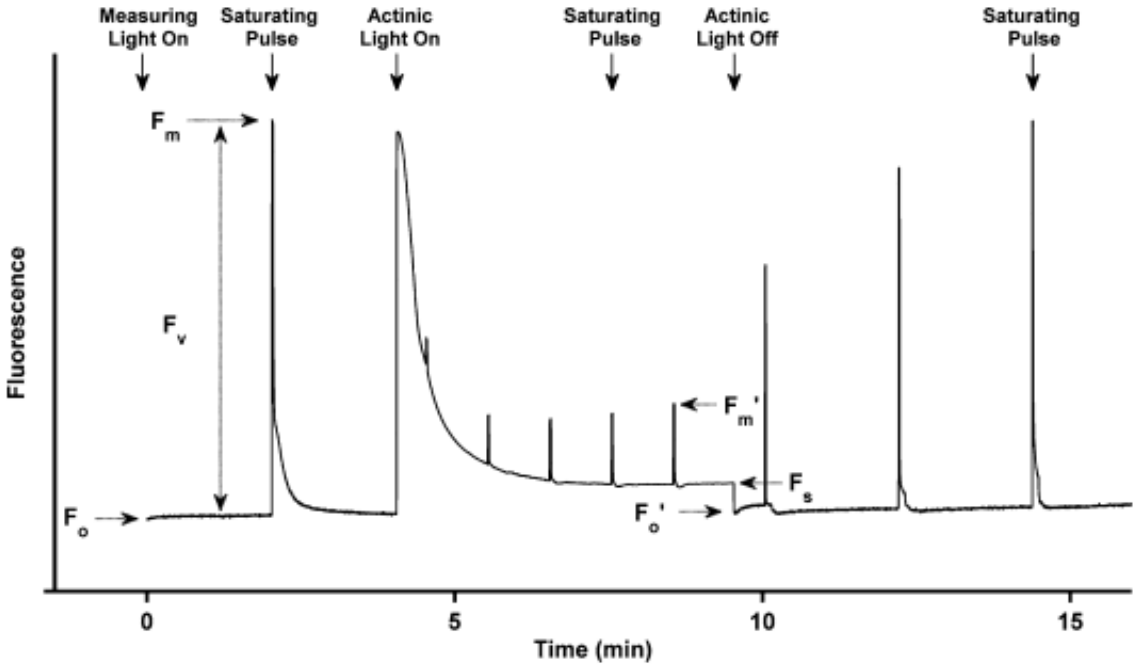

Figure 3.5: An example PAM-F trace recorded for wild-type *Arabidopsis thaliana* plant leaves from Ref. [23]

3.2.2 Solar-induced Fluorescence

3.2.2.1 Technological Schemes for SIF

Solar-induced fluorescence (SIF) is another widely-used in-field environmental monitoring method, which assesses large areas through monitoring naturally occurring fluorescence excited by solar radiation as opposed to induced fluorescence from an artificial light source. Because the fluorescence of Chl *a* is linked to photosynthesis, SIF can provide information on photosynthetic function. In most cases, SIF uses ground-based towers or satellites for broad-area surveillance to gain insight into the effects of climate change on plants' ability to process CO_2, which is important for understanding to what extent the plants can mitigate excessive release of carbon into the atmosphere [137]. Ground-based tower systems rely on a scanning collection telescope that is coupled to a spectrometer, usually measuring light from forest canopies [69, 77, 137, 204]. In modern systems, the angular resolution of these ground-based instruments is better than 0.1°, they can rotate 360° [77], and they can measure fluorescence while simultaneously monitoring the solar radiation. The FOV can allow for monitoring single trees in a canopy, with ∼60 s time resolution possible. It is common to have longer measurement times, ≥30 min, depending on the weather conditions. Satellite-based systems also consist of scanning telescopes, with generally poorer FOV, but can obtain information over a broader area and are capable of global monitoring. The angular resolution can be 0.5°, with a FOV covering approximately 100 km × 100 km area, and time resolution on the order of days depending on weather conditions [77]. There are several global satellite systems that regularly collect SIF data and other information related to atmospheric conditions that can be found on the National Oceanic and Atmospheric Administration website. The following section reviews how the data collected by satellite and ground-based telescope systems can be used to extract SIF information from the plants.

3.2.2.2 Fundamentals of SIF

The relatively small amount of light emitted by Chl *a* used for fluorescence measurements in comparison to the large contribution from solar background makes the direct measurements of ChlF challenging. One method used to extract the fluorescence bands from the large solar background is by measuring the depth of the Fraunhofer lines in the solar spectrum [137]. An example of absorption lines in the solar spectrum relevant to SIF are shown in Fig. 3.6. The broadband ChlF has peaks at approximately 680 nm and 720 nm. The absorption bands of primary interest in the region of the ChlF spectrum are the H-α line at 656 nm, O lines at 688 nm and 760 nm, and sometimes the water absorption bands around 720–740 nm [122]. When no vegetation is present, the absorbance is proportional to the concentration of hydrogen and oxygen in the atmosphere over the measurement path length, and the optical density of the Fraunhofer lines in many cases is known with 1–2% accuracy. If vegetation is present, the ChlF can be measured by the change in optical density at these well-known lines of interest. Ref. [122] provides an example of how this is implemented in practice.

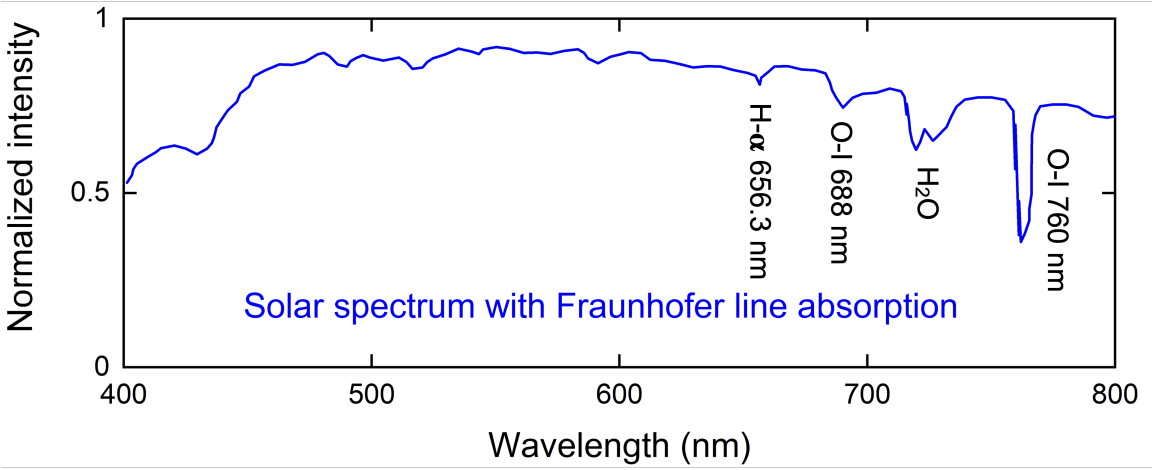

Figure 3.6: An example solar spectrum adapted from from Ref. [122] with atmospheric absorption, referred to as the Fraunhofer lines. The main lines commonly used for SIF analysis are labelled.

Collection systems used to monitor SIF vary from earth-based telescopes generally ranging from 1 m to 100 m in elevation to satellite-based SIF monitoring systems. Earth-based systems are able to monitor local vegetation, such as forests or farms, and obtain spatially resolved measurements by rotating in sub-1° steps [204]. Recent work has used spatially-resolved satellite-collected SIF signatures to assess the efficacy of China's reforestation efforts by quantifying Chl content simultaneously with water concentration measurements via microwave radiation [69]. While SIF data is primarily used in conjunction with other measurements, such as microwave radiation measurements for water content or reflectance spectroscopy for pigment and biomass information, SIF is also informative on the Chl content and how it changes depending the environment, weather, and time of year, which is of paramount importance to determining plants' role in and ability for mitigating effects of climate change.

3.2.3 Health Monitoring

The main focus of plant health monitoring relates to climate change, where the goal is to understand the fluctuation in plant function over time and the capability of plants to sufficiently consume and process CO_2. Also related to climate change, the goal has been to assess changes in ChlF yield with the worsening of drought [204]. Several previous works have demonstrated SIF of Chl *a* to successfully measure both the growth of vegetation [69] and loss of vegetation due to drought and intense heat [204]. Zhang *et al.* found that the magnitude of SIF correlated better with drought trends in Australia than other parameters measured by reflectance spectroscopy and greenness-related vegetation indices [204]. Gerlein-Safdi *et al.* reported that SIF could accurately monitor the effectiveness of reforestation efforts in China and found that microwave measurements of water content in vegetation generally correlated well with the SIF yield [69].

SIF has been shown to be beneficial in broad-area surveillance and is generally

accompanied by a complementary measurement. For rapid health monitoring, PAM-F is predominantly used, especially in cases of pollution and heavy metal monitoring. This is primarily due to the abundance of information it provides with higher time resolution than SIF. Similarities between SIF and PAM-F in relation to drought stress show that the overall fluorescence yield decreases due to increased NPQ and reduced photosynthetic activity [189]. The reason for this response is that drought significantly influences the function of PSII, which is the site of the water evolving complex and the first step in the photosynthetic chain. To avoid damage to PSII reaction centers, more Car and xanthophylls are involved in dissipation of the excess energy through heat.

Similarly, many previous works have reported reduced photosynthetic activity and increased NPQ upon plant exposure to heavy metals, such as copper, arsenic, cadmium, and others [101, 131, 205]. Mechanisms that lead to increased NPQ from heavy metal uptake in plants are disruptions in the photosynthetic electron transport chain resulting in formation of ROS, changes in the chloroplast shape, substitution of toxic metals in essential nutrients like potassium and calcium, and substitution of magnesium and zinc in Chl *a* by heavy metal ions [44]. For example, Maksymiec *et al.* found that within 15 hrs of exposure of *Arabidopsis thaliana* seedlings to 100 µM of Cu and Cd separately, the quantum yield of PSII photochemistry (photosynthetic efficiency) decreased, and continued to decrease up to 144 hrs of exposure. They also reported an increase in NPQ after 15 hrs compared to the control, and a significant increase after 48 hrs. Interestingly, the NPQ at 144 hrs after exposure had decreased from the 48 hrs of exposure, but in all cases was still higher than the control. The authors associate the increase in NPQ with an increase in $O_2^{\bullet-}$, a radical oxygen species. Similarly, Iriel *et al.* reported a decrease in quantum yield of PSII upon exposure of *Vallisneria gigantea*, *Azolla filiculodes*, and *Leman minor* to arsenic compared to a control after seven days of exposure [101]. Furthermore, with increased NPQ pri-

marily noted for *V. gigantea* and *A. filiculodes*, they observed decreased fluorescence intensity of the 680 nm peak compared to the 720 nm peak upon excitation with a continuous wave 460 nm light source. The decreased time-integrated fluorescence intensity is another sign of decreased PSII activity.

Often associated with increased NPQ is production of ROS [10, 131], increase in anthocyanin and Car content, and decrease in Chl content [10]. Baek *et al.* studied the effect on pigment content upon exposure of *A. thaliana* seedlings to several different metal stresses: copper, zinc, manganese, lead, and mercury [10]. In all cases, with increasing metal content exposure there was a decrease in Chl content and clear increase in anthocyanin content. Car content did not increase with the same magnitude as the anthocyanin, but it was observed to increase with high concentrations of all the metals tested except for manganese. While fluorescence parameters were not explored in this study, physical signs of reduced photosynthetic efficiency for plant growth are apparent in reduced root and shoot growth. In general, it is well-known that heavy metals induce the formation of ROS, reduce Chl content, increase production of Car especially at high metal concentrations, and reduce photosynthetic efficiency. Chl fluorescence measurements are useful in providing information on whether a plant is under stress, and how stress exposure influences the physiological function of the plant. While PAM-F and SIF are powerful techniques, there are several scenarios that require simultaneous remote and rapid measurement of Chl fluorescence. In the next section, laser-induced fluorescence of Chl is introduced along with how it may address some of the current limitations of PAM-F and SIF.

3.3 Laser-induced fluorescence of chlorophyll

Laser-induced fluorescence of Chl has been explored in the literature, though not as extensively as PAM-F or SIF. A typical schematic for LIF has been shown in Chapter 2, and is similar for applications in monitoring ChlF. Predominantly, the

literature reports experiments conducted with CW- or ns-LIF of Chl because a compact interrogation system can be constructed at relatively low cost. Nd:YAG lasers are often employed for ns-LIF experiments, emitting at 1064 nm, and can be frequency doubled or tripled to produce 532 nm and 355 nm wavelengths. Most systems are capable of achieving approximately 50-m standoff excitation [38]. The collection systems, similar to PAM-F, generally incorporate long-pass filters to reject reflected laser light and improve the signal-to-background ratio. With LIF, the ChlF can be measured directly as opposed to using changes in the optical density of Fraunhofer lines in SIF. Furthermore, the use of pulsed-laser excitation in combination with a gated photodetector allows for time-resolved measurements, which aids in rejection of solar background.

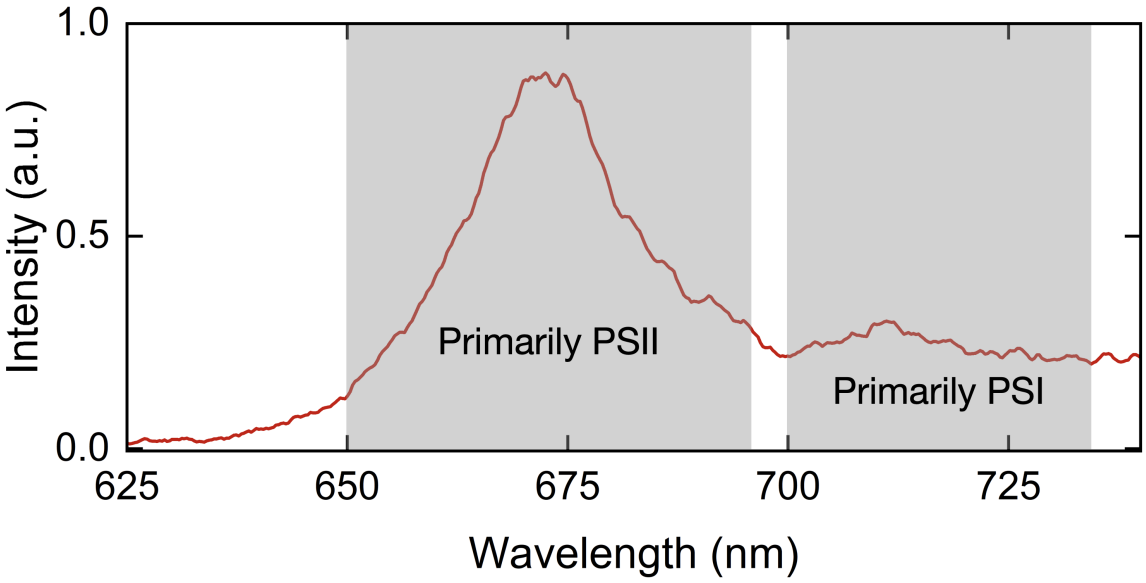

Figure 3.7: Example ChlF spectrum from extracted *Arabidopsis thaliana* thylakoid membranes suspended in 0.5 M HEPES KOH buffer. Fluorescence is excited with a 120-fs pulse duration frequency-doubled Ti:sapphire laser with a 1-µJ pulse energy. The light is collected with a fiber-coupled collimator and sent to a Czerny-Turner spectrograph and ICCD. Spectra are recorded at a delay of 0 ns and with a gate width of 10 ns.

More recently, the use of femtosecond lasers for LIF of chlorophyll have been investigated [167, 195, 196]. The time resolution of fs-laser spectroscopy is many orders

of magnitude better than that with ns-lasers, such that rapid molecular dynamics such as NPQ, which occurs on the sub-ns timescale [147], can be resolved from fs-LIF of chlorophyll. In ns-LIF, time-integrated fluorescence intensity and spectral shape are the main parameters that could be linked to plant stress [101, 177]. The high temporal resolution achievable with fs-LIF could potentially elicit greater specificity in distinguishing stressors. Also, the wavelengths available from standard fs-laser systems are more suitable for excitation of Chl than standard ns Nd-based lasers, including their harmonics. For example, Ti:sapphire lasers produce wavelengths that span ∼700–900 nm and can be frequency doubled such that the peak spectral intensity occurs around 400 nm. Chl *a* absorbs much more strongly at 400 nm than the Nd:YAG ns-laser produced 532 nm, as can be seen in Fig. 3.2. Improved absorption of the excitation light improves the selectivity in exciting primarily Chl *a* as opposed to considerable absorption by Car at 532 nm from the second harmonic of an Nd:YAG laser. The benefits of standoff and real-time analysis combined with background rejection offered by LIF could have a significant impact for rapid monitoring the early onset of stress in field applications.

3.3.1 Stress detection with laser-induced fluorescence of chlorophyll

An example ChlF spectrum generated from 400-nm fs-LIF of extracted thylakoid membranes from *A. thaliana* leaves is shown in Fig. 3.7. The two peaks are shaded and labelled according to the photosystems that mainly contribute to each. In general, the overall fluorescence yield and spectral shape can depend on the species, light exposure conditions, and environmental conditions. For example, in a previous study of LIF of Chl *a* it was demonstrated that the fluorescence yield is correlated to photosynthetic activity and cycles throughout the day while being correlated with other important parameters such as CO_2 assimilation and photosynthetically active radiation (PAR) intensity [157]. Figure 3.8 shows how the total ChlF intensity induced

by LIF correlates with the intensity of PAR in terms of a day-to-night cycle. In the first 24 hrs while the plants have sufficient water supply, ChlF intensity is roughly proportional to the PAR intensity. Interestingly, with decreased water availability over time, it is observed that increasing PAR results in increased ChlF intensity up until a maximum PAR level, where the ChlF yield then decreases. The change in relationship of ChlF with PAR light intensity upon reduced water uptake is a sign of increased NPQ due to drought stress. This example shows how LIF of chlorophyll can be related to photosynthetic activity.

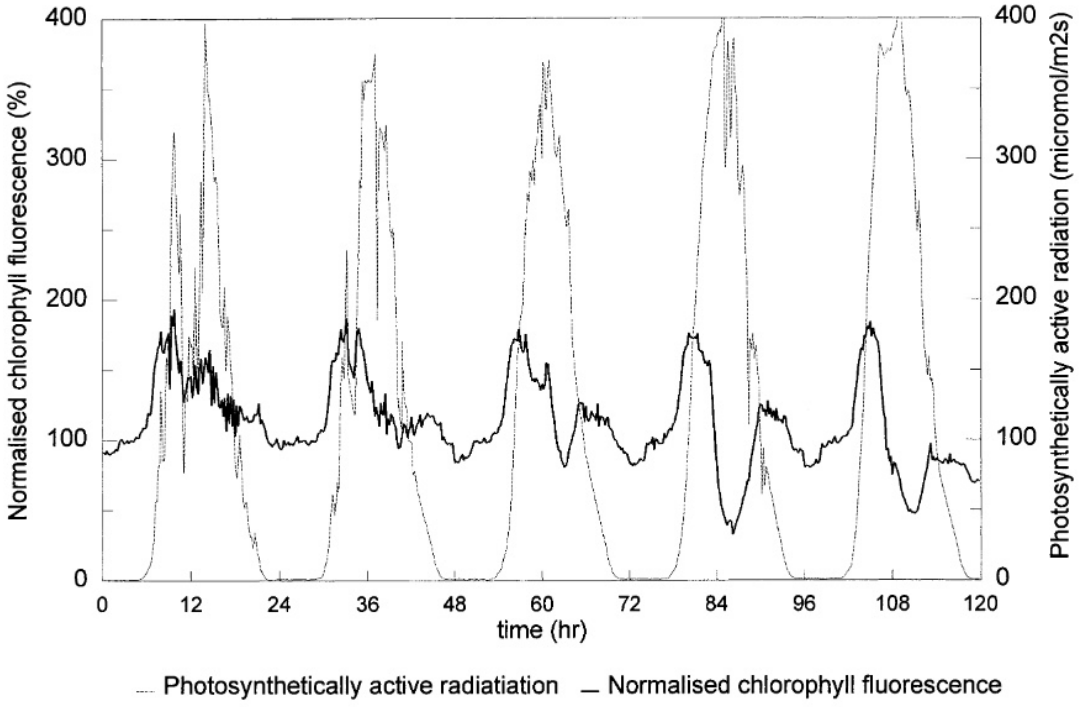

Figure 3.8: Fluctuation of LIF of chlorophyll of poplar plant leaves with photosynthetically active radiation intensity over several days [157]. The plants are watered in the first 24 hrs, but not during the remaining duration of the measurements.

Similar to PAM-F and SIF, a large focus has been on identifying signatures of drought and water stress in plants, largely due to the importance to agriculture and climate change. Several interesting relationships have been found between the drought stress and the ChlF spectrum, namely that the fluorescence intensity ratio

between the 680-nm peak and 720/730-nm peak changes, in some cases such that the 680-nm peak decreases with respect to the far-red fluorescence [177], while for other species the opposite effect occurs [67]. Yamakawa *et al.* and Shibata *et al.* further found, upon excitation with a fs-laser, that the rapid molecular dynamics leading to fluorescence quenching could be resolved and that the lifetime of the 680-nm peak decreases significantly for desiccation-resistant moss under drought stress compared to a control [167, 195, 196]. This decrease in fluorescence lifetime was attributed to increased NPQ in the PSII site in the photosynthetic chain, which is known to occur under drought stress from PAM-F measurements [189] and was observed with LIF by Rosema *et al.* [157].

Previous work has shown that air pollution that influence gas exchange processes, such as SO_2 and NO_2, results in an increase in the intensity of the 680 nm peak with respect to the 730-nm peak ($I_{680\ nm}/I_{730\ nm}$) for three different plant species upon excitation with a HeNe 632.8-nm laser [177]. They attribute the increase in fluorescence intensity ratios to reduced photosynthetic activity resulting in increased ChlF at PSII; previous work has shown that SO_2 significantly influences the electron transport chain. Another potential reason for increased ChlF $I_{680\ nm}$ is that the chlorophyll content has decreased, resulting in lower self-absorption by ChlF emitted at 680 nm as it escapes from deeper layers of the leaf. For heavy-metal stress, Gopal *et al.* found upon excitation with a 488-nm Ar laser that the total ChlF intensity of mung leaves decreased even at 0.1 mM exposure to nickel, and it decreased further with 1 mM nickel exposure. However, they observed that the intensity of the 680-nm peak decreased with a greater magnitude than the 730 nm peak [72]. Cabrita *et al.* explored the effect of nickel along with other heavy metals on the microalgae *Phaeodactylum tricornutum* and found that the peak intensity at 730 nm decreased more drastically than the 680-nm peak upon excitation with a 532 nm ns-pulsed laser [29]. While both observed an overall decrease in fluorescence intensity, the ratio

of the peak intensities were different in the two studies, which may be a result of the different exciting wavelengths used. The variations in fluorescence peak intensity differ depending on the excitation source, plant species, and pigment content.

While the observed variations in response and magnitude of metal accumulation among various plant species vary, it is generally found that most heavy metals are toxic to plants, and uptake or exposure results in a decrease in growth rate, cell death in particular for algae, and production of ROS [10, 29, 92]. Furthermore, it is common to also observe a decrease in overall pigment content and especially that of Chl *a* [10, 29]. Often times the ratio of [Chl *a*]:[Car] decreases due to an increase in Car with respect to the chlorophyll content. Increased [Car] with respect to the [Chl *a*] is often associated with increased NPQ, as the decreased [Chl *a*]:[Car] often occurs simultaneously with poorer photosynthetic efficiency [28]. Since the response to toxic heavy metals is known to occur, it is hypothesized that uranium exposure in plants could solicit a similar response. The following section provides a brief review of the literature that reports on uranium-induced effects on the plant health.

3.4 Uranium effects in plants

There has been recent interest in using living plants as biosensors for nuclear nonproliferation measurements, as well as the use of plants for phytoremediation of nuclear accidents [51, 110]. Uranium is relevant to both applications. Several studies have investigated the efficiency of uranium uptake in plants [19, 52, 89, 159]. Some studies have identified signatures that are measurable in-field [183–185], but no studies have reported the realization of remote monitoring using these signatures. One objective of this dissertation is to address this gap by examining the feasibility of the use of fs-laser- and filament-induced fluorescence for in-field nonproliferation monitoring.

Although uranium is not essential for plants, it has been found that most plant

species that have been investigated to date will uptake it to some degree in the roots and translocate it to the shoots. At sufficiently large concentrations, uranium is toxic and can result in oxidative stress. The concentration absorbed by plants is generally several orders of magnitude smaller than the concentration in the surrounding soil, where 10s–100s µM concentration in soil results in ∼µg/g of dry weight plant material [7]. One factor that influences the magnitude of uptake from soil or solution to the roots is the speciation of uranium, which is known to be pH dependent [52]. Uranium is most often found in the +VI oxidation state in the form of UO_2^{2+}, the uranyl cation, and is predominantly in this form in slightly acidic solutions, where the pH is ∼5 or lower, as shown in Fig. 3.9. Around a neutral or basic pH, other complexes like phosphates and carbonates form. When uranium is in the form of the uranyl cation, it is found to be more mobile in soil, solution, and in the plant in terms of translocation from roots to shoots [19, 52].

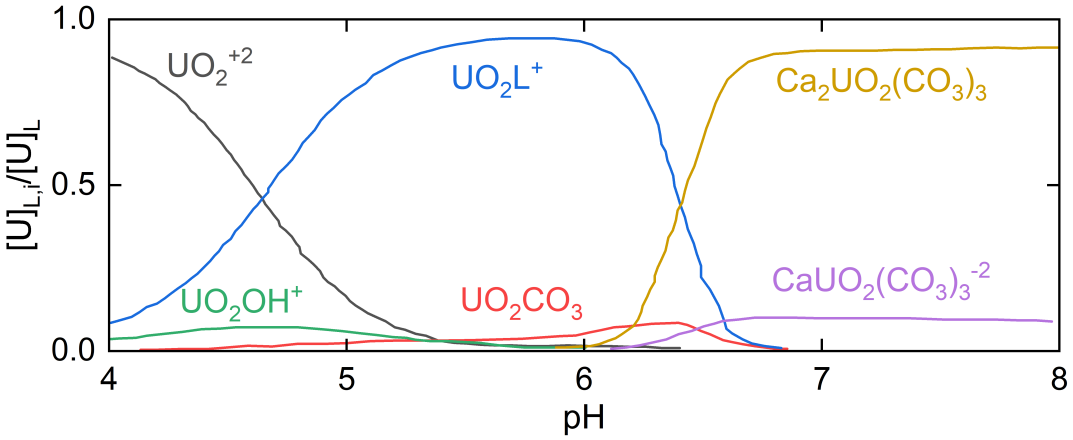

Figure 3.9: The total concentration of various uranium molecules in the liquid soil solution ($[U]_{L,i}$) and the aqueous solution ($[U]_L$) at different pHs. This figure is adapted from Ref. [19].

In previous work, Ebbs *et al.* exposed pea plants to a 5 µ M solution of $UO_2(NO_3)_2$ over 7 days, with pH values in the range of 5.0–6.0. They found that 5 µM of $UO_2(NO_3)_2$ was toxic, resulting in stunted growth and blackened roots. The greatest amount of accumulation of uranium in the shoots was at a pH of 5.0, indicating that

the lowest pH tested in this study resulted in the most mobile uranium species. They further performed a controlled study on the effect of phosphorous on the uptake of UO_2^{2+} and found that phosphate complexation with UO_2^{2+} decreased the uptake of uranium by about 10%. Another work examined how the pH of uranyl nitrate solutions affects the uptake, photosynthetic efficiency, and fluorescence quenching factors measured via PAM-F [159]. *Arabadopsis thaliana* was exposed to a series of uranium exposures from 0–100 µM uranyl nitrate solution under hydroponic conditions. They found that in comparison to a pH of 4.5, the fraction of uranium in the leaves compared to the roots was always higher by a factor of ∼4 at a pH of 7.5 despite greater overall uptake at a pH of 4.5. Ebbs *et al.*, on the other hand, observed the greatest shoot accumulation at lower pHs in pea plants. Furthermore, there was a significant decrease in the Chl *a*, Chl *b*, and Car concentrations at the 4.5 pH in the work by Saenan *et al.*; however, there was no significant change in pigment content during the exposure at a pH of 7.5. Despite the overall decrease in pigment content and inhibited growth, the photosynthetic efficiency increased with uranium uptake at a pH of 4.5, which the authors attribute to energy produced during photosynthesis to be used in defense mechanisms against oxidation by uranium-induced stress as opposed to plant growth.

Previously, it has been shown that uranium exposure leads to oxidative stress in plants [7, 183, 184] even at low concentrations of exposure. Vanhoudt *et al.* found that photosynthetic efficiency increases, while NPQ decreases under uranium stress for *A. thaliana* [184]. However, a decrease in total Chl *a*, Chl *b*, and Car content was observed and signified stress. The decreased NPQ and increased PSII activity proved that uranium-exposed *A. thaliana* can cope with this stress. Aranjuelo *et al.* used several different analysis methods upon exposure of *Arabidopsis thaliana* to uranium: PAM-F, absorption spectroscopy for pigment concentration analysis, and proteomics. In contrast to the prior results, a significant decrease in the efficiency and

function of PSII was observed. The authors also found that ascorbate and glutathione, enzymic proteins, played an important role in the response to ROS produced, such as providing antioxidant defense. Many factors influence the plant response, such as age of plant upon initial exposure, soil or hydroponic solution composition, light exposure, and heavy metal or stress concentration, which can make identification of a specific signature challenging.

Algae are also of interest to biosensing applications due to their abundance and sensitivity to environment. Previous works have explored the efficacy with which various algae species can remove uranium from water systems [65], along with the effect of uranium exposure on the photosynthetic efficiency and function of algae [66, 68, 92]. Similar responses of green algae, which contain the same photosynthetic pigments as leafy green plants, to uranium uptake have been observed. Herlory *et al.* found that exposure of the green alga *Chlamydomonas reinhardtii* to 50 µM concentrations of uranium in the form of uranyl nitrate resulted in reduced photosynthetic efficiency [92]. A similar response was observed by Aranjuelo *et al.* upon uranium exposure to *A. thaliana* [7]. Both Herlory *et al.* and Aranjuelo *et al.* performed analysis with PAM-F. However, other work has found that microalgae can be highly resistant and adaptable to harsh growth conditions, such as extreme pollution from uranium mining [68]. García-Balboa *et al.* found the several microalgae species were able to mutate such that they can tolerate living in highly toxic environments. *Chlamydomonas reinhardtii* and *Dictyosphaerium chlorelloide* were two of the main algae species examined during this study, and it was found that early exposure resulted in death of sensitive cells; however, within 30 days, sexual mutation resulted in adaptation of cells that allowed them to be resistant to the toxic environment. Because of this adaptation to uranium exposure, microalgae may be a promising species for identification of uranium contamination in the environment.

CHAPTER 4

Experimental Investigation of Filament Properties at High Peak Powers

Ultrafast laser filaments [22] have been the subject of great interest due to their broad potential application space, such as remote sensing [47, 70], laser-driven water condensation, FIBS [154, 156], optical waveguiding [168], and air lasing [129, 150]. The complex physics that underlies their formation makes them an area of current ongoing investigation, especially when it comes to controlling the naturally sporadic and stochastic multiple filament structures that can cause shot-to-shot variability. Multiple filamentation is most likely to occur when the laser peak power exceeds 10–$100\times P_{cr}$[15] and form as a result of modulation instability [17] of the laser pulse wavefront in competition between the Kerr effect and diffraction, leading to several plasma cores surrounded by an energy reservoir [173]. Previous studies investigated the robust turbulent properties of long-wavelength multiple filaments for extended propagation in air as light guides [136], reproducibility of multiple filament patterns [15], and structural evolution of multiple filaments in turbulent air [201]. The desire to control the pattern and reproducibility of multiple filaments has led to exploration of the merging of multiple filaments into a "superfilament" by controlling the focusing conditions in air [149] and water [152], generating longer and higher intensity single filaments. Furthermore, the suppression of multiple filament formation has been ex-

plored and it has been found that, under proper focusing conditions and with small beam sizes, multiple filamentation can be inhibited [78]. While significant advancements have been made on this subject, a complete analysis of how the driving laser parameters affect the filament composition, which dictates the guided laser intensity, is lacking.

This chapter presents an investigation of the plasma properties in the multiple filament regime and how they can be controlled to improve analytical techniques such as FIBS. In Section 4.1, the properties of filaments formed at high peak powers, where multiple filamentation occurs, are studied using non-invasive optical emission spectroscopy. Understanding the spatially- and temporally-dependent molecular fluorescence intensity and filament plasma characteristics and how they depend on the controllable input laser parameters is vital for practical applications in remote sensing, air lasing, and multi-filament control. Ultimately, we find that there are minimal differences in electron temperature over the first 10 ns of filament lifetime between the two driving laser wavelengths studied; however, the process leading to formation of different molecular and atomic excited states is different as evidenced by the non-invasive spatially and temporally resolved optical emission spectra. In Sec. 4.2, a genetic algorithm is employed to control the multiple filament structure for FIBS signal enhancement upon ablation of a copper target. Previous work had shown that nitrogen fluorescence from filamentation in air could be enhanced upon correcting an imperfect wavefront; the work presented in this section demonstrates that a wavefront free from aberrations does not necessarily lead to signal enhancement in FIBS. The real-time signal enhancement demonstrated in this work has significant implications for improving detection capability for remote sensing. This chapter includes edited portions from Refs. [59, 60, 64].

4.1 Characterization of multi-filament plasmas in air

This section presents results on non-invasive optical emission spectroscopic plasma diagnostics of filaments formed in air under the multi-filament regime. Several prior studies investigated the spatially-dependent properties of the filament plasma in the single-filament regime for a driving wavelength of 800 nm from a Ti:sapphire ultrafast laser [16, 54, 91, 123, 128]. In other studies, other driving wavelengths of 248 nm [181], 400 nm [45], and 3.9 µm [135] have also been explored. Past research provides clear evidence that different laser wavelengths, beam energies, pulse durations, and focusing conditions can have notable effects on the ionization yield, electron density, and plasma temperature of the filament. For example, Théberge *et al.* [179] have shown that the plasma density and diameter of the filament strongly depend on external focusing conditions. A variety of invasive and noninvasive techniques have been used to measure the electron density in filaments, like terahertz spectroscopy [187], N_2^+ emission intensity [179], interferometry and diffraction [178, 179], Stark broadening [16, 123], and many others [91, 128, 193]. Reported densities range from 10^{15} cm^{-3} [187] to 10^{18} cm^{-3} [179]. In several studies, the plasma temperature of single filaments was measured and reported to range from 3900 K [178] to 5800 K [16, 123]. Techniques used to determine these temperatures include diffraction, interferometry, and the ratios of line intensities. This section presents an analysis of the multiple filament plasma formed in air by observing the axially resolved nitrogen fluorescence from 400- and 800-nm ultrafast laser pulses at various energies. Mechanisms that lead to the measured fluorescence spectrum are suggested, and comparisons of our results to previous measurements of single-filament plasmas are made. Estimates of the filament plasma temperatures and electron densities are made.

4.1.1 Experiment

The experimental schematic can be seen in Fig. 4.1. The laser used was the custom-built Lambda Cubed (λ^3) Ti:sapphire-based chirped-pulse amplification system at the University of Michigan, operating at a central wavelength of ∼800 nm at a 480-Hz repetition rate and with a pulse duration of ∼50 fs. The beam had a 22-mm Gaussian diameter immediately after the compressor. The laser propagated ∼7 m before reaching the silver-coated 1-m focal length ($f/40$) spherical focusing mirror. For the 400-nm filament, the laser was frequency doubled using a β-$Ba(BO_2)_2$ (BBO) crystal, with the remaining 800-nm light being removed using a dichroic mirror. The resulting 400-nm pulse duration was estimated to be 42-fs long based on the pulses at 800 nm measured via frequency-resolved optical gating. Spectroscopy was performed using a 25.4-mm diameter, 30-mm focal length lens coupled to a 400-µm optical fiber, which was connected to a 0.55-m Czerny-Turner spectrograph (Horiba Jobin Yvon, iHR550), and an intensified charge-coupled device (ICCD) detector (Andor, iStar 334T). The spectroscopic system resolution was measured to be ∼40 pm at 632.8 nm. For side imaging of the filament, an electron-multiplying intensified charge-coupled device (EM-ICCD) (Princeton, PI-MAX4) was used with an objective lens. To isolate N_2^+ emission, a 50.8-mm diameter, 391.4-nm bandpass filter with a 1.4-nm FWHM-bandwidth (Andover) has been placed in front of the camera objective. The inset of Fig. 4.1 shows an example radial profile of the multiple filament cores inferred from the damage on a copper target placed at the geometric focus of the spherical mirror from a single 3-mJ, 400-nm pulse. The range of peak powers used in this study is 20–80$\times P_{cr}$ at 800 nm, and a single peak power of 140$\times P_{cr}$ for 400 nm is used. The critical powers for self-focusing of 400- and 800-nm are estimated to be 0.5 and 3 GW, respectively [26]. All experiments were conducted in air.

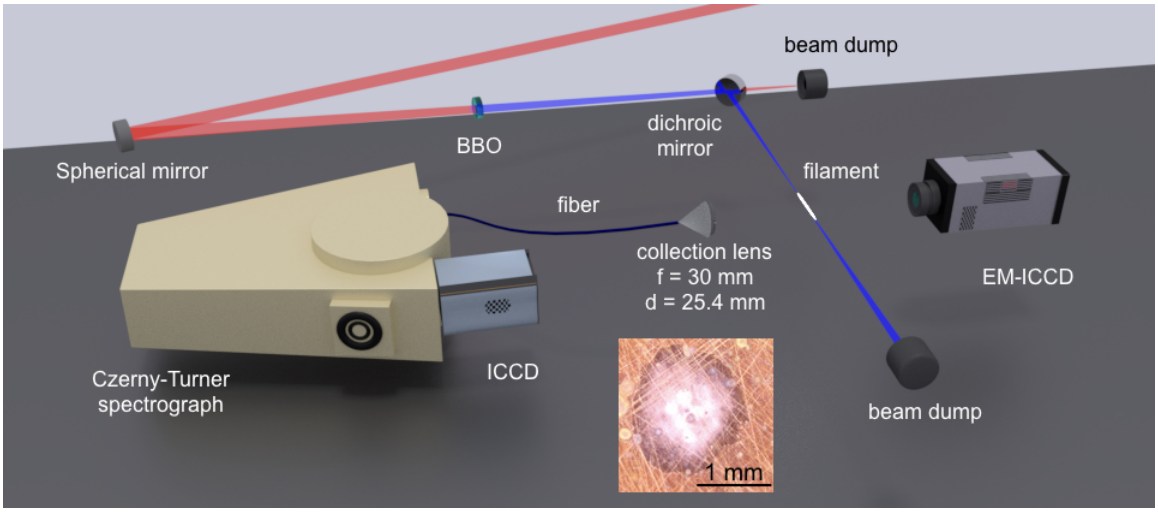

Figure 4.1: Schematic of the experimental setup. The inset image shows an example radial profile of the multiple filament cores (bright spots) observed from the damage on a copper target (3 mJ, 400 nm). The copper target was placed near the geometric focus of the spherical mirror. The damage pattern is from a single laser shot [64].

4.1.2 Results & Discussion

The optical emission from filament-air plasmas contain two dominant nitrogen fluorescence systems, as seen in Fig. 4.2. The first of them is the N_2 second positive system ($C^3\Pi_u \rightarrow B^3\Pi_g$), where the upper excited levels of N_2 are populated indirectly by recombination of electrons with N_4^+ [193, 194]. The second is the N_2^+ first negative system ($B^2\Sigma_u^+ \rightarrow X^2\Sigma_g^+$), where the inner-shell ionization of N_2 by multiphoton and tunnel ionization populates the excited states of N_2^+ [194]. The (x_u, x_ℓ) notation in Fig. 4.2 refers to a transition from a vibrational state in the upper level (excited) electronic state (x_u) to a vibrational state in the lower level electronic state (x_ℓ); for example, (0,0) represents a direct transition from the ground vibrational state in the upper electronic level to the ground vibrational state in the lower electronic energy level. According to Fig. 4.2, the peak of the 337-nm (0,0) band-head from the N_2 second positive system is 2.6× more intense for the 800-nm filament than for the 400-nm filament, both driven by 3-mJ pulses. On the other hand, the peak intensity of the 391-nm band-head arising from the N_2^+ first negative system (0,0) transition is 4.4×

greater for the 400-nm filament than for the 800-nm filament. It is well understood that multiphoton ionization is increasingly probable for decreasing laser wavelength, where the individual photon energy increases. Daigle *et al.* performed a similar experiment in the single-filament regime with 800- and 400-nm input laser energies of 2.3 mJ focused using a 15-cm focal length lens, and reported a 6.4× higher intensity for the 391-nm peak when using 400-nm compared to 800-nm driving wavelength; however, the N_2 emission was observed to be constant for both wavelengths. The equal N_2 emission between the two wavelengths is attributed to similar total ionization yields at 400 and 800 nm [45]. Identical N_2 emission between the two wavelengths is not observed in our case using looser focusing conditions and entering the multiple filament regime for laser peak powers $20\times P_{cr}$ and $140\times P_{cr}$ at 800 nm and 400 nm, respectively. The increased N_2^+ emission may be explained by higher efficiency for inner-shell ionization of N_2 in the 400-nm case, leaving a larger fraction of N_2^+ in the excited state, which may also contribute to the lower observed N_2 emission.

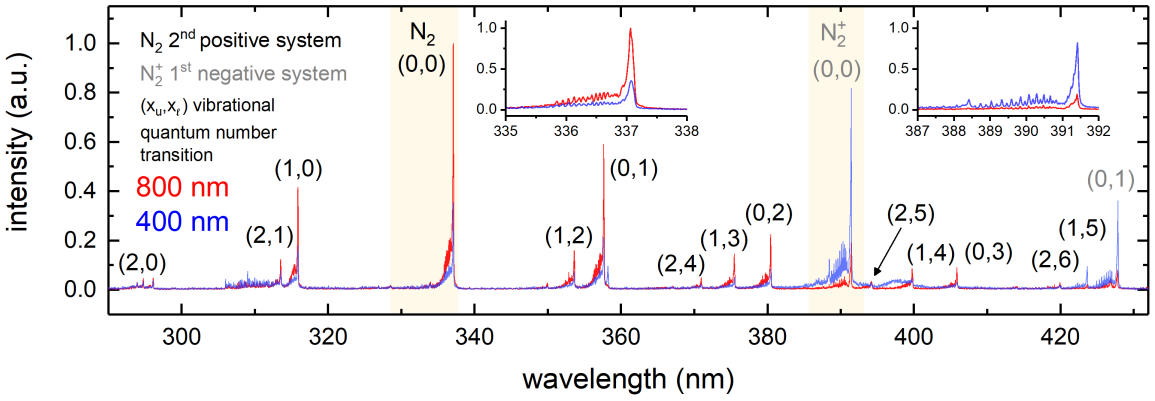

Figure 4.2: Measured emission spectrum of the N_2 second positive system and the N_2^+ first negative system for 3-mJ pulses at 400 nm (blue) and 800 nm (red) measured 20 mm before the geometric focus in the direction of beam propagation. The ICCD delay and gate width were 0 ns and 10 ns, respectively, measured with respect to arrival the incident laser pulse at the filament position. The shaded regions highlight the two molecular band-heads primarily discussed [64].

The spatiotemporal dependence of the filament plasma emission is explored with gated side-on imaging in order to gain more insight into the distribution of ionic

species and the axial distribution of plasma properties. The filament lifetime is measured by the side-view optical emission intensity distribution at 1-ns intervals, as shown in Fig. 4.3. The total emission dissipates over a period of ∼5 ns, in agreement with previous measurements of the filament lifetime [145] as well with the more recent measurements of the surrounding magnetic field, which suggest a 5–6 ns lifetime [34]. The decay of total emission intensity in Fig. 4.3 can be used to infer the temporal evolution of plasma temperature and density. Moreover, Fig. 4.3 provides information on the spatial distribution of the plasma emission. The rapid decay and spatial distribution of the total optical emission motivate subsequent exploration of the behavior and mechanisms governing air ionization in the filament. In this way, the plasma characteristics determined under various controllable laser parameters when multiple filaments form can be compared with those reported in previous studies where single filaments were investigated.

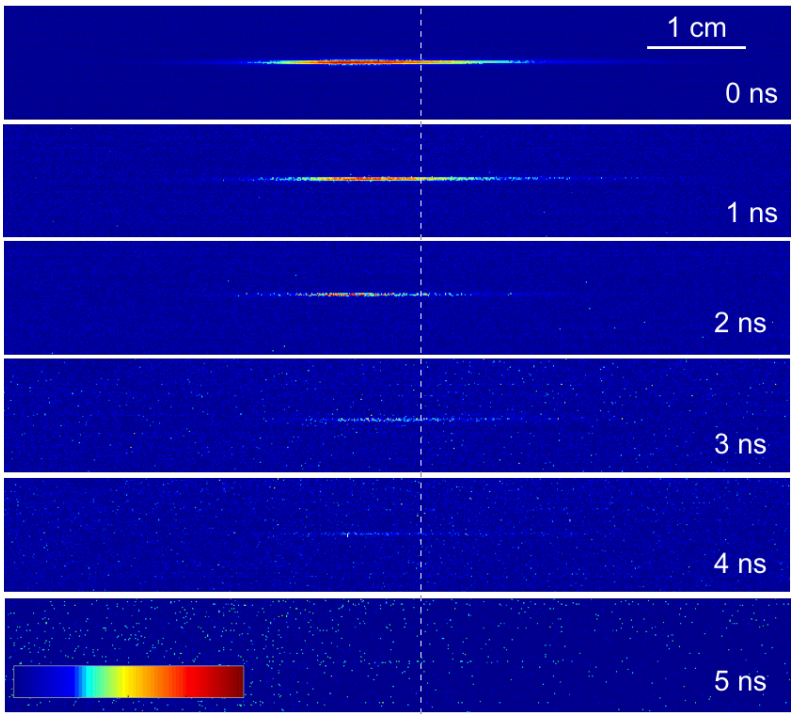

Figure 4.3: Time evolution of the filament plasma measured by side imaging for 3-mJ, 800-nm pulses. The gate widths for each time step were 1 ns with 100 accumulations. The white dashed line represents the geometric focus of the spherical mirror [64].

The spatial distribution of the 391-nm N_2^+ from the filament plasma is examined in Fig. 4.4. The brightest emission occurs before the geometric focus represented by the dashed line in Fig. 4.4, demonstrating the contribution of self-focusing. The 391-nm emission shown in Fig. 4.4(c) and (f) displays a similar axial profile to the total emission, as can been seen in Fig. 4.4(a) and (d), implying similar emission trends for N_2 and N_2^+. The emission diameter from the filament plasma increases from ~600 µm with 3 mJ to ~800 µm with 12-mJ driving laser energy, respectively. The plasma channel length also increases from ~57 mm to ~85 mm. The large diameter of emission compared to the previously reported filament core diameters of ≤100 µm [15, 179] is attributed to the formation of several filament cores; the increased diameter with greater input laser energy implies the formation of more cores with increased laser peak power.

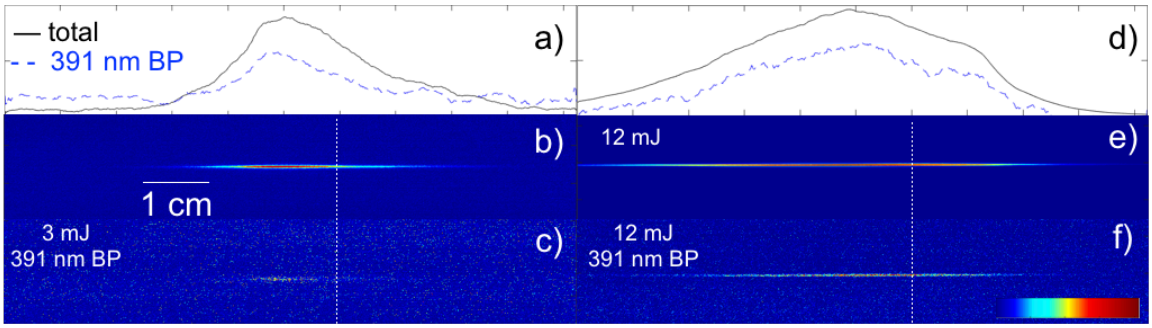

Figure 4.4: Side imaging of the total and N_2^+ emission from the 800-nm filament with 3 mJ (a)–(c) and 12 mJ (d)–(f) laser energies. Profiles (a) and (d) show the vertically-integrated emission. Images (b) and (e) show the total emission. Images (c) and (f) show the 391-nm emission with a 1.4-nm FWHM bandpass (BP) filter. The white dashed line represents the geometric focus of the spherical mirror. Images were recorded at a delay of 0 ns with respect to the incident laser pulse, gate width of 10 ns, and accumulated for 100 laser shots [64].

Assessing the axially resolved and energy-dependent optical emission spectrum helps to identify the excitation pathways that produce this distribution of species. The axial position is measured with respect to the geometric focus of the spherical mirror (0 mm). The maximum intensities for the 391-nm and 337-nm band-heads in the spectra occur 10 mm before geometric focus for both 400- and 800-nm beams, as

seen in Fig. 4.5. The 337-nm N_2 emission dominates for 800-nm, while the 391-nm N_2^+ emission dominates for the 400-nm filament, which is consistent with the result of the spectra shown in Fig. 4.2. Figures 4.5(a) and (b) show that both N_2 and N_2^+ emission bands follow similar trends along the filament axis. While the nitrogen molecular emissions peak near the same location, O I peaks at the geometric focus for 400 nm and 5 mm behind the geometric focus for 800 nm. The different axial distribution of O I emission as distinguished from that of N_2 and N_2^+ implies a different origin for O I excited species. Consequently, plasma processes, (*e.g.*, collisional or thermal dissociation and excitation), may cause the O I emission to peak at an axial position beyond the region of maximum filament intensity along the beam propagation direction. Results from previous work on temporal plasma emission characteristics illustrated that atomic lines of N and O in filament plasmas appear after both N_2 and N_2^+ emissions and after the decay of continuum emission [99], suggesting further that collisional interactions in the plasma result in atomic O-I emission. The axial gradient (dI/dz) is highest for the 337-nm band-head for both filaments at the beginning of the filament formation, as seen in Fig. 4.5(c) and (d). Previous work indicates that the N_2 337-nm emission band-head has a longer persistence ($\sim$1 ns) than the N_2^+ 391-nm emission band-head ($\sim$400 ps) [99]. This is primarily due to the means by which each upper level is pumped: photoionization and collisional processes for the N_2^+, and solely collisional processes for the N_2. The axial gradient in the excited N_2 population is greater for the 800-nm filament than for the 400-nm case. The different axial gradients for each wavelength may imply different excitation and ionization paths for the two driving laser wavelengths.

Diagnostics of the optical emission are performed in order to determine the axially-resolved plasma properties and how they vary with incident laser parameters. The experimental nitrogen spectra are fit using SPECAIR [1] in order to determine plasma temperatures, assuming Boltzmann velocity distributions. The individual tempera-

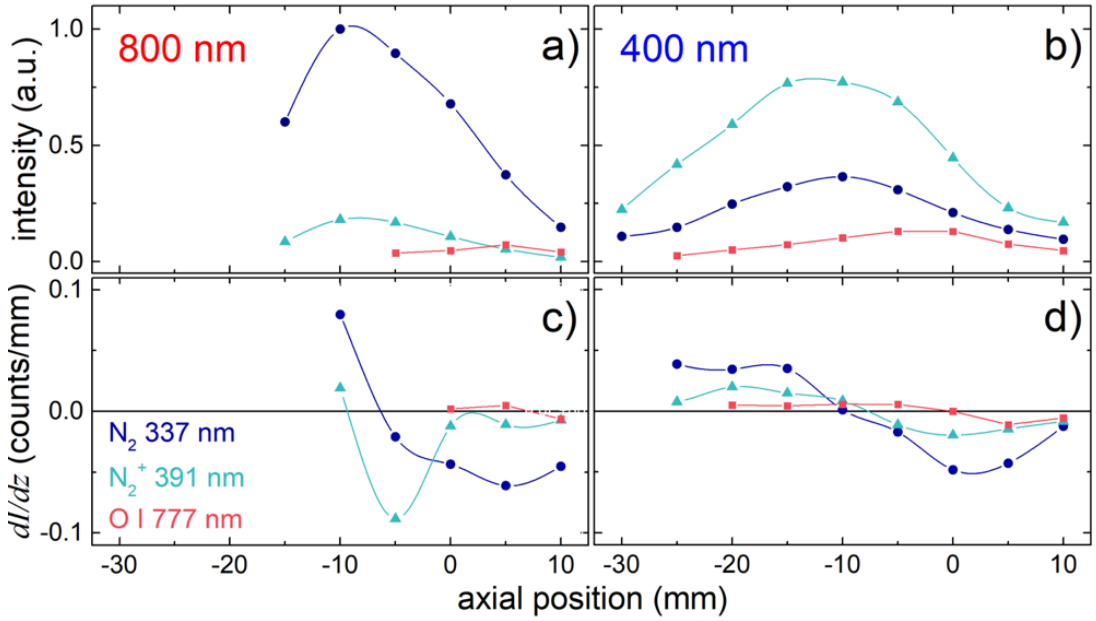

Figure 4.5: Measured peak intensities for the N_2(337 nm) and N_2^+(391 nm) bandheads, and O I (777.19 nm) line from the (a) 800-nm and (b) 400-nm filament spectra and axial gradients (dI/dz) for the measured intensities of each band and line for the (c) 800-nm and (d) 400-nm filaments. Driving laser pulse energy was 3 mJ for both wavelengths. Geometric focus of the spherical mirror is denoted as 0 mm. Data is fit with a spline curve to help guide the eye [64].

tures are iteratively varied to approximate the assumed case of incomplete or partial local thermodynamic equilibrium (LTE). Temperatures are derived from a "best fit" by minimizing the residuals between the experimental and simulated spectra. Figure 4.6 shows an example of experimental and simulated spectra used to estimate rotational (T_r), vibrational (T_v), and electronic temperatures (T_e).

As stated previously, a variety of methods, both invasive and non-invasive, have been used to date to estimate and measure the electron density in transient filament plasmas. Here the degree of Stark broadening for the O I 777.19-nm line is measured as a non-invasive method for evaluating electron density. Figure 4.7 shows a sample multi-Voigt fit that combines the natural and Stark broadening (Lorentz shape) and instrumental and Doppler broadening (Gaussian shape) that determine the measured

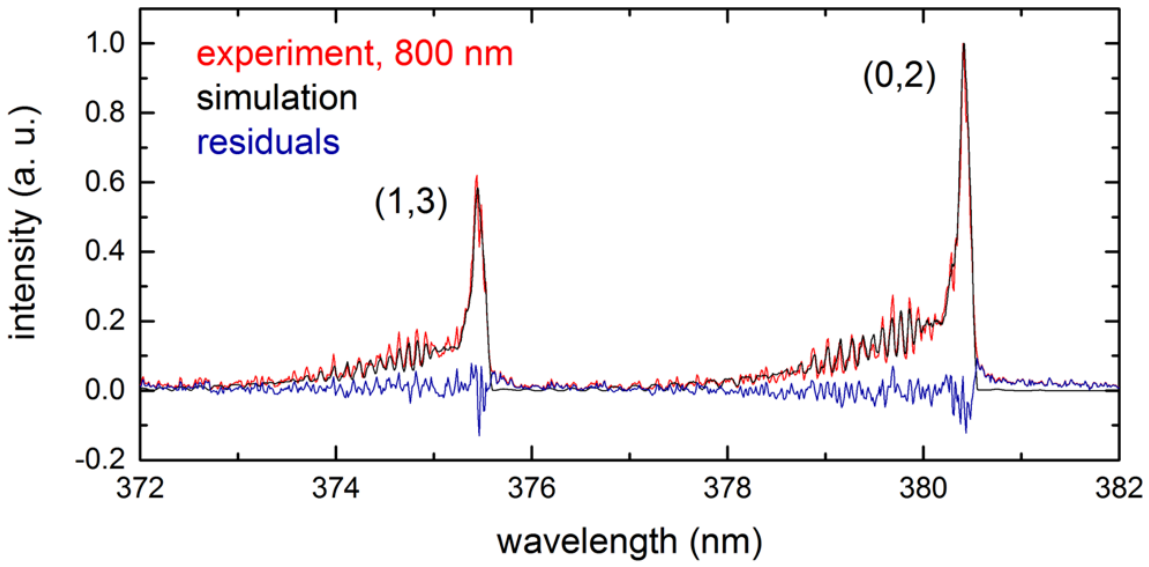

Figure 4.6: Spectrum measured with 3-mJ, 800-nm pulses and simulated by SPECAIR for the (1,3) and (0,2) N_2 emission bands [64].

line shape and line width. Natural broadening is assumed negligible in comparison to the measured line width. Instrumental broadening for the spectroscopic system is measured using a Hg-Ar source, and Doppler broadening is calculated using the electron temperatures from SPECAIR ($w_{\text{Doppler}} = 7.2\times10^{-7}\lambda_0\sqrt{T_e/M}$, where w_{Doppler} is the Doppler half-width, λ_0 is the line center, and M is the mass of the emitter). These contributions are subtracted from the full width at half maximum (FWHM) from the Voigt fit of the selected spectral lines, isolating the Stark broadening contribution. Assuming negligible broadening from ions in the plasma, the electron density can then be estimated from [75]

$$n_e = \left(\frac{\Delta\lambda_s}{2a}\right) \times 10^{16}\ \text{cm}^{-3}, \tag{4.1}$$

where $\Delta\lambda_s$ is the Stark broadening contribution to the FWHM (nm) and a is the elec-

tron broadening parameter (nm) for that species at a particular wavelength. Bernhardt *et al.* [16] performed a dedicated study to determine the electron broadening parameter for O I 777.19-, 777.42-, and 777.54-nm lines, finding it to be 16.6 pm for all three lines in a single-filament plasma with input beam energies up to 2 mJ. Electron densities calculated using this value for a are presented in Fig. 4.8 and Table 4.1.

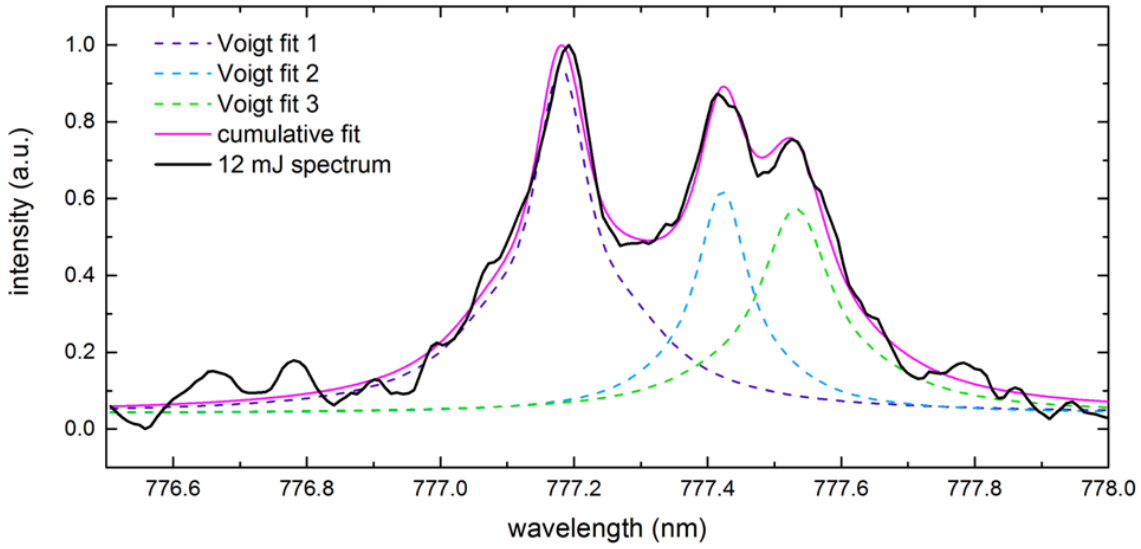

Figure 4.7: Sample multi-Voigt fit for the O I 777.19-, 777.42-, and 777.54-nm lines used to determine the degree of Stark broadening. The spectrum shown is taken for 800-nm with driving laser energy of 12 mJ [64].

Axially resolved T_r, T_v, and T_e are shown in Fig. 4.8; temperatures vary less than 10% along the axial distance. The temperatures are found to be unequal, implying the filament plasma is not in complete LTE, which may contribute to the calculated errors in the fits seen in Fig. 4.8. The temperatures, however, are comparable to those previously reported for single filaments where LTE is assumed [16, 98, 123]. While the electronic temperature is most commonly used for characterizing plasmas, it is interesting to note that T_r and T_v primarily determine the appearance of the

(2,5) N_2 vibrational band. The average T_r and T_v are ∼900 K and ∼3300 K for the 800-nm filament, and ∼1150 K and ∼2300 K for the 400-nm filament. The lower T_v in the 400-nm plasma indicates that the higher lying (2,5) vibrational transition is less probable than transitions involving lower lying vibrational levels in the upper electronic state. Vibrational partition functions are calculated in order to determine how many accessible vibrational states there are at each respective temperature. Vibrational energy levels are described by the harmonic oscillator model, hence T_v can be determined as follows:

$$T_v = \frac{hc\nu}{k}, \tag{4.2}$$

where h is Planck's constant, ν is the vibrational frequency of the diatomic molecule, and k is the force constant. The simplified vibrational partition function is

$$q_v = \frac{1}{1 - \exp(-h\nu/kT_v)}, \tag{4.3}$$

where q_v is the partition function that gives the number of accessible vibrational states. Using $h\nu = 2358$ cm^{-1}, $k = 22.94$ dynes cm^{-1} [9], and T_v as 2300 K and 3300 K, q_v is ∼23 and ∼33 for the 400- and 800-nm filaments, respectively. The lower partition function for the 400-nm case suggests that fewer vibrational states are accessible. Since the (2,5) transition is already weak in the 800-nm spectrum, it is likely that the decrease in accessible states suppresses this transition.

Figure 4.8(d) shows the axially-resolved electron densities, where the maximum is near the geometric focus. The electron density distribution provides further evidence that plasma processes may be the dominant cause for the dissociation and excitation of oxygen. The dissociation energy for O_2 is ∼5.1 eV at room temperature from the ground vibrational state. Dissociation of O_2 at 5000 K is possible from O_2-O_2 and e^--O_2 collisions, and is especially likely when O_2 is in an excited vibrational state [93]. The photoabsorption cross-section which dictates the dissociation of O_2 significantly

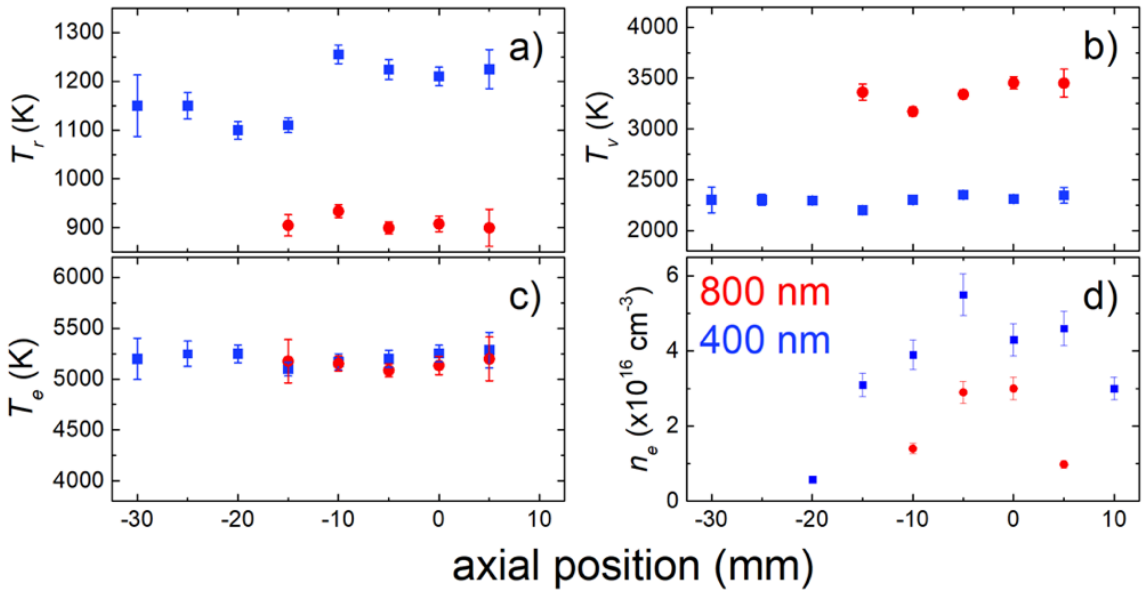

Figure 4.8: Axially-resolved (a) rotational temperatures (T_r), (b) vibrational temperatures (T_v), (c) electronic temperatures (T_e), and (d) electron densities (n_e) along the filament length. Geometric focus of the spherical mirror is at 0 mm. Results shown are for 3 mJ energies with both 400- and 800-nm beam wavelengths [64].

decreases with increasing wavelength, and most photo-dissociative processes occur below 400 nm [55]. Therefore, it is possible that multiphoton dissociation of O_2 by 400- and 800-nm pulses is not the main process for production of O I. It is observed that the optical emission in Fig. 4.5 peaks in the region before the maximum electron density is reached, while the temperatures remain fairly constant along the length of the filament. Similar observations about electron temperature were reported by Liu *et al.* [123] in the single-filament regime, where the average and maximum temperature were similar (within ~6%). Further work is necessary to understand more details in the process of filament interaction with air, which causes the maximum electron density to occur at a different position along the filament axis than the maximum molecular optical emission intensity. The processes that may play a role in explaining this difference include the spatial evolution of the filament profile (including the

filament core and reservoir), compression of the laser pulse while propagating along the filament, and the gradual decrease of laser pulse energy along the filament.

The McWhirter criterion [133], which states $n_e \geq 1.6 \times 10^{12} T_e^{1/2} (\Delta E)^3$, where ΔE is the largest gap between adjacent energy levels, is evaluated. For an energy gap of 1.78 eV [123] and electronic temperature of 5000 K, the minimum electron density required to satisfy the criterion is 6.4×10^{14} cm^{-3}. The measured densities, on the order of 10^{16} cm^{-3}, satisfy the McWhirter criterion, implying the density is sufficiently high for the electrons to be in LTE. However, the different measured rotational, vibrational, and electronic temperatures suggest that the LTE conditions may differ between subsets of particles, (*e.g.*, electrons vs. neutral or ionic molecules in the excited state). For transient and inhomogeneous plasmas, such as laser-produced [42] or filament plasmas, further studies are required to verify the existence of equilibrium conditions.

Table 4.1: Driving laser energy- (E_λ) and wavelength- (λ) dependence of filament optical emission and plasma properties. Energy is given in mJ. Intensity ratios ($I_{N_2}/I_{N_2^+}$) and peak emission (I_{peak}) compare the emissions from N_2(∼337 nm) and N_2^+(∼391 nm) (0,0) band-heads at the axial peak of the optical emission. Plasma temperatures are also given at the axial peak of the optical emission in units of K. Electron densities are calculated from Stark width parameters measured for filaments [16] and given in units of cm^{-3}. [64].

$E_{800\text{ nm}}$	$I_{N_2}/I_{N_2^+}$	I_{peak}	T_e	n_e
3	5.5	9.9×10^5	5180±120	1.2×10^{16}
6	5.4	2.2×10^6	5160±100	2.2×10^{16}
9	5.2	3.3×10^6	5230±110	2.2×10^{16}
12	4.9	4.1×10^6	5290±120	2.7×10^{16}
$E_{400\text{ nm}}$	$I_{N_2}/I_{N_2^+}$	I_{peak}	T_e	n_e
3	0.5	9.6×10^5	5100±70	3.9×10^{16}

Table 4.1 presents T_e at the axial peak of the filament emission for various laser parameters. Electronic temperatures do not increase significantly with input beam energy, while the peak optical emission intensity (I_{peak}) does. Table 4.1 gives the peak emission at a single axial position, which is distinguished from the total emission of

the plasma. In Fig. 4.4, it is observed that the diameter and length of the emission increases with energy. A clamped laser intensity implies that the plasma emission also reaches a maximum. The increasing peak emission at this axial position therefore implies the formation of additional plasma cores. This observation is supported by the increased diameter of the emission observed in Fig. 4.4 between 3 mJ and 12 mJ incident laser energies, from 600 to 800 µm. Becker *et al.* [12] observed an analogous relationship between total optical emission and beam energy under different experimental conditions for various high pressures. Constant temperature with increasing emission intensity may also be a consequence of multiple filamentation, where multiple cores contain more total emitters, but each may have a similar temperature. However, single-shot measurements are necessary to disambiguate the temperatures of individual cores. Also, the temperatures presented in this study are determined from averaging the emission of 1000 shots, smearing the sporadic behavior typical for multiple filamentation.

The fraction of ions in the excited state also increases with beam energy, as seen by the decrease in intensity ratio between 337 nm and 391 nm ($I_{N_2}/I_{N_2^+}$) in Table 4.1. Approximately 11 photons at 800 nm are needed for MPI of N_2[45]. The greater laser intensity at higher pulse energies increases the probability of multiphoton inner-shell ionization of N_2, which emits the 391-nm band. The 400-nm pulses produce a larger fraction of ions in the excited state than 800-nm pulses, since fewer photons are required to ionize N_2; the increasing fraction of ions in the excited state correlates to the increasing electron density. The n_e values in Table 4.1 agree with those calculated in [16], where the values on order of 10^{16} cm^{-3} were obtained with 2-mJ, 800-nm pulses with varying focal length lenses. This is also consistent with results from [179], where n_e was deduced from the intensity of the 391-nm peak. In addition, the authors reported that the plasma density in the filament increases slowly with beam energy in the single-filament regime. Similar slowly increasing electron densities with

incident beam energy in the multiple-filament regime are observed in this work. A larger electron density in the 400-nm case when compared to the 800-nm case is also observed, which is consistent with the expectation that at 400 nm the probability of MPI is greater [26, 45, 181].

4.2 Wavefront control of multi-filament structures

The ability to control the properties of multiple filaments, such as configuring them into reproducible patterns or even suppressing them to create a single *super-filament* [78, 149], is of significant interest for remote sensing applications. One method to realize this control is by the use of axicon lenses to form a Bessel beam profile, which is known to create longer and more stable filament structures at high laser powers [166]. A drawback to this approach is the higher energy needed as a result of a smaller fraction of the beam energy contributing to filamentation. Furthermore, one can use diffraction from a circular aperture to control the filament stability and axial formation position [41]. It has been shown that beam aberrations can be reduced by shaping the beam amplitude profile [106]. The stability of the backscattered signal from filamentation in air can also be improved by reducing the beam diameter [112]. Previous work has shown that spatiotemporal control of filamentation can improve the signal intensity through adjustment of pulse chirp, which can influence FIBS detection limits [25, 200]. Modification of the laser spectral phase has been used to establish precise control over the filament onset location [90]; however, this approach has not shown promise for controlling the transverse filament structure.

Adaptive optics, on the other hand, can be used to modulate the beam phase profile. An example of the use of adaptive optics to control filamentation is the use of a SLM, which can seed a multi-filamentation pattern by encoding a cluster of microlenses into the beam profile [20]. The spatial phase can be adjusted using phase masks or optical diffractive elements [40] or SLM-based pulse shapers, which has been

shown to regulate the spatial location of filament formation [90]. A deformable mirror (DM) has been used to control the delivery of filaments to the desired location through wavefront manipulation [53, 88]. In previous work, filament length was shown to increase through application of spherical aberration from wavefront adjustment by a DM [100]. Astigmatism also increases the filament length and eventually causes a single filament to separate into two filaments along the beam propagation direction [50]. It has been shown that wavefront optimization using a DM can increase the signal of N_2 fluorescence from filament plasma emission by a factor of seven [46]. Therefore, it may be possible to use the signatures contained in the optical emission spectrum produced via filament ablation of a solid target to optimize the filament-solid interactions and generate a more intense characteristic spectroscopic signal. The goal of this study has been to determine whether the shaping of the beam phase profile can provide a significant increase in the intensity of the spectroscopic signal to increase the remote FIBS detection distance.

FIBS on a solid copper (Cu) target is performed and the area under the Cu I 521.8 nm (atomic) line is used as the figure of merit (FOM) for signal optimization in a GA. The wavefront is measured before and after optimization in order to quantify the phase adjustment that increases the FIBS signal intensity, and the resulting changes in the beam profile and filamentation pattern are discussed. The Cu signal intensity approximately triples through the wavefront optimization for two separate trials of the GA, reaching a relative maximum at $\sim$450 iterations.

4.2.1 Experiment

A Ti:sapphire chirped-pulse amplification system was used, operating at a central wavelength of 790 nm, 480 Hz (chopped to 80 Hz to match the data acquisition rate of the camera used in the experiment), 70-fs (for trial 1) and 40-fs (for trial 2) pulse duration, and an energy of 7 mJ, which provides a sufficiently high peak power to

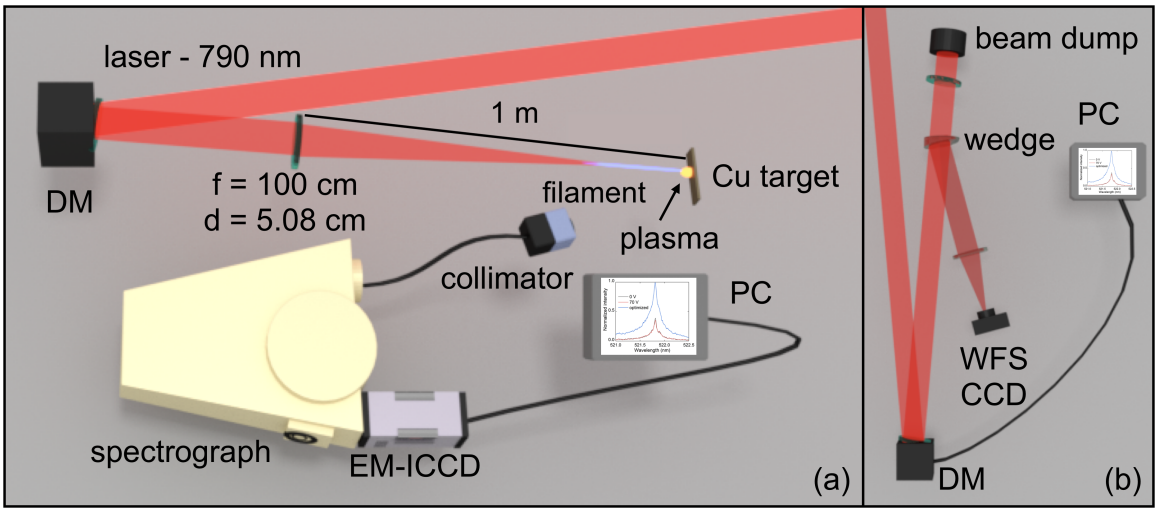

Figure 4.9: (a) Experimental setup used during real-time GA optimization; (b) diagnostics for post-experiment analysis, including the wavefront sensor (WFS) and charge-coupled device (CCD) for measuring the wavefront and beam profile, respectively (not to scale) [60].

observe multiple filaments [169]. The two pulse durations were selected to determine the dependence of peak power on the optimization process and final filament structure produced. A schematic of the experimental setup can be seen in Fig. 4.9(a). The Gaussian beam diameter was 44 mm, and the beam was focused using a 1-m focal length, 5.08-cm diameter lens ($f/20$) to form a filament. The filament plasma channel length as visible to the eye is $\sim$3 cm in length and starts approximately 1 cm prior to geometric focus. The Cu target (CopperLabs, LLC. 99.9% Cu, 24 gauge/16 oz.) was placed at geometric focus and was moved continuously throughout the experiment to expose fresh surface to the filament. The optical detection system consisted of a variable fiber-coupled collimator (Andor CC52) placed 15 cm away from the target at a 30° angle with respect to its normal, coupled to a 0.55-m Czerny-Turner spectrograph (Horiba Jobin Yvon iHR550) and an electron-multiplying intensified charge-coupled device (EM-ICCD). An 1800-l/mm grating (resolving power of 16000, with a resolution of 40 pm at 632.8 nm) was used. A 5.08-cm diameter DM (AOA Xinetics, 37 actuators) is used, and the voltages applied to the actuators were controlled via a custom GA algorithm written in Python, where the FOM is the background-subtracted

area under the Cu I 521.8 nm atomic spectral line. Each spectrum was obtained as an average over 5 laser shots, and the GA analyzes 50 spectra corresponding to 50 DM surfaces. The DM surfaces corresponding to the five largest FOMs were used to generate the next population in the algorithm through a random mutation process. This process is referred to as a single iteration, and each iteration takes ∼30 s. The laser beam propagated over a distance of 1.5 m after the DM prior to reaching the focusing lens. The schematic of the diagnostics component of the setup is shown in Fig. 4.9(b). The beam wavefront was recorded after the FIBS optimization by reapplying the previously recorded DM actuator settings. A 7.62-cm diameter, 3° fused silica wedge was placed before the $f/20$ focusing lens to partially reflect the beam, which was then imaged using a 30-cm focal length, 5.08-cm diameter ($f/6$) achromatic lens onto the Shack-Hartmann wavefront sensor (WFS), or onto the CCD to record the beam profile. The object plane for imaging was the entrance face of the $f/20$ focusing lens used for producing the filament. The initial and final wavefront are measured by using a flat wavefront as a reference, and extract the Zernike coefficients using the Frontsurfer software [142] to determine the nature of phase adjustment that results in signal enhancement.

4.2.2 Results & Discussion

The GA was run under two different trials, where the pulse duration in trial 1 was 70 fs, and in trial 2 it was 40 fs, in order to examine the sensitivity of the optimization process to the initial peak power and spectral phase. The pulse duration was changed by adjusting the compression gratings separation and was measured at the output of the compressor. Figures 4.10 (a) and (b) show the FOM progression of the largest FOM per iteration for both trials. The starting voltage of the DM actuators for the GA was set to 70 V. This is because the linear regime of operation for voltage-to-stroke (µm) conversion was 40–100 V, where 70 V is in the middle of that range.

Therefore, iteration (It.) 0 is the signal produced when the DM has 70 V applied across the entire surface. Although the paths to optimization are dissimilar, both reach an enhanced FOM that is approximately 3× the starting FOM. Figure 4.10(c) and (d) present the spectra recorded at the initial position of the DM (It. 0) and the DM surface resulting in 3× enhancement (It. 450) for trial 1 and trial 2, respectively. While it is possible for the signal to increase beyond ∼450 iterations, the algorithm is computationally expensive and limited by the speed of extracting data from the EM-ICCD software. For this reason, once the relative standard deviation, or σ/μ, of the FOM over 25 iterations is approximately 0.025 or less, the change is determined to be negligible and the algorithm is terminated. Not only is the peak signal intensity higher for the optimized mirror settings, but the linewidth also increases as compared to the initial setting for the DM. The linewidth of the peaks are determined by manually measuring the full width at half maximum (FWHM), and present the results in Table 4.2. The broader linewidth corresponds to increased Stark broadening [16, 76], which can be attributed to increased electron density in the plasma.

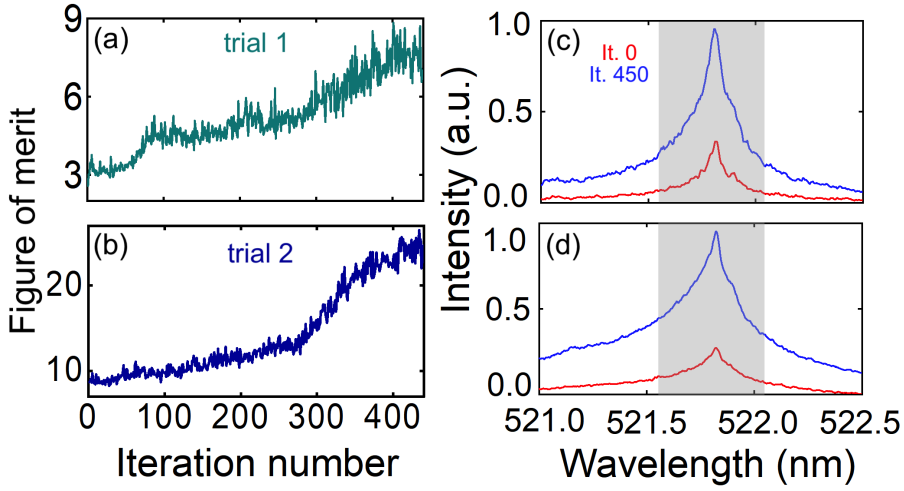

Figure 4.10: (a) Figure of merit progression during GA optimization for trial 1 and (b) trial 2; (c) spectra recorded for It. 0 (70 V applied to all DM actuators) and the enhanced actuator settings for the maximized figure of merit (It. 450) for trial 1 and for trial 2 (d). The spectra were recorded at a delay of 50 ns after the pulse arrival and with a gate width of 2 µs. The shaded region highlights the area used for the FOM [60].

Figure 4.11 contains a broader region of the spectrum to provide a better representation of how the plasma properties vary in the investigated conditions recorded for trial 2. The signal intensity also increases for two other atomic lines at 510.55 nm and 515.32 nm, supporting the hypothesis that the laser coupling to the target is more efficient, *i.e.* mass removal is greater, under ablation with the optimized DM surface. It is worth noting that the ionic Cu (Cu II 481.29 nm) line is observed, and it is more apparent in the spectrum at It. 450 than in the spectrum recorded for It. 0. Ionic lines are seldom observed in filament-induced plasma emission due to the generally lower temperatures they produce when compared to plasmas produced by nanosecond or direct femtosecond laser interactions [81]. It is also important to note that the continuum emission is more prevalent at It. 450 compared to It. 0 at the same time delay. Continuum in plasma emission generally is dominant at early times when the plasma temperature is high, and mostly results from free-bound electron de-excitation through recombination and bremsstrahlung. Appearance of continuum at this delay for It. 450 implies the continuum lifetime is longer, which affirms the conclusion of a higher plasma temperature. Observation of continuum and ionic emission features therefore further supports the argument of greater energy deposition at the sample surface, generating a higher plasma temperature that is capable of producing ions, at the optimized DM surface than at the initial mirror surface, where the ionic feature has much lower intensity.

The reproducibility of the FIBS signal was assessed by recording 25 single-shot spectra during ablation of Cu at the initial and optimized DM surfaces and consider the fluctuation around the mean in the total peak area for the 521.8-nm line. The relative standard deviation (ν) is calculated as $\nu = (\sigma/m)\times 100$, where σ is the standard deviation in the area under the peak and m is the mean area under the peak, is calculated. The ν values are 17% and 12% for It. 0 and It. 450, respectively. It is determined that this relatively small improvement of signal stability is not a notable

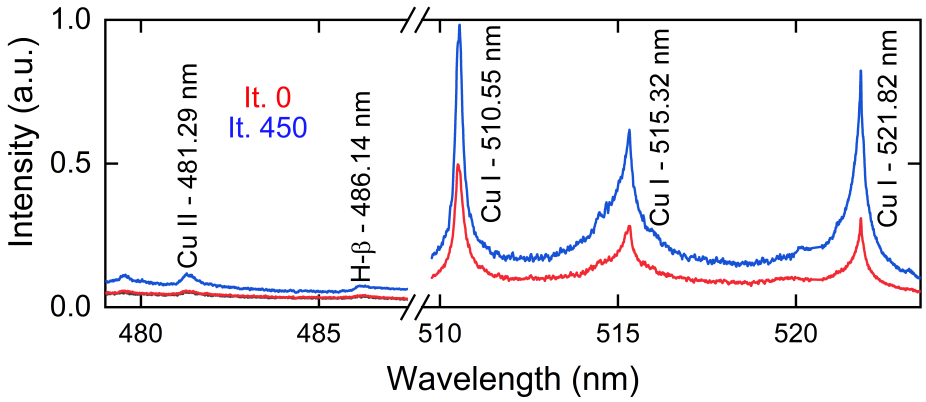

Figure 4.11: Representative broad spectral region including ionic and atomic lines of the Cu optical emission produced from filament ablation. Spectra are recorded at a delay of 50 ns and with a gate width of 2 µs [60].

benefit of this method.

Table 4.2: Linewidths measured as baseline subtracted FWHM for both It. 0 and It. 450 experimental spectra measured for GA FIBS signal optimization.

Spectrum	Peak (nm)	Linewidth (nm)
It. 0	510.55	0.264
	515.32	0.508
	521.82	0.236
It. 450	510.55	0.286
	515.32	0.592
	521.82	0.312

Next, the wavefront was recorded at It. 0 and It. 450 for trial 1 and trial 2. The Zernike coefficients (|A|) are shown in Fig. 4.12(a) and (d); the aberrations can be identified by the radial degree (N) and the azimuthal degree (M) associated with Zernike polynomials Z_N^M. The aberrations that become dominant in both trials are vertical astigmatism (Z_2^2), horizontal coma (Z_3^1), and secondary astigmatism (Z_4^2). While starting with a different phase profile at It. 0 (Fig. 4.12(b) and (e)), the phase profiles at It. 450 are similar ((c) and (f)). Furthermore, it can be noted that the nearly flat wavefront at It. 0 in Fig. 4.12(b) does not result in the greatest signal intensity. Previous work found that a flat wavefront increased the intensity of filament induced N_2 fluorescence in air [46]. The results presented in this section suggest

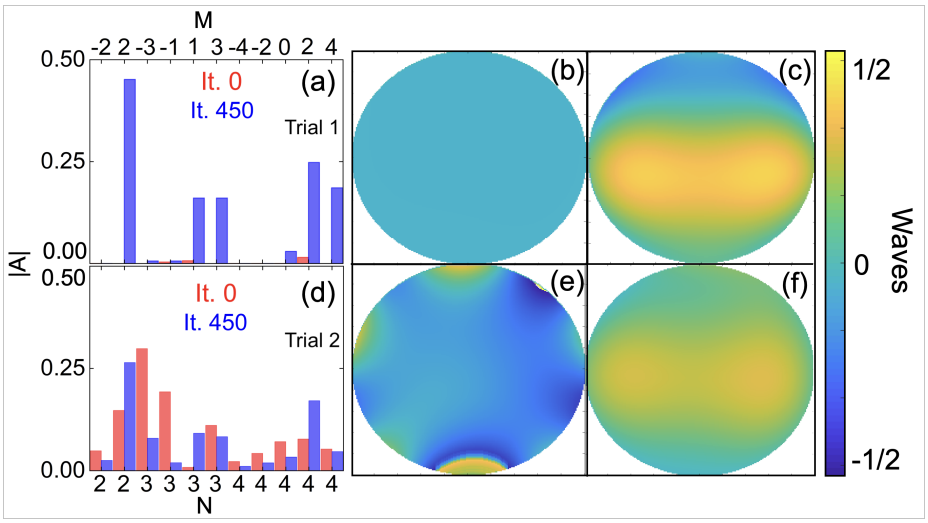

Figure 4.12: Zernike coefficients (a) and (d) extracted for the wavefront measurements at It. 0 and It. 450 for trial 1 and trial 2, respectively. The reconstructed wavefront profiles are shown for It. 0 in (b) and (e) and It. 450 for (c) and (f) for trial 1 and trial 2, respectively [60].

that the optimal wavefront for enhanced filament fluorescence is not necessarily the same as the wavefront that leads to improved filament ablation of a target some distance away from the laser source. Because the dominant aberrations are reproduced upon repeating the experiment, they must be of significance to filament formation and filament-target coupling, and are independent of peak power. Grantham *et al.* investigated the effects of applied aberrations on beam bifurcation, and found that primarily astigmatism and coma are responsible for "noncircular" geometry [74]; it is well-known that these aberrations lead to beam ellipticity. Fibich *et al.* discussed how astigmatism leads to a decrease in the number of filaments that form by confining the filaments to the major axis of the elliptical beam and suppressing filaments along the minor axis [56]. The degree of the wavefront perturbations induced by the algorithm can be further determined by using the voltage-to-stroke calibration of the DM:

$$\text{Stroke } (\mu\text{m}) = -1.3393 + 0.066929 \times V, \tag{4.4}$$

where V is voltage measured in volts. Since the initial surface is 70 V applied to

every actuator on the DM surface, the difference in stroke from this initial position can be calculated. The total shift applied to the wavefront ranges from −2.2 µm to 1.5 µm, or −2.75 waves to 1.88 waves.

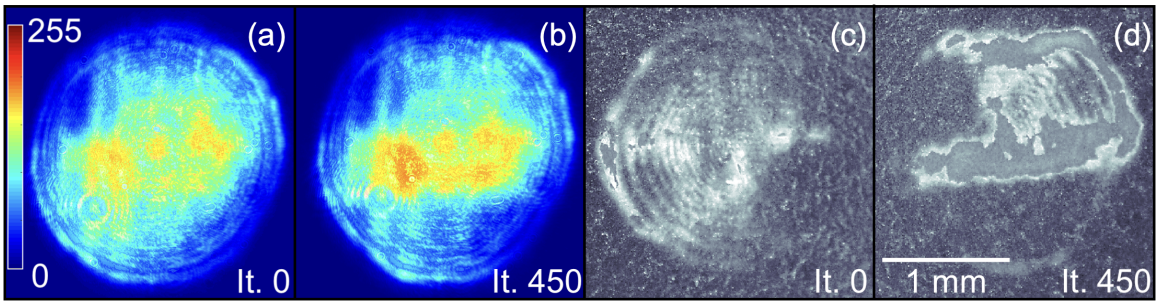

Figure 4.13: Imaged beam profile incident on the lens (a)–(b) and burn spot (c)–(d) measurements for: (a)/(c) It. 0 and (b)/(d) It. 450 for trial 2. The burn spots are measured for a single laser shot on burn paper 10 cm prior to geometric focus (target location) [60].

To measure the beam attributes resulting from the wavefront that produced the increased optical emission intensity, the beam profile and burn spots were recorded for It. 0 and It. 450 and are shown in Fig. 4.13. It can be seen that the beam profile becomes more elliptical as the wavefront is adjusted from It. 0 (Fig. 4.13(a)) to It. 450 (Fig. 4.13(b)), as would be expected when astigmatism and coma are introduced. Additionally, it is noted that the intensity in the center of the beam is higher at It. 450. Ablation profiles are recorded on laser alignment burn paper 10 cm prior to geometric focus in order to avoid ablation from the focused energy reservoir and better resolve the filament structure. Despite recording the burn spots prior to geometric focus, saturation in Fig. 4.13 (d) is observed as a result of the high intensity filaments. While this limitation of the measurement performed with burn paper is recognized, it is still interesting to compare Fig. 4.13 (c) and (d). The beam pattern at It. 0 in Fig. 4.13(c) shows dispersed hot spots in its profile. The burn spots in (d), produced with the beam at It. 450, indicate a more localized ablation profile which appears linear along the major axis in comparison to (c). The greater area of damage at It. 450 can be interpreted as more mass removed during ablation of the Cu sample.

This is supported by the spectra presented in Fig. 4.11, where the spectrum at It. 450 has higher intensity than the spectrum at It. 0, which is the evidence for more mass removed during ablation. Further work incorporating crater measurements could be performed to better quantify mass removal efficiency.

Daigle *et al.* reported enhanced optical emission signal of N_2 fluorescence and gaseous hydrocarbons from filamentation upon wavefront correction [46]. A wavefront absent of aberrations does not necessarily result in the greatest signal produced upon filament ablation of a solid target, as shown in the present work. In fact, it is found that introducing aberrations like coma and astigmatism lead to enhanced FIBS signal. For gaseous excitation with filamentation, it is desirable to use the laser energy to ionize the propagation medium; however, in our work the goal is to deliver the greatest amount of energy to a solid target some distance away from our laser source. For this reason, minimizing ionization and excitation in air is ideal, so that there is more laser energy available to produce a strong signal on the sample surface. It is possible that applying these aberrations reduces the ionization of air prior to the Cu target. This is achievable either by redistributing the laser energy so that the energy reservoir more efficiently feeds the filaments, rearranging the filament structure to confine ablation over a smaller area [56], by shifting the focus so that the filament forms at a different location along the propagation path [50], or a combination of all three methods.

Astigmatism and coma are known to lead to beam ellipticity, which is observed in Fig. 4.13(a) and (b). These profiles are recorded with the image plane being the entrance face of the focusing lens used for filamentation. This location for measuring the beam energy redistribution was chosen due to the challenge of measuring the the filament at the target surface, where the intensity is much higher. Astigmatism results in a separation between foci in the sagittal and tangential planes. Astigmatism may result in a shift in the axial position of the filament that produces ablation [50], which can affect the energy available for ablation at the target surface. Evidence of increased

ablation efficiency is presented in the burn spot measurements in Fig. 4.13(c) and (d), where the ablation is more confined and more damage is present in the case of ablation at It. 450. The degree of the perturbation to the wavefront is therefore significant enough to reorganize the multi-filamentation pattern, and has been demonstrated in previous work [53, 56].

Fibich *et al.* demonstrated that by inducing astigmatism, one can significantly reduce the number of filaments generated in the transverse profile of the beam [56]. Astigmatism was applied by rotating the focusing lens from 0° to 20° around the axis perpendicular to the beam propagation direction. The authors observed that filaments that formed along the minor (vertical) axis of the beam at small rotations disappeared at larger rotations. Furthermore, higher intensity filaments formed along the major axis in a predictable manner at larger rotations, and the authors found that sufficiently large astigmatism inhibits the formation of more than a single filament. Therefore, constraining multiple filaments to fewer intense filaments for ablation of a target may be the reason for observation of enhancement of spectral intensity in this work. While there is no evidence for significant multi-filament suppression according to the burn spots recorded in Fig. 4.13(c)–(d), the ablation profile is more confined, which leads to improved ablation efficiency at It. 450 as opposed to It. 0. These higher intensity filaments may couple to the target better than more dispersed, weak filaments, and result in greater ablation volume, increased plasma density, and signal intensity, which is observed in the spectra recorded in Fig. 4.10(c)–(d) and Fig. 4.11. It is important to note that the ablation efficiency is dependent on the target material, surface roughness, and surface shape. It may be possible that a different target can influence the wavefront needed for signal enhancement; however, further work is needed to explore this parameter space.

4.3 Summary

In summary, the optical emission spectra were examined in order to determine the filament plasma properties in the multiple filament regime. The spatio-temporal structure of the filament plasma was evaluated and the visible emission lifetime was determined to be ∼5 ns, which agrees with previous measurements performed on single filaments. Both the N_2 and N_2^+ emission bands peak at the same axial location prior to geometric focus and follow similar emission trends along the length of the plasma, suggesting similar relative spatial population distribution of the molecular nitrogen species. The occurrence of O I peak emission near or after geometric focus, however, implies that collisional (plasma) processes may have a more significant contribution to the dissociation and excitation of oxygen than radiative processes directly driven by the laser. Similar electronic temperatures of ∼5000–5200 K are estimated as well as uniform axial distributions despite multiple filamentation for both 400- and 800-nm pulses. This negligible change was attributed to increasing total peak emission resulting from the formation of several plasma cores, each with a similar temperature, reported for single filaments. Although more efficient multiphoton inner-shell ionization is observed for the 400-nm filament, the axial gradient for the N_2 emission measured at the beginning of the filament is greater than the N_2^+ emission for both wavelengths, demonstrating different ionization and excitation paths for these two processes. Electron density has a more significant change with axial position than temperature, and the maximum density appears near geometric focus. These results provide further insights into the characteristics of filament plasma in the multiple filament regime, which dictates the guided laser intensity relevant to applications such as remote sensing. A dedicated modeling study is needed, however, to better understand the fundamental processes leading to these observations.

Furthermore, it is demonstrated that the use of a GA to control the spatial phase of a high-power laser beam for FIBS can significantly increase the characteristic signal

intensity. This method can be applied without previously eliminating imperfections or aberrations from the optical system in attempt to suppress multiple filamentation, which has been an approach taken in the past. Two separate trials of the GA reach a similar magnitude of enhancement, and the aberrations applied to the beam to achieve signal enhancement are primarily coma and astigmatism. In agreement with previous work, the effects of elliptical localization of filaments were observed as a result of astigmatism. Shot-to-shot FIBS signal fluctuation is slightly reduced by wavefront optimization, but this effect is not distinctive enough to be a major benefit of this method. Along with increased signal intensity, evidence was presented for improved filament-target coupling by the appearance of continuum and ionic emission features in the spectrum for the optimized wavefront. Generation of high-intensity filaments through wavefront shaping plays an important role in extending the distance and detection limits of FIBS. The result of astigmatism and coma is verified through two trials of the GA at different pulse durations, and since the GA operates by a semi-random mutation process using the DM surfaces that produce the largest FOM, this enhancement is shown to be reproducible despite differences in peak power and initial wavefront. The results in this work can be applicable in-field as a starting point for signal optimization, where convergence time for the algorithm would be reduced significantly, and could be further improved with higher laser repetition rates or data acquisition speeds. While further work is needed to precisely define the mechanisms that lead to signal enhancement and test these results with producing filaments at larger distances, it can already be concluded that the use of adaptive optics in conjunction with a genetic algorithm using a spectral signal as feedback is a promising strategy for signal optimization in remote filament ablation applications.

CHAPTER 5

Remote Single-Shot Detection of Uranium via FIBS

Remote detection of uranium (U), its isotopes, and uranium-containing molecules has a potential to address various nuclear security needs in areas such as nonproliferation, safeguards, and treaty verification [48]. Traditional radiation detection methods, which rely on observing the products of radioactive decay, are limited by nuclear decay rates, yield, and range of the emitted radiation. Laser-based methods could overcome the drawbacks of radiation detection techniques and be helpful in scenarios where no shielding is presented to the laser beam. Optical emission, which can propagate over long distances through atmosphere following laser excitation of a sample, originates from de-excitation of atomic or molecular populations. Pulsed-laser based methods further establish a distinct time structure that accompanies ionic, atomic, and molecular signatures to facilitate rejection of continuous background such as ambient light. Both the qualitative and quantitative capabilities of one such optical technique – LIBS – have been demonstrated in detection of uranium, its isotopes, and uranium-containing compounds [11, 38, 39, 81, 86, 132]. LIBS and its remote counterpart FIBS were introduced in Chapter 2. In Chapter 4, filament propagation at high peak powers, where multi-filament formation occurs, was investigated. This regime is relevant for remote excitation of samples, where high peak powers are needed for extended

delivery of laser energy.

The work presented in this chapter demonstrates how filamentation can be used to remotely excite optical signatures of uranium, and in particular of uranium monoxide that can be used to achieve isotopic sensitivity [86]. The ability to make distant isotopic measurements of uranium is of paramount importance to nuclear nonproliferation applications. Furthermore, this chapter discusses the underlying physical and chemical processes that lead to improved signal-to-background ratio of the UO molecular spectral signature at 10 m compared to ablation and measurements made at 2 m and 5 m, despite lower energy reaching the target. This chapter includes edited portions from Refs. [62, 63].

5.1 Loose-focusing FIBS for rapid, remote detection of uranium

Recently, ns-LIBS has been explored as a method for detecting uranium, and standoff distances of up to 30 m have been reached [38]. However, diffraction limits the distance to which ns pulses can be delivered with sufficient intensity to perform laser ablation or sample excitation, and beam propagation is further subject to atmospheric turbulence [118]. FIBS and femtosecond filament-laser ablation molecular isotopic spectrometry (F^2-LAMIS) [97] have been used to detect low-Z targets, which exhibit well-isolated features in their emission spectra; FIBS in particular has been demonstrated at distances up to 90 m [127, 155]. In contrast, high-Z elements, such as U, yield congested spectra with many interfering spectral lines arising from ionic and atomic transitions [144] that are difficult to distinguish from continuum and background. Additionally, recent work shows that unresolved spectral features from uranium oxides further congest the uranium emission spectrum. U_xO_y compounds readily form in laser-produced plasmas (LPPs) even at small ambient oxygen con-

centrations [170], and molecular-oxide emission is an integral part of the uranium spectrum for LIBS in air. For example, recent studies measured the isotopic shift between ^{235}U and ^{238}U in the UO 593.55 nm band to be approximately 180 pm [87], whereas the isotopic shift for ionic or atomic lines is less than 50 pm [81], suggesting that LIBS may be viable for uranium enrichment measurements in air [132]. In the work presented in this chapter, the focus was on a spectral range that contains both atomic and molecular UO signatures (591 nm–601 nm). It is demonstrated that both uranium atomic and molecular emission can be simultaneously excited using FIBS at a distance of 10 m with 10-mJ pulses, and that uranium can be detected using a single laser shot over this distance with a modest light collection system.

5.1.1 Experiment

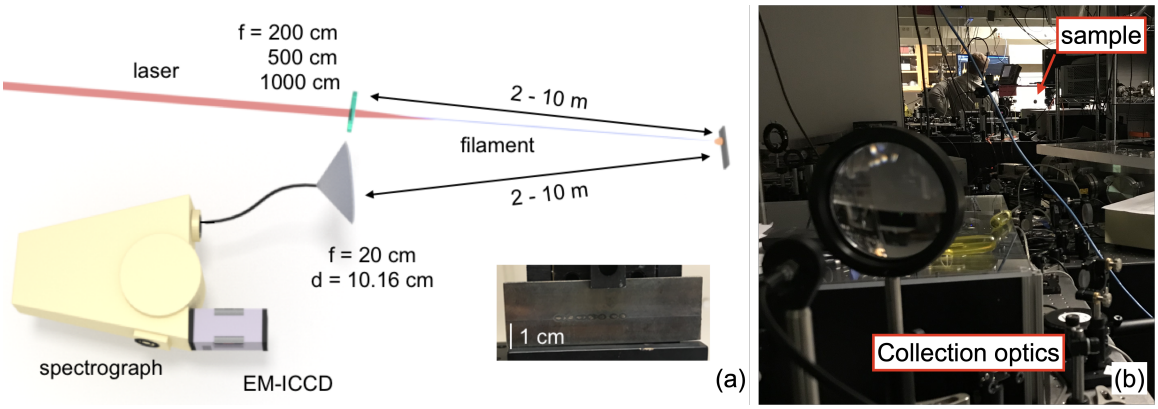

Figure 5.1: (a) Schematic of the experimental setup for the remote measurements (not to scale). The inset shows the photograph of the depleted U target used in the experiment [62]. (b) Collection optics and sample location in the Lambda-cubed laser facility on the University of Michigan campus [63].

A schematic of the experiment is shown in Fig. 5.1(a). A Ti:sapphire chirped-pulse amplification laser system was used, with a central wavelength of 790 nm and pulse duration of ∼50 fs. Pulses had the energy of 10 mJ, repetition rate of 80 Hz (reduced from 480 Hz), and a Gaussian beam diameter of 22 mm. The beam was loosely focused using 2-m, 5-m, and 10-m focal length, 5.08-cm diameter lenses ($f/90$,

$f/225$, and $f/450$, respectively) to form filaments in air. Filaments ablated a depleted uranium (DU) metal target placed at the geometric focus of each lens. The DU target was placed into a fume hood and separated from the laboratory by a barrier with an 8-cm aperture to permit the filament to reach the target and allow measurement of the plasma emission without inhibiting the solid angle of the collection system, as shown in Fig. 5.1(b). The sample was mounted on a motorized translation stage for continuous movement during measurements to ensure a fresh sample spot. The remote collection system was comprised of a 20-cm focal length, 10.16-cm diameter lens ($f/2$) focused onto a 400-µm diameter optical fiber, which was coupled to a 0.55-m Czerny-Turner spectrometer (Horiba Jobin Yvon iHR550) and an electron multiplying-intensified charged coupled device (EM-ICCD, Princeton Instruments PI-Max 4). A grating with 1800 l/mm (resolving power ∼16000) was used. Time-resolved reference spectra were recorded at a fixed distance of 35 cm from the target using a variable fiber-coupled collimator (Andor CC52).

5.1.2 Results & Discussion

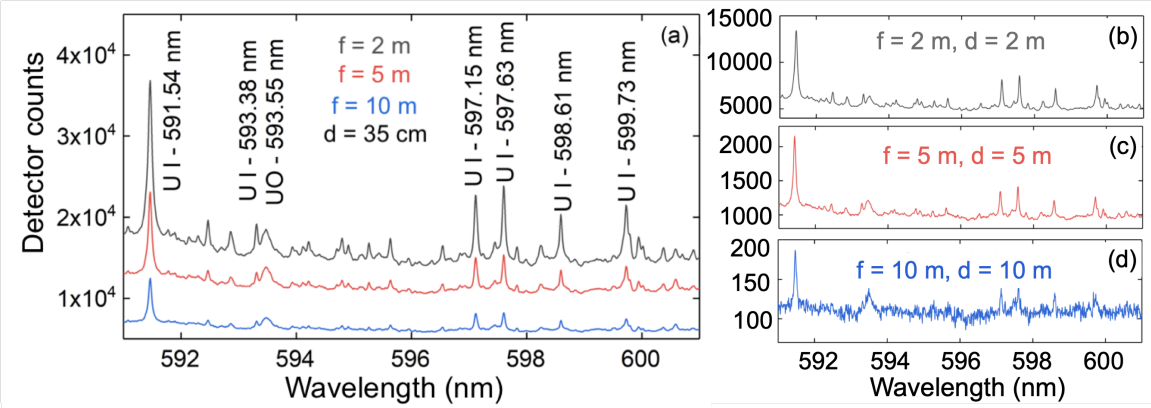

Figure 5.2: (a) Sample uranium emission spectra measured at 35 cm while under 2 m, 5 m, and 10 m focusing conditions; (b–d) emission spectra recorded at the same distances as the focusing lens (where f is the focal length of the lens and d is the distance of the collection system from the target). Each spectrum was averaged over 1000 laser shots, with a gate delay of 50 ns after the laser pulse with a gate width of 2 µs [62].

Figure 5.2(a) shows representative emission spectra measured at a fixed distance of 35 cm while varying the filament focusing conditions. These spectra reflect the differences that arise in the formation and evolution of the plasma for different filament focusing conditions and propagation distances employed in the experiment, with the same laser pulse energy of 10 mJ. Notable spectral features include the atomic uranium (U I) resonance line at 591.54 nm, among other less intense U I lines, and the broader feature from UO centered at 593.55 nm. Figure 5.2(b–d) shows representative spectra averaged over 1000 laser shots recorded at the same distance from the target as the focusing lens, demonstrating the capability to generate and collect a representative signal for uranium using FIBS despite decreased collection efficiency as a result of $1/R^2$ scaling, where R is the distance between the sample and the collection system. Both U I and UO are observed simultaneously in each focusing scheme. Femtosecond ablation typically yields colder plasmas in which U oxides tend to form more readily [58], in contrast to hotter nanosecond-LPPs, in which oxides form at late times or near the plasma periphery [57]. The time dependence of atomic and molecular emission and the background is further investigated.

The time evolution of U I and UO emissions measured 35 cm from the target with varying filament focusing conditions can be seen in Fig. 5.3. In order to quantify the signal, spectral features of U I and UO species are isolated from background and nearby or overlapping features. First, the measured background was fit to a second-order polynomial and subtracted from the spectrum. The area under this polynomial was used as the background signal area. Next, to determine the limits of integration for signal counts, the background-subtracted spectrum was fit to isolate the U I 591.54-nm line and UO 593.55-nm band. Example fits and limits of integration are shown in Fig. 5.3(d) and (e). The pixel at which the U I 593.38 nm line reaches $1/e^2$ of its maximum intensity was chosen as the starting point for integration of the UO signal; the end of the integration was set to the point where the signal reaches

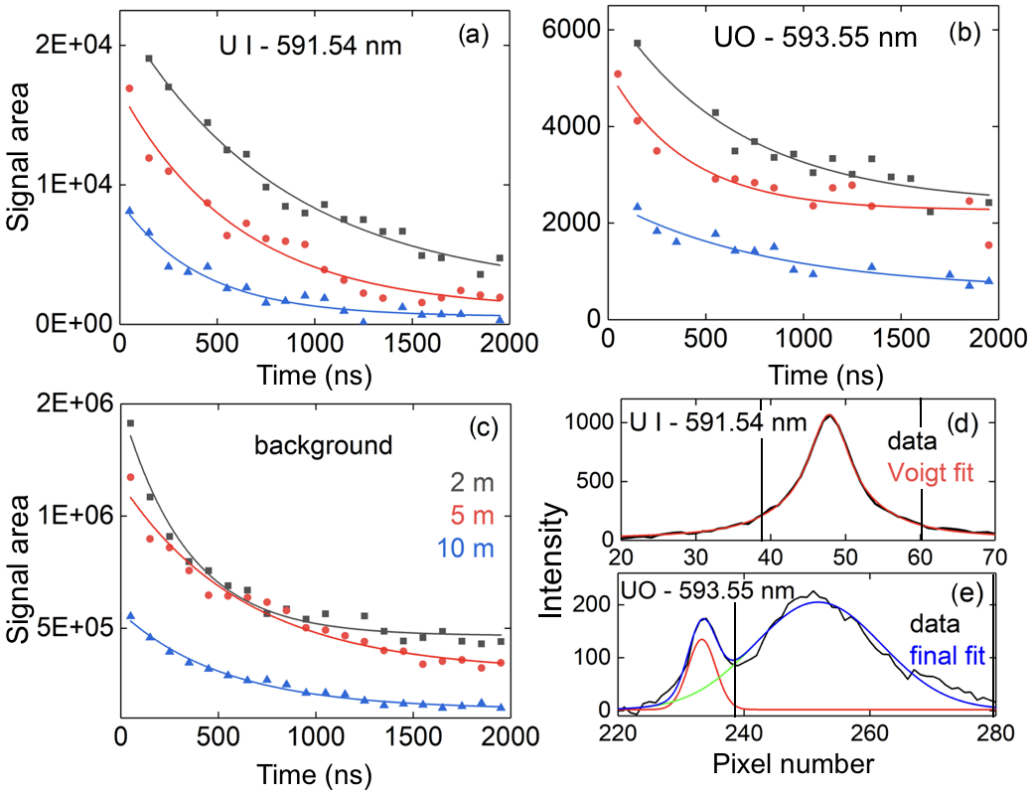

Figure 5.3: Time-dependent emission intensity for (a) U I 591.54 nm; (b) UO 593.55 nm; and (c) background. The background is determined as the area under a polynomial curve fit to the spectrum. Integration limits for the signal intensity were determined by fitting the emission profiles of (d) U I 591.54 nm and (e) U I 593.38 nm and UO 593.55 nm features. Atomic lines were fit with a Voigt profile, while the UO molecular band was fit with a Gaussian profile (green line – UO fit, red line – U I 593.38 nm fit). The initial gate delay was 50 ns. Each spectrum was measured with a 100 ns gate width, in 100 ns time steps up to 1950 ns [62].

the baseline. The integration limits for the U I 591.54 nm line are at $1/e^2$ of the maximum intensity for the fitted line profile.

The exponential decay rates vary considerably among the three focusing conditions. The decay constants for U I are 820, 614, and 418 ns for 2-, 5-, and 10-m ablation distances, respectively. A more intense signal was observed when focusing the laser pulse closer to the target, which is attributed to greater energy available for ablation because of the efficient coupling of the energy reservoir around the filaments with the target in addition to filaments [81]. The background decreased exponentially

with time, similar to the signal, which implies that it originates from the LPP as opposed to other sources (*e.g.*, detector noise), and persists much longer than plasma continuum that is known to occur only at early times after laser ablation and is almost nonexistent for filament ablation [84]. This observation is consistent with previously reported studies [85, 170], which suggest that background may be comprised in part from uranium oxide emission and is correlated to signal in any spectral region of consideration. Nonetheless, the plasma lifetime of ~2000 ns in all cases was selected as the gate width for the following analysis.

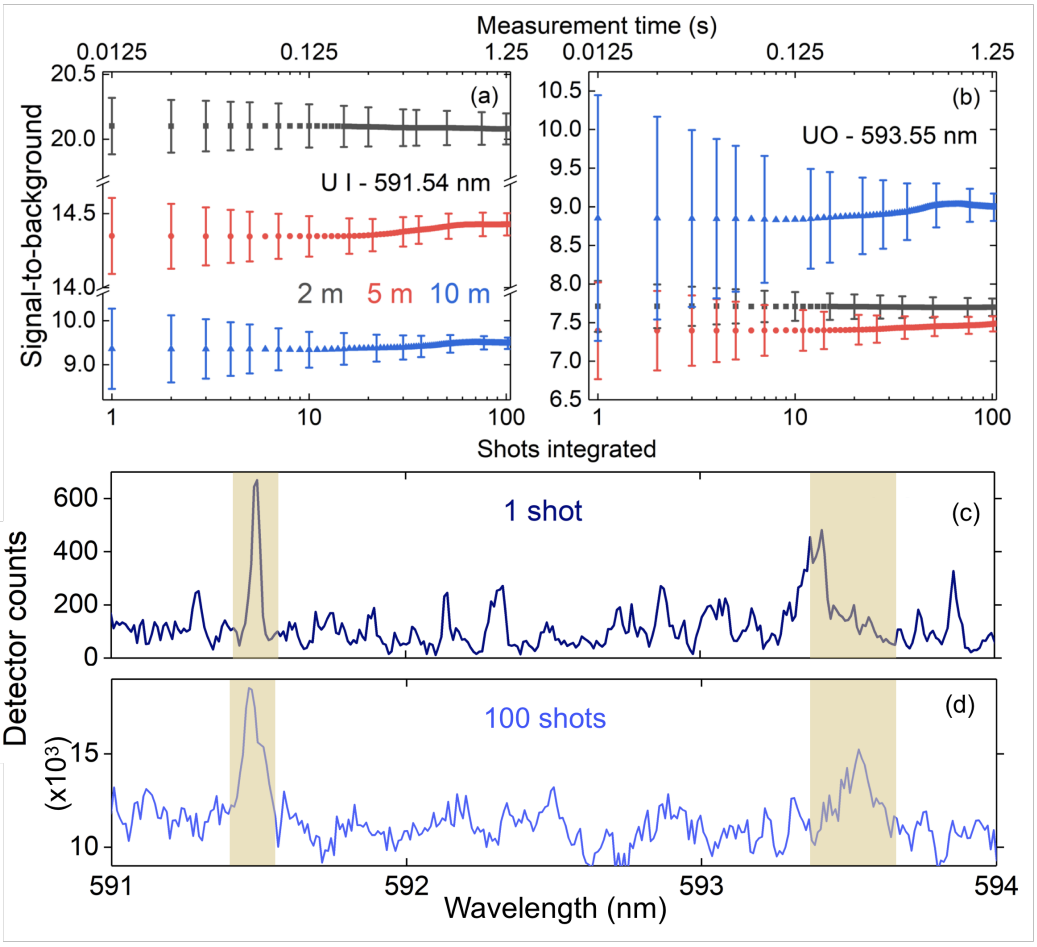

Figure 5.4: Evolution of the signal-to-background ratio with the number of laser shots for (a) atomic U I and (b) molecular UO for the remote collection and ablation scenarios for 2 m, 5 m, and 10 m. Signal development with shots integrated, single shot (c) and 100 shots (d) for the 10 m ablation-collection scenario. The shaded regions show the U I – 591.54 nm and UO – 593.55 nm features of interest in (a) and (b), respectively [62].

One of the most attractive features of FIBS is the prospect for detecting uranium much more rapidly than using traditional radiation detection, the ultimate case being remote detection using a single laser shot. To assess this possibility, first the SBR of U I and UO features are compared in Fig. 5.4. The background may be comprised in part of unresolved emission features from uranium oxides, and hence may be correlated to the U I and UO signals. However, the following analysis mimics a practical scenario in which quantification of how well the U I and UO spectral features can be distinguished from the measured background is determined, in which the background may include unknown unresolved oxide emissions. The SBR was nearly constant for each case when increasing the number of shots; as expected, the uncertainty in the SBR decreased with shot number. The uncertainty is calculated as

$$(\sigma_{\mathrm{SBR}}/\mathrm{SBR})^2 = (\sigma_{\mathrm{S}}/\mathrm{S})^2 + (\sigma_{\mathrm{BG}}/\mathrm{BG})^2, \tag{5.1}$$

where σ_{SBR} is the uncertainty in SBR, S and BG are the average signal intensity and background level, respectively, and σ is the standard deviation in each set of single or averaged spectra for the respective intensity of a feature. A relative uncertainty of $\sim$5% was reached after integrating 25 shots for the UO feature at 10 m, and 100 shots yield $\lesssim$2% relative uncertainty. The measurement times needed to reach these uncertainties at the experimental 80-Hz repetition rate are $\sim$0.35 s and $\sim$1.25 s, respectively. The SBR for U I decreased with increasing ablation-collection distance, as a result of lower laser energy reaching the target under farther ablation schemes, along with the increased collection distance. On the other hand, the SBR for UO at 10 m was greater than both 2- and 5-m cases. Also, the ratio of the intensity of molecular emission to atomic emission increased with ablation distance (0.37 for 2 m and 0.95 for 10 m). These results imply that lower intensity of the filament from farther ablation schemes under the present experimental conditions may foster the production

and/or favorable excitation of the molecular species. Different focusing conditions are expected to affect the uranium plasma chemistry, where longer filaments are known to lose more energy along the path due to ionization of air. However, a dedicated analysis on the filament interaction with the target is necessary to determine the mechanisms that lead to uranium-oxide formation in the plasma. Nevertheless, the improved SBR of UO at 10-m suggests that the UO band may be a suitable feature for detection of uranium in air using FIBS.

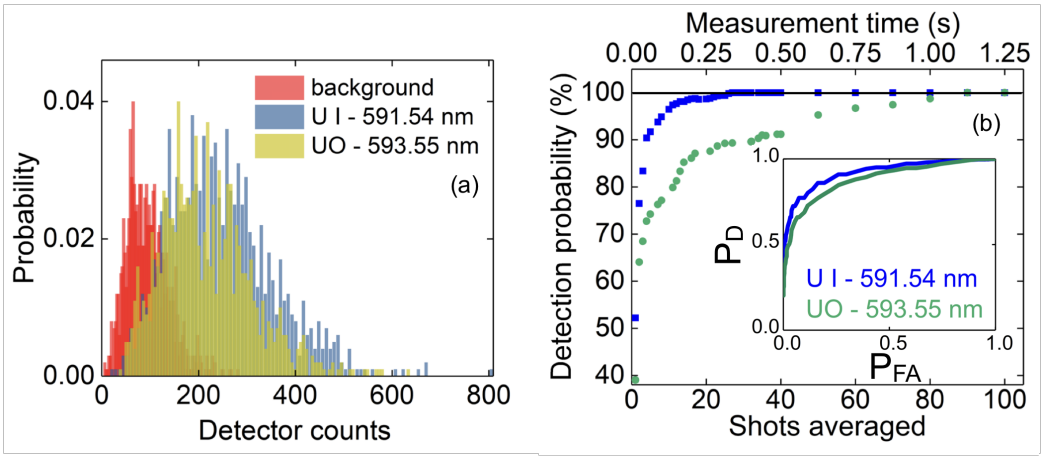

Figure 5.5: Single-shot probability distributions for signal and background compared to background counts alone for (a) 10-m ablation–10-m collection measurement. Both U I 591.54 nm and UO 593.55 nm signal features were considered. (b) Detection probability with laser shots averaged and measurement time with a set 1% false alarm probability. The inset shows the ROC curve for U I and UO signal features [62].

Next, the feasibility of single-shot detection of uranium using FIBS at a distance of 10 m is explored. Histograms were created for the signal counts (not background-subtracted) and compared to histograms of the background. Figure 5.5(a) shows histograms for both U I and UO emissions measured at 10 m for the 10-m ablation case. The probability of being above a chosen critical limit L_C was calculated and ROC curves were constructed for both signals, shown as the inset in Fig. 5.5(b). The

true detection (P_D) and false alarm (P_{FA}) probabilities are defined as follows:

$$P_D = \int_{L_C}^{\infty} P(N_D) dN_D, \tag{5.2}$$

and

$$P_{FA} = \int_{L_C}^{\infty} P(N_{BG}) dN_{BG}, \tag{5.3}$$

where N_D is the total signal+background count distribution, and N_{BG} is the distribution for background counts alone.

The ROC curve was constructed from 50 evenly-spaced L_C values from the minimum background to the maximum background. The ROC curve displays the single-shot detection characteristic for individual signals. For example, the true detection probability of a single-shot measurement is 52.2% and 39.0% for U I and UO signals, respectively, for a chosen false alarm probability of 1%. High-repetition-rate lasers and measurement systems would allow for more rapid detection. Figure 5.5(b) shows the detection probability for a fixed 1% false alarm probability determined by averaging a series of shots. A ∼100% detection probability is reached in just ∼0.3 seconds (24 shots) with our 80-Hz system for the atomic signal, and in ∼1.1 seconds (90 shots) for the molecular signal.

Signal and background variability ultimately limits the single-shot measurement. Background is contributed in part by U_xO_y for uranium-containing targets. However, for practical experiments, the limiting case also consists of ambient light leaking into the detector (room light). The contributions of the detector dark current and room lights were isolated; the mean background (no plasma) was 575 counts, and the variation (σ) was 1.2 counts. The background measured with the plasma present for 10-m ablation-collection distance approached this limit with a mean of 708 counts and σ of 41.5 counts. Note that the dark current and room light contribution were

subtracted from the data in Fig. 5.5(a). The observed variability (41.5 counts) in the data was greater than that predicted by the Poisson model (26.6 counts), providing evidence for real overdispersion. Experimental sources of overdispersion include laser energy and profile fluctuations, air turbulence, and variations in the target surface and matrix.

Additional sources of variability in the experiment can arise from the sporadic nature of multiple filaments, modulation instability of the laser wavefront, and air turbulence [201]. Various phenomena dictate intensity at the target, including oscillatory focusing and defocusing and pulse self-compression [14]. It was also observed in previous work by comparing tight-focus ($f/20$, no filament) fs-ablation, loose-focus ($f/400$, in which filamentation occurred) ablation, and free-propagating (no focusing optic) filament ablation with a brass target that there is a significant drop in initial LPP temperature for changing from one to another focusing condition, respectively. These results suggest that there is an additional, unknown contribution of the energy reservoir to ablation with "loose-focusing" [84] that may also contribute to variability.

5.2 Summary

Filament-induced breakdown spectroscopy (FIBS) is an attractive remote detection approach that is potentially applicable to practical nuclear material detection applications. Simultaneous detection of atomic uranium and uranium monoxide features was demonstrated in a single laser shot with detection probabilities of 52.2% and 39.0%, respectively, and with a 1% false-alarm probability. It was shown that a nearly 100% detection probability can be reached with 1% false alarm probability in $\lesssim$1 second when using an 80-Hz laser and data acquisition system. Atomic uranium and UO signal features are identifiable in the remote measurement with comparable SBRs, suggesting that, despite being broader than the U I emission line, the UO band

is also suitable for remote detection of uranium by FIBS. The magnitude of the SBR for both the U I and UO signatures show promise for detection over greater distances than the 10 m study employed here, in particular with an improved collection system.

In conclusion, it is demonstrated that single-shot detection of U I and UO features using FIBS is feasible under chosen definitions of true detection and false alarm probabilities at a distance of 10 m. Rapid ($\lesssim$1 second) measurements at 80 Hz enable $\sim$100% detection probability with a 1% false alarm rate, and this measurement time can be reduced with a system that can operates at higher repetition rate. Furthermore, the UO 593.55 nm band was more distinguishable at 10 m in these experiments, with an SBR of $\sim$9.0, than in the 2- and 5-m cases, with SBRs of $\sim$7.5–8.0. The increased SBR fro UO at 10 m ablation and collection is an anomalous result, as it is expected that at greater collection distances the reduced signal intensity would reduce SBR. However, because of the filament ablation dynamics which occur under remote schemes, the filament produced plasma conditions at 10 m appear to foster the formation of molecular species, resulting in a greater detectability than with closer ablation schemes. UO and U I SBRs are comparable at 10 m. Therefore, UO is also suitable as a signature for remote detection of uranium in air, in addition to U atomic transitions. Further work could be done incorporating the GA introduced in Sec. 4.2 to manipulate the multi-filament distribution over the 10 m ablation distance such that UO molecular emission is favored over U atomic emission. The results in this work are promising for the future of laser-based remote sensing in the nuclear nonproliferation space.

CHAPTER 6

Femtosecond and Filament-LIF of Biota for Stress Monitoring

Chapters 4 and 5 explored the use of filaments to excite optical signatures directly from the material of interest, generally through LA. However, when there is contamination in the environment, it may be difficult to directly excite observable optical emission, especially in low concentrations. There has been recent interest in using plants as biosensors for contamination in the environment due to their extreme sensitivity to growth conditions. In this chapter, the capability of filaments produced by ultrashort laser pulses to excite optical signatures in plants and identify stress responses is investigated.

The response of plants to stress and toxicity has been the subject of numerous studies. Plant health monitoring is relevant to many applications including agriculture [162], pollution monitoring [8], biosensor development [6, 107, 186], biofuels [114], and remediation efforts for nuclear accidents [51, 110]. In particular, uranium exposure in the environment is of recent interest for nuclear nonproliferation purposes. The majority of prior studies focused on the effect of natural stresses such as drought, or the exposure to heavy metals associated with industrial pollution, such as lead, cadmium, and arsenic [10, 101, 131, 205]. In addition to area monitoring in the case of accidental nuclear releases, it has also been suggested that such biosensors may enable

large-area surveys for detecting nuclear proliferation activities. Future progress in this field critically depends on the understanding of the specificity of plant's response to uranium contamination and the optimal method to detect this response, especially over long distances [19, 89, 159, 183–185]. One highly relevant proliferation scenario that includes a pathway for uranium contamination is clandestine enrichment of uranium [109]. For example, the centrifuge process employs UF_6 gas to alter the isotopic composition of naturally occurring uranium (consisting predominantly of U-238 and U-235) to greater concentrations of U-235. Small quantities of UF_6 gas can escape from these facilities and interact with water in the atmosphere to form UO_2F_2 [109], which can deposit in surrounding soils and water systems and be absorbed by or adsorbed onto plants.

Prior studies have explored the form of uranium that is most bioavailable across a broad range of biota, such as algae [65], *Arabidopsis thaliana* [19, 52], *Brassica juncea* [33], and many others. In all cases it has been found that uranium in the form of the uranyl ion (UO_2^{2+}) is the most mobile in soil and roots and is the dominant uranium species at slightly acidic pH's, around 4.5–6.5. It has also been found that this ion chelates with other essential nutrients commonly found in plant soil, such as phosphates and carbonates [89, 185]. In general, uranium is known to have long-term toxic effects in plants, evidenced by the formation of radical oxygen species (ROS) such as H_2O_2, and that the proteins glutathione and ascorbate play an essential role in mitigating the effects of ROS damage to photo-sites within the photosynthetic chain [7, 183]. The efficacy with which various algae species can remove uranium from water systems was investigated [65], along with the effect of uranium exposure on the photosynthetic efficiency and function of algae [66, 68, 92]. It has been reported that microalgae can be highly resistant and adaptable to harsh growth conditions, such as extreme pollution from uranium mining [68]. While the uptake of and plant response to uranium has been investigated, signatures of uranium exposure that could be used

for remote and rapid in-field detection have not been explored.

Plant health can be assessed by protein sequencing [188], genomics [21], and by measuring certain optical properties [28, 137, 138, 182]. Protein sequencing and genomics offer in-depth chemical and biological information into the cellular-level mechanisms of changes in response to different stresses. However, they are time consuming and require sample preparation, processing, and intensive data analysis which make them unsuitable for remote, wide-area surveys. In contrast, optical properties of plants are much more promising for real-time, in-field monitoring of plant health. Plants' optical properties and techniques that are currently implemented in-field were introduced in Chapter 3. The three main methods that have been used to interrogate plants in-field are pulse amplitude moldulated-fluorometry (PAM-F), hyperspectral imaging through reflectance spectroscopy, and solar-induced fluorescence (SIF). Only the latter two methods are suitable for remote detection. The main drawback of these techniques is that solar radiation contributes significantly to the background, and weak signal is observed in areas of low plant density.

Fs-LIF is a promising method for standoff optical characterization of plant health. Two main benefits of LIF that make it attractive for remote monitoring of plants' stresses are (1) the ability to efficiently reject slow-varying solar background from rapidly-varying luminescence signal, which results from excitation using a pulsed source and the use of a fast-gated detector; and (2) the ability to precisely direct the laser excitation source to a target, narrowing the interrogation region to where plant material is abundant, which can improve the signal-to-noise ratio. While this method is not commonly used to study plant response to stress, as reported in the literature, some studies have shown that fs-LIF has been successful in identifying changes in the ChlF lifetime in response to drought stress in moss [167, 195, 196]. Results from previous work indicate that stress in the Chl *a* sites in the photosynthetic chain which contribute to water uptake and processing affect the observed ChlF lifetimes. Further

work is still needed to identify the information one can retrieve from fs-LIF of plants. Laser-based excitation of chlorophyll in plants has been explored with ns and fs lasers, but filament excitation of plants through LIF has yet to be reported.

In this chapter, time-resolved optical properties of hydroponically grown *Arabidopsis thaliana* under three different growth conditions are explored: control, drought, and uranium-exposed. It is found that *A. thaliana* is more resistant to uranium exposure than drought stress, evidenced by perishing of drought stressed plants after 72 hrs, whereas the plants exposed to uranium are still visibly healthy up to 96 hrs. With drought stress, a decrease in the lifetime of the peak at 675 nm corresponding to PSII activity with respect to the lifetime of the PSI peak is observed. A similar response was also reported in previous work investigating moss resistance to drought [167, 195, 196]. For uranium stress, a "shock" response within the first 24 hrs of exposure is observed, where the ratio of $\tau_{675\ \mathrm{nm}}/\tau_{730\ \mathrm{nm}}$ decreases drastically. However, after the initial 24 hrs, the fluorescence lifetime ratio increased and remained relatively consistent over the duration of the experiment. There further appeared to be a strong correlation between lifetime ratios and [Chl]:[Car] ratios for the uranium-exposed plant. It was determined that there is a recovery after the initial shock response, potentially as a result of phytostabilization of uranium in the hydroponic solution after initial uptake of uranium. Furthermore, the feasibility of ultrafast laser filamentation to non-destructively excite fluorescence in the green alga *Chlamydomonas reinhardtii* is investigated for remote, rapid detection of uranium exposure. Ultimately, it is found that initial uranium exposure does induce stress through observed ROS formation evidenced through the steady-state absorption spectra, and that the fluorescence lifetime for both the 675-nm and 720-nm features increases. A parameter is calculated from the temporal profile of the fluorescence decay, and with distance-dependent uncertainty propagation, it is found that excitation and detection of uranium exposure is possible over approximately 100 m in a 1-s measurement time

with modern laser and data acquisition systems. This chapter contains edited content from Ref. [61].

6.1 Femtosecond-LIF of *Arabidopsis thaliana*

In this section, the change in optical properties of *Arabidopsis thaliana* in response to three different growth conditions is explored to determine the feasibility of fs-LIF as a method to distinguish the presence of nuclear proliferation-related stressors from natural stressors in the environment. Further, steady-state absorption spectroscopy is performed on extracted cells to better understand how the fluorescence properties, such as excited-state lifetime, are influenced by pigment concentration (Chl *a*, Chl *b*, and Car) in response to uranium and drought stress. A positive correlation between [Chl *a*]:[Chl *b*] and $\tau_{675\ \mathrm{nm}}/\tau_{720\ \mathrm{nm}}$ is identified for drought stress, whereas a stronger relationship between [Chl]:[Car] is observed with $\tau_{675\ \mathrm{nm}}/\tau_{720\ \mathrm{nm}}$ for uranium stress. A notable decrease in $\tau_{675\ \mathrm{nm}}/\tau_{720\ \mathrm{nm}}$ after 24 hrs is observed for the uranium exposed case, and may be a "shock" response of the plant. A potential recovery is observed which is proposed to be a result of phytostabilization after the initial exposure to uranium. It is found that fs-LIF of chlorophyll may be a promising method for stress detection in plants.

6.1.1 Experiment

6.1.1.1 Hydroponic growth of *Arabidopsis thaliana*

A. thaliana seeds were obtained from the Ohio State University Arabidopsis Biological Resource Center (CS72318). Rockwool was the growth medium, and the nutrient solution components can be seen in Table 6.1. The seeds were planted 1 mm below the surface of the Rockwool and kept in the dark until the sprouts were ∼1-5 mm above the surface of the Rockwool. Once sprouted, the seedlings were placed 125 mm

below a grow light (390 nm–720 nm) with a photon flux density of 120 µ mol/s m^2 (25 W/m^2) and a cycle of 8 h on/16 h off. Once the roots grew to the bottom of the Rockwool, each plant was transferred to a netted pot and placed in separate containers containing nutrient solution. *A. thaliana* was grown to 50-day maturity before stress exposure. It is important to note that a fraction of the plants had bolted, *i.e.*, had grown stems and began to flower at the time of the stress exposure.

Table 6.1: Nutrient media concentrations in one gallon of water used for hydroponic growth.

Nutrient	Mass (g) per gallon
KNO_3	0.7
$(NH_4)_3PO_4$	0.1
K_3PO_4	0.35
$MgSO_4$	1.05
H_3BO_3	0.04
Cu-EDTA	0.06
KCl	0.33
Fe-DTPA	0.07
Mn-EDTA	0.25
Zn-EDTA	0.06
Na_2MoO_4	0.004
$Ca(NO_3)_2$	1.0

6.1.1.2 Stress Exposure

Previous work demonstrated that uranium uptake increases when uranium is in the form of the uranyl ion ($UO_2{}^{2+}$), in solutions with lower pH in the range 4.5–6.5, and with minimal concentrations of aqueous phosphorous or calcium [7, 185]. In order to optimize conditions for uranium uptake, a simplified Hoagland nutrient solution was prepared following the procedure outlined by Hayek *et al.* [89]. Briefly, the solution consisted of $MgSO_4$, KCl, NH_4NO_3, and $NaHCO_3$. This control solution was used to confirm that any response from the uranium exposure does not solely originate from Ca deficiency. In summary, *A. thaliana* was exposed to three different growth conditions: control without Ca, drought (*i.e.*, all water removed from the

system), and uranium (500 µM) stress. The uranium solution was prepared by the adding $UO_2(NO_3)_2$ to the simplified Hoagland solution. Samples were prepared every 24 hours over a period of 96 hours.

6.1.1.3 Cell extraction

The thylakoid membranes from the leaves of *A. thaliana* were extracted following Method II in Ref. [35]. Briefly, three buffer solutions were prepared, and the pH of each was controlled with HEPES KOH buffer (7.8): grinding buffer, shock buffer, and a storage buffer. Approximately 2 g of leaves were clipped from each plant every 24 hrs, at the same time each day, and stored in a dark, 4°C refrigerator for 30 min prior to the extraction process. The samples were collected from the top of the rosette of leaves, characteristic to *A. thaliana*, to avoid pigment fluctuations that occur from variations in light exposure (ex. shading from other leaves). Once refrigerated, leaves were ground in the grinding buffer 1 mL:1 g (vol/w) (ex. 2 g of leaves are ground in 2 mL of grinding buffer) using a mortar and pestle until completely disintegrated. The remaining mixture was then filtered through two layers of Miracloth (pore size 20 µ m). The solution was then transferred to a tube that was centrifuged for 5 min at 2850 rpm. A pellet formed at the bottom of the tube containing the intact thylakoid membranes. The supernatant was disposed of, and the pellet was then suspended in the grinding buffer for a second time. The samples were run through the centrifuge again at 2850 rpm. Next, the pellet was resuspended in the shock buffer and centrifuged at 4000 rpm for 5 min. After removing the supernatant, the resulting pellet was suspended in the storage buffer and passed through one final cycle of the centrifuge at 4000 rpm for 5 min. This supernatant was disposed of, and the final pellet was then resuspended in the storage buffer and stored in the refrigerator until it was used in experiments. The centrifuge was kept at a temperature of 4 °C during runs. Measurements were performed within five days

of sample preparation.

6.1.1.4 Optical Spectroscopy: fs-LIF and Steady-State Absorption

The experimental setup for fs-LIF is presented in the schematic in Fig. 6.1. A Ti:sapphire CPA laser system was used to conduct all fs-LIF measurements. The CPA amplifier was seeded with an 80-MHz pulse train of ∼12 fs pulses from a Kerr-lens-modelocked Ti:sapphire oscillator. Compressed output pulses with 1-kHz repetition rate, 130-fs pulse duration (11-nm spectral FWHM bandwidth), a 3.5-mm ($1/e^2$) beam diameter, and 780-nm central wavelength were used for SHG of the fluorescence pump signal. SHG results in a central laser wavelength of 390 nm using a 200-µm-thick Type I BBO crystal. The pulse energy after SHG is 1 µJ, and a dichroic mirror was used to reject any residual 780-nm light. The optimal pulse energy was determined experimentally to prevent optical bleaching of the suspended solution. The fluorescence detection system consisted of a fiber-coupled collimator oriented perpendicular to the beam propagation direction. The signal was coupled into the entrance slit of a Czerny-Turner spectrograph (Andor Shamrock SR303i) used in combination with an intensified charge-coupled device (ICCD, Andor iStar 334T). A 150-l/mm grating blazed at 800 nm was used. Camera triggering was initiated via a 20-Hz TTL signal provided by a digital delay generator (Stanford Research Systems DG535) synchronized to an 8:1-divided RF clock signal from the laser oscillator. The steady-state absorption spectra were recorded with a Varian Cary 50 UV-VIS-NIR spectrophotometer. Pigment concentrations of Chl *a*, Chl *b*, and total Car were calculated following the equations outlined by Porra *et al.* [151].

6.1.2 Results & Discussion

Figure 6.2(a) shows an example absorption spectrum of thylakoid membranes extracted from the *A. thaliana* plants. There is an elevated baseline originating from

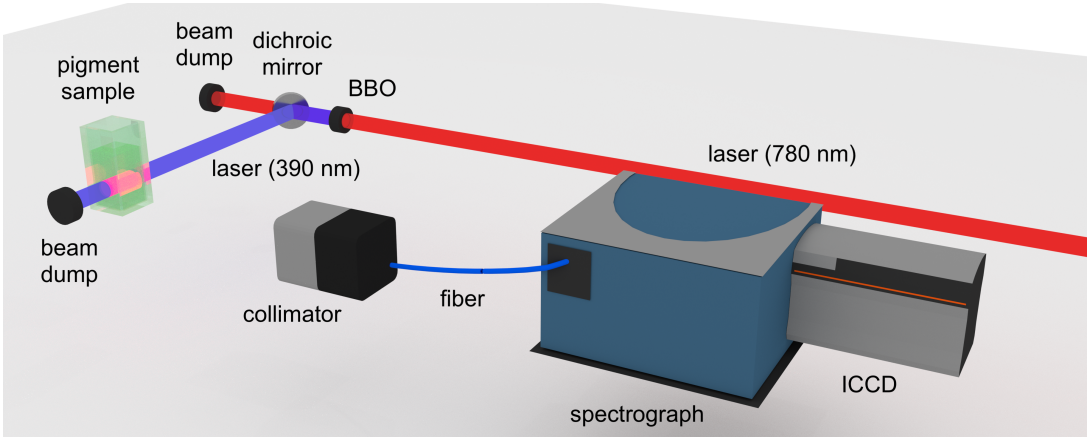

Figure 6.1: Experimental schematic for fs-LIF of extracted plant cells. [61].

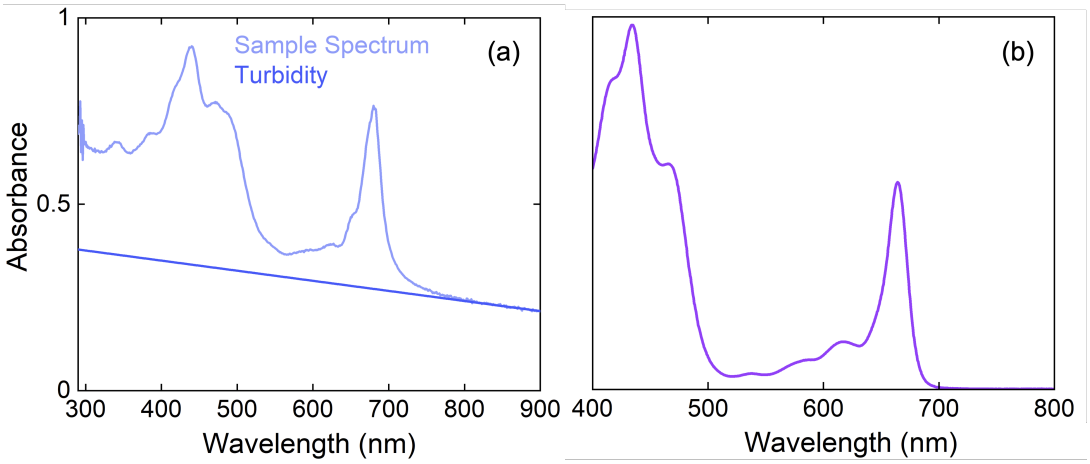

Figure 6.2: (a) An example absorption spectrum of the extracted thylakoid membranes from *A. thaliana* along with an example turbidity fit [61]; (b) Pigments from *A. thaliana* leaves extracted in 95% ethanol.

the turbid cell membranes, which can be fitted with a line using calibration points that generally do not contain any relevant absorbing species. The 800–900 nm region is fit with a linear function and extrapolated to the lower wavelengths. An example linear fit is also shown in Fig. 6.2(a). To determine the pigment concentration and changes under the different growth conditions, the pigments are extracted in 95% ethanol. An example spectrum is shown in Fig. 6.2(b) The equations derived by Lichtenthaler *et al.* [120] are used to calculate the pigment concentrations and ratios.

The pigment concentrations and their ratios can provide information about the functional changes in how the plant dissipates collected light and the response to ROS. The main wavelengths used were ∼660 nm for Chl *a*, ∼645 nm for Chl *b*, and 470 nm primarily for the Car. In general, different Car have similar molecular structure and their spectral signatures overlap, making it difficult to extract concentrations of specific Car. However, the total Car content, or the relationship of Car to total Chl content, can be a sign of oxidative stress in plants since Car can function as an antioxidant. It is also known that Car contribute to NPQ of ChlF. Therefore, a change in Car content can mean changes in the activity of NPQ. While NPQ is most commonly measured via PAM-F as discussed in Chapter 3, it can also be observed on the ps–ns timescale if using fs pulse durations for excitation of ChlF [147, 167, 195, 196], and in few cases, has been used to identify signatures of stress in moss.

Figure 6.3(a) shows an example ChlF spectrum, and the two peaks corresponding to the two photosystems, PSII and PSI, are at 675 nm and 720 nm, respectively. They are shaded in the respective colors of their temporal decay shown in Fig. 6.3(b). The area under each peak was calculated as a function of time to find that it decays exponentially and lasts approximately 5–8 ns. The time constants extracted from the exponential fits were in the range of 1.0–2.5 ns. The time constant can be dependent on many factors, such as Chl *a* concentration (triple-state annihilation) and NPQ mechanisms (energy transfer from Chl *a* to Car). To observe whether one photo-

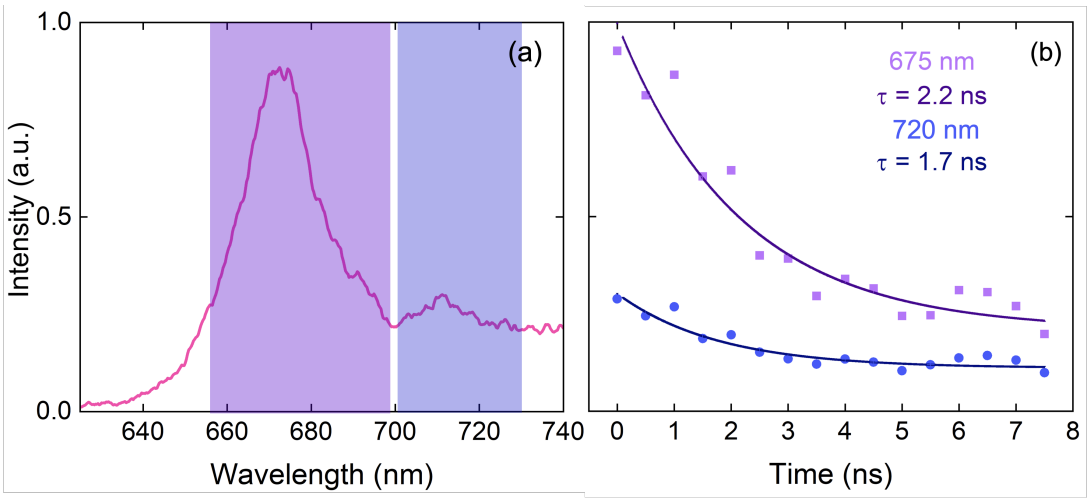

Figure 6.3: (a) Example chlorophyll fluorescence spectrum recorded for suspended thylakoid membranes, where the two main peaks of interest are shaded in colors corresponding to the plot in (b). The spectrum is recorded with a 0-ns delay with a 10-ns integration window, and 500 laser shots are averaged. (b) Temporal decay of the main peaks of interest in the ChlF spectrum shown in (a), along with their exponential fits. The initial gate delay is 0 ns. Each spectrum is recorded with a 3-ns gate width in 0.5-ns time steps up to 7.5 ns. Figure adapted from Ref. [61].

system is affected more than the other, the ratios of the lifetimes for the two peaks ($\tau_{675\ \mathrm{nm}}/\tau_{720\ \mathrm{nm}}$) were compared.

The drought stress scenario was investigated to confirm observations in previous works studying moss response to drought with *in-vivo* fs-LIF [167, 195, 196]. Prior work reported the lifetime of the peak at 675 nm corresponding to PSII decreased, while that of the peak at 720 nm corresponding to PSI remained either unaffected or mildly affected. In order to determine if a similar response was observed in *A. thaliana*, the ratio of the lifetime of the two peaks were compared, as shown in Fig. 6.4(a). There was a decrease in the lifetime ratios observed for drought conditions, whereas the control case showed a continuous increase over time. A decrease in the lifetime ratio corresponds to a decrease in the lifetime of the PSII ChlF peak with respect to the lifetime of the PSI ChlF. It is well-known that the PSII site is involved in converting water into H^+ and O_2 and producing electrons for the remaining photosynthetic electron transport chain. Therefore, in a drought scenario, the activity of this site

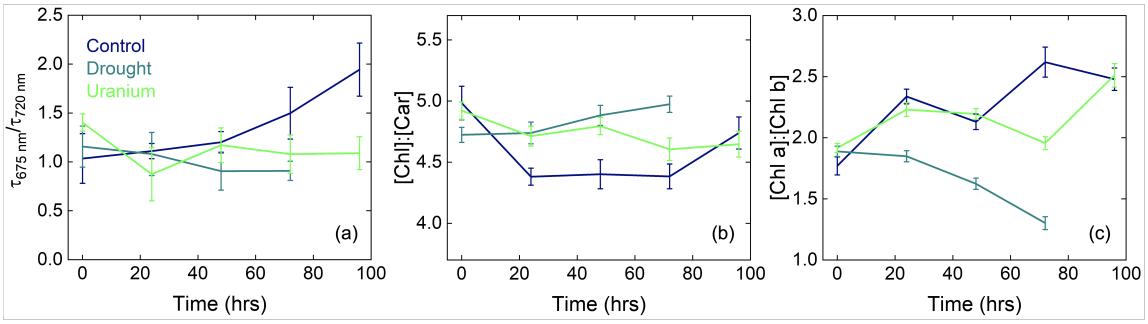

Figure 6.4: (a) Fluorescence lifetime ratios determined via fs-LIF time-dependent spectroscopy; (b) Concentration of the total Chl content with respect to total Car content as a function of time since initial exposure to stress determined from the steady-state absorption spectrum; (c) Concentration of Chl *a* with respect to Chl *b* as a function of time since initial exposure to stress determined from the steady-state absorption spectrum.

will decrease, and be more likely to transfer energy to the accessory pigments through NPQ.

The variation [Chl]:[Car] was inspected, as shown in Fig. 6.4(b), along with [Chl *a*]:[Chl *b*], as shown in Fig. 6.4(c). A slight increase in the [Chl]:[Car] ratio for the drought stress was observed, and a simultaneous and more notable decrease in [Chl *a*]:[Chl *b*]. While Car are heavily involved in stress remediation through quelling ROS and alleviating excess energy collected by Chl *a*, Chl *b* often becomes dominant over Chl *a* under stress. It is important to note that the decrease in [Chl *a*]:[Chl *b*] over time is greater than the increase in [Chl]:[Car], indicating the level of Car is still significant with respect to [Chl *a*] and are likely contributing to NPQ, evidenced by the lifetime ratios in Fig. 6.4(a). This result confirms previous observations where there is a respective decrease in the lifetime of the 675 nm peak associated with PSII for drought stress, and is correlated with a reduction in [Chl *a*] with relatively consistent [Car].

Similarly, the relationship between lifetime ratios and uranium exposure can be examined. As shown in Fig. 6.4(a), a significant decrease in the lifetime ratio for the U-stressed plant was observed after 24 hrs of exposure, whereas the lifetime of

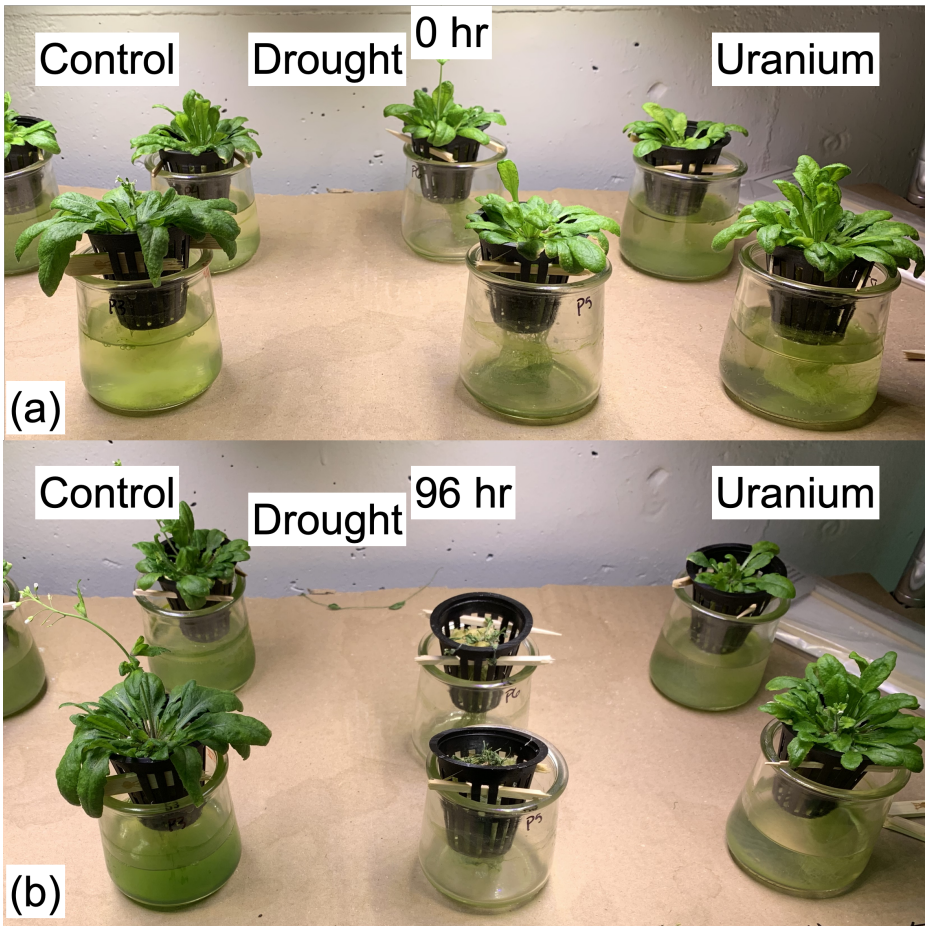

Figure 6.5: *A. thaliana* plants at beginning of exposure, 0 hrs (a), and final day of measurements, 96 hrs (b).

the control case slightly increased. A decrease in the lifetime ratios means that the lifetime of the 675 nm peak decreased with respect to the lifetime of the 720 nm peak. This could be a sign of increased NPQ in PSII. At 48 hrs and later, however, the lifetime ratio of the U-stressed plant increased and remained relatively constant over the remainder of the experimental period. This observed trend indicates a rapid "shock" response during which the greatest amount of uptake occurred in the first 24 hrs, and after 24 hrs there may have been a reduction in uranium uptake. Interestingly, in the case of uranium exposure, the lifetime ratios appear well-correlated with changes in [Chl]:[Car], which is evidence of a strong relationship of with NPQ. For the control, there is no clear relationship between [Chl]:[Car] and [Chl *a*]:[Chl *b*];

however, in general there appears to be a greater [Chl *a*] and lower [Chl]:[Car] for the control case compared to the stressed plants. Although increased NPQ can also be associated with an increase in [Car] [10, 131], previous work reports oxidation and increased production of other proteins such as glutathione can also be signs of stress associated with ROS formation [184, 185]. Further work is needed to identify if there is a relationship between enzymic proteins, NPQ, and fs-LIF lifetimes of Chl. Increased NPQ is common for heavy metal stressed plants [10, 131]; however, previous work found that NPQ decreased upon exposure of 18-day old *A. thaliana* to 50 µ M $UO_2(NO_3)_2$ [184]. While a similar effect is not observed here, the concentration of uranium and age of *A. thaliana* may influence the stress response. Both the results in this study and the work by Vanhoudt *et al.* [184] support that *A. thaliana* is resistant to uranium exposure.

Figure 6.5 presents photographs of the plants used in this study at the start of the experiment, 0 hrs of exposure, to the final measurement at 96 hrs of exposure. Here, it is clear that the drought plants had died, however the uranium-exposed plant leaves still visibly appeared healthy. Despite the observed recovery and appearance of health in the leaves, Fig. 6.6(a) and (b) show that there are signs of stress that were not evidenced in the leaves, such as inhibited root growth with extended exposure to uranium. Figure 6.6(a) shows an image of the roots of the control plants, which were dense and long. In Fig. 6.6(b), the roots of the uranium-exposed plant are shown were significantly lower density. It is likely that the stress response could take longer than the 96 hrs of this study to be evidenced in leaf measurements. A potential explanation for the "shock" response and recovery is phytostabilization of uranium by the *A. thaliana* plant, which would minimize further uptake of uranium after the initial exposure. Phytostabilization occurs by a plant emitting chelating or stabilizing species from their roots to avoid uptake of toxic materials, either through precipitation on their roots or stabilizing the movement of the species in the soil and water [203].

It is well-known that uranium binds with phosphorous and may precipitate out of solution upon interaction with phosphorous or phosphorous-containing compounds. Figure 6.6(c) shows the evidence of yellow precipitation in the container in which the uranium-exposed plants were confined. The only yellow-colored component of the simplified hydroponic nutrient solution is uranium, and therefore it is highly likely this precipitation contained uranium. Furthermore, no precipitate was observed in any other containers. Further work is needed to confirm the composition of the uranium precipitates and to determine if phytostabilization occurs under these conditions.

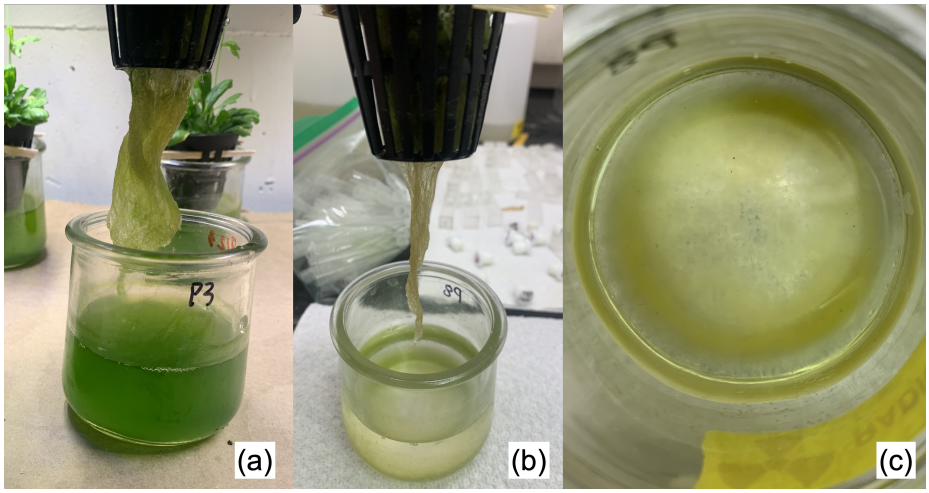

Figure 6.6: (a) Roots of control plant demonstrating long, thick, healthy roots. (b) Roots of uranium-exposed plant demonstrating significantly inhibited root growth, despite appearance of healthy leaves. (c) Precipitation in the uranium-exposed plant growth container.

Lastly, a notable observation during this experiment is the presence of algae in the hydroponic containers used in this study. It was observed that after 96 hrs, there is growth of algae in the containers for the control, as shown in Fig. 6.5 and Fig. 6.6. However, for the uranium-exposed *A. thaliana*, no algae is clearly observed. For this reason, it is possible that the presence of uranium prevents the growth of algae in the environment and may be toxic to green microalgae. It is also known that algae uptakes nutrients from solution for growth, along with *A. thaliana*, which may influence the results reported in this section. Algae may be more sensitive to direct exposure to

uranium than *A. thaliana*, presenting the potential to be a more pervasive and rapid biosensor for uranium contamination in the environment. In the following section, early time-scale exposure of the green alga *Chlamydomonas reinhardtii* is investigated to determine the feasibility of algae as a biosensor for nuclear activity.

6.2 Filament-induced fluorescence of *Chlamydomonas reinhardtii*

Here, ultrafast laser filament-induced fluorescence of chlorophyll in the green alga *Chlamydomonas reinhardtii* is studied and found to be a promising method for remote, in-field detection of stress from exposure to nuclear materials. This method holds an advantage over broad-area surveillance, such as SIF monitoring, when targeting excitation of a specific plant would improve the detectability, for example when local biological density is low. After exposing *C. reinhardtii* to uranium, the concentration of Chl *a*, ChlF lifetime, and Car content increased. The combination of increased Car content with increased fluorescence lifetime signifies a decrease in NPQ and production of ROS, as evidenced in the steady-state absorption spectrum. This is potentially a unique signature of uranium, as previous work finds that heavy metal stress generally increases NPQ. The temporal profile of the chlorophyll fluorescence is identified to be a distinguishing feature between uranium-exposed and unexposed algae. Discrimination of uranium-exposed samples is possible at a distance of $\sim$35 m with a single laser shot and a modest collection system, as determined through a combination of experiment and simulation of distance-scaled temporal profiles. Illustrating the potential for remote sensing, detection over 125 m would require 100 laser shots, commensurate with the detection time on the order of 1 s.

6.2.1 Experiment

6.2.1.1 Test species and growth

C. reinhardtii algae is obtained from the University of Texas Culture Collection of Algae (UTEX #90). An axenic culture was prepared in Hoagland solution [94]. A small portion of *C. reinhardtii* was transferred from the agar to two glass flasks containing 50 mL of nutrient growth media using a sterilized metal spatula. The flask apertures were sealed with Parafilm and placed under grow lights (390–730 nm) with a photon flux density of 120 µmol/s m^2 (25 W/m^2) and a light cycle of 12-hr on:12-hr off. The algae were propagated for three weeks before beginning the experimental exposure, with a cell density of 300,000 cells/mL.

6.2.1.2 Stress exposure

In order to optimize conditions for uranium uptake, a simplified Hoagland nutrient solution was prepared following the procedure outlined by Hayek *et al.* [89]. Briefly, the solution consisted of $MgSO_4$, KCl, NH_4NO_3, $NaHCO_3$, and $UO_2(NO_3)_2{\cdot}6\ H_2O$ (provided by the Inorganic Materials and Nanomaterials Lab at the University of Nevada Las Vegas) for the uranium exposure. The concentration of $UO_2(NO_3)_2$ in solution is 500 µM, and the pH of the solutions was monitored to be at ∼5. In order to transfer the algae from the nutrient growth media to the experimental media, four 5 mL samples from each stock algal media were extracted and centrifuged for 5 min at 3000 rpm to form a pellet. The remaining growth media were disposed, the pellets were washed once in DI water, centrifuged a second time, and resuspended in the experimental media. Two samples from each stock media were resuspended in the control solution (simplified Hoagland without uranium) and the remaining two samples from each stock media were exposed to the 500 µM of uranium in simplified Hoagland solution. The samples were stored in glass flasks, sealed with parafilm, and

agitated twice for 1 minute each over a 24-hour period.

6.2.1.3 Steady-state absorption and filament-induced fluorescence

Steady-state absorption spectra were recorded with a Varian Cary 50 UV-VIS-NIR spectrophotometer, with a spectral range of 190–1100 nm. Measurements were made 1 hour and 24 hours after stress exposure. The experimental schematic for filament-induced fluorescence (F-IF) is shown in Fig. 6.7. A Ti:sapphire CPA system was used, operating at a central wavelength of 790 nm, 480 Hz, 50-fs pulse duration, and an output energy of up to 18 mJ. A half-wave plate was used to control the power of 395-nm light generated after passing through a 200-µm-thick Type I β-$Ba(BO_2)_2$ crystal for SHG. A dichroic mirror was used to reject any residual 790-nm light, and the final energy after SHG was ∼80 µ J. This resulted in a peak power of 1.6 GW, greater than the critical power for self-focusing at ∼395 nm of ∼0.3 GW. The multiple-filament regime generally requires $\gtrsim 10 \times P_{cr}$ [15] and has not been reached. The Gaussian beam diameter was 22 mm, and the filamentation process was seeded with a 75-cm-focal length lens ($f/30$). A 1-cm path length quartz cuvette (Thorlabs, CV10Q35FA) containing the algae samples was placed approximately 50 cm after the termination of filament, resulting in a total excitation distance from the focusing lens of 1.25 m. The filament formed approximately 1 cm prior to geometric focus, and the plasma channel length was ∼3 cm as estimated from its optical emission. The F-IF was collected transverse to to the laser propagation direction with an electron multiplying-ICCD (EM-ICCD, PI-MAX4 Princeton Instruments) coupled to a variable telescopic lens. Two filters were used to isolate the main ChlF bands, one with a central wavelength of 675 nm and a 20-nm-FWHM and another with a central wavelength of 720 nm and a 10-nm-FWHM (Andover). Time-integrated and time-resolved fluorescence measurements were recorded after 24 hours of sample exposure.

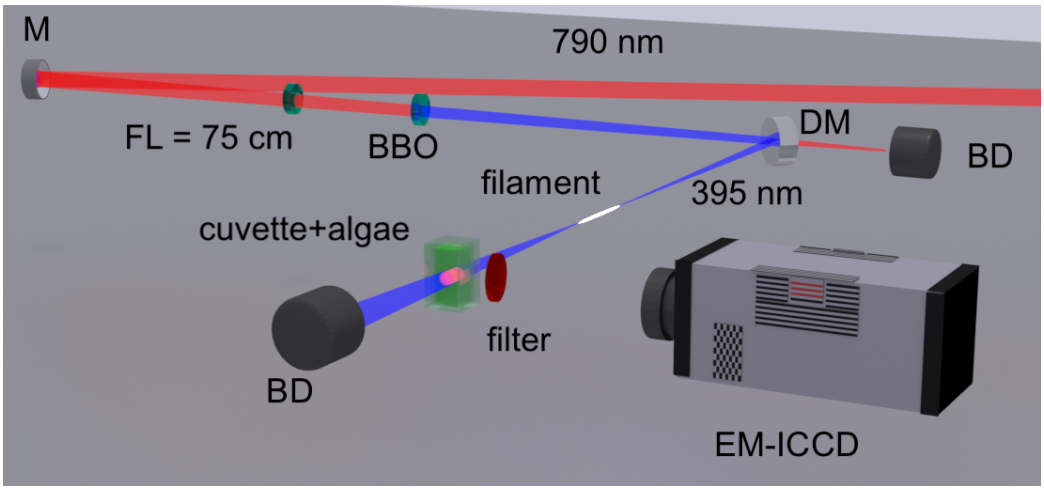

Figure 6.7: Experimental schematic for the filament-induced fluorescence imaging of algae samples. BD: beam dump; DM: dichroic mirror; FL: focal length; M: mirror.

6.2.2 Results & Discussion

6.2.2.1 Filament excitation and imaging analysis

Figure 6.8(a) shows the filament excitation spectrum and a typical absorbance spectrum of the *C. reinhardtii* samples. The filament spectrum is measured with an integrating sphere and a fiber-coupled spectrometer (CCS200, Thorlabs) at the position where the samples are placed. The 395-nm peak from second-harmonic generation (SHG) of the fundamental laser wavelength can be seen. In Fig. 6.8(b), an example ChlF spectrum and the transmission spectrum for each of the two bandpass filters (BPFs) is shown; each filter isolates the emission from a single peak. When measured *in vivo*, the two peaks are generated mainly from different photosystems in the photosynthetic chain [28]. PSII primarily fluoresces at 675 nm, while PSI fluoresces at 720 nm. Fluorescence from each of the two peaks is measured separately to examine their response to uranium exposure. Example fluorescence images recorded with an EM-ICCD detector are shown in Fig. 6.9(a) and (b) for the 675 nm BPF and 720 nm BPF, respectively. To determine the total intensity, the images are cropped to contain only the aperture of the BPF, as depicted by the red outlines in Fig. 6.9(a)

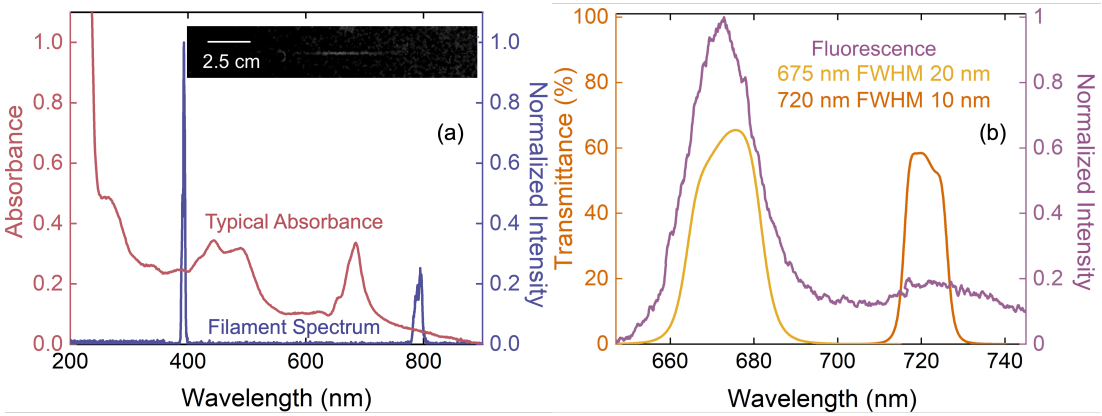

Figure 6.8: (a) Typical absorbance spectrum of *C. reinhardtii* and the filament excitation spectrum overlaid. The inset shows an image of the filament used for this experiment. (b) Example ChlF spectrum and the transmission spectra of the two spectral filters used for imaging.

and (b), and then integrated. A cuvette containing water is used as a background image, which is subtracted. Images are also recorded at various delays with respect to the arrival of filament pulse to measure the ChlF lifetime, which is typically ∼700 ps–1 ns upon fs-laser excitation [147, 167, 195, 196]. Here, the fluorescence lifetime is defined as the constant of the exponential fit, *i.e.*, the time it takes the fluorescence intensity to drop to 1/e × its initial value. Figure 6.9(c) shows example time dependence of the fluorescence intensity in each peak; exponential fits are used to extract the lifetimes. These fluorescence lifetimes can provide information on NPQ of ChlF by Car, especially in combination with the measurement of pigment concentration.

6.2.2.2 Influence of uranium exposure on fluorescence parameters

Figure 6.10 presents the fluorescence lifetime, lifetime ratios, and overall intensities for each sample. The stock solutions are labeled by the number in front of a letter, where "C" stands for control and "U" stands for uranium. The labels "a" and "b" underneath denote each of the two samples per stock solution per condition. The thick lines on top of the four bars represents the mean value for four samples. As shown in Fig. 6.10(a) and (b), the mean fluorescence lifetime for both the 675-nm and 720-nm

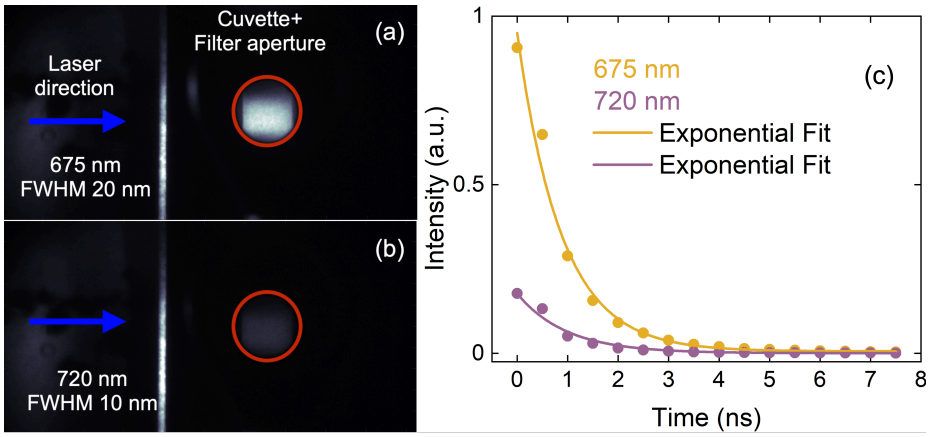

Figure 6.9: Fluorescence images recorded with the (a) 675-nm BPF and (b) 720-nm BPF. The red outlines define the region over which the total fluorescence intensity is integrated. Temporal profile of the two peaks (c), where the initial delay is 0 ns, the time step is 0.5 ns, and the gate width is 4 ns.

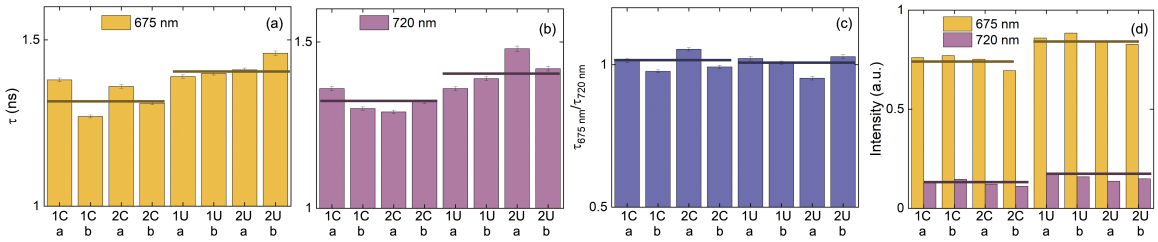

Figure 6.10: Lifetimes extracted for the (a) 675-nm peak and (b) 720-nm peak; (c) the ratio of the lifetimes used to identify preferential disruption to PSII or PSI during stress; (d) time-integrated intensity for both peaks and all exposure conditions. The lines across the top of the bar graphs represent the mean. The control and U-exposed samples have the following means and error, respectively: (a) 1.33±0.02 and 1.41±0.02; (b) 1.31±0.01 and 1.40±0.03; (c) 1.01±0.02 and 1.00±0.02; (d) 0.75±0.02 at 675 nm, 0.13±0.01 at 720 nm and 0.85±0.01 at 675 nm, 0.16±0.01 at 720 nm.

peaks were longer for the uranium exposed algae; however, in Fig. 6.10(c) the ratio of the lifetimes was approximately the same for the uranium exposed samples as for the control case. This implies that both photosystems are likely affected simultaneously by uranium stress. Lastly, the time-integrated signal intensity was greater for the uranium-exposed algae in both peaks. An increase in total ChlF intensity may be due to increased Chl content. To confirm this observation, the pigment concentration were evaluated for all samples using the UV-VIS-NIR absorption spectrum.

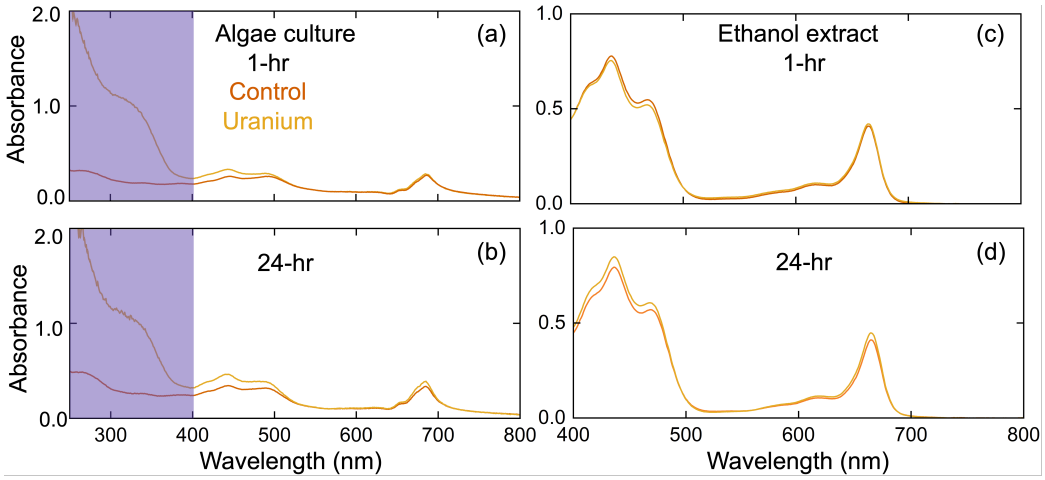

Figure 6.11: Representative absorbance spectra for the control and U-stressed algae at (a) 1-hr and (b) 24-hr exposure in growth media and the pigment extract in 95% ethanol for (c) 1-hr and (d) 24-hr.

6.2.2.3 Influence of uranium exposure on pigment content

The time-integrated fluorescence intensity at both 675 nm and 720 nm increased for the uranium-exposed algae, as shown in Fig. 6.10(d). A potential reason for the increase in fluorescence emission is the increased Chl content. Figure 6.11 presents representative absorbance spectra for the control and uranium-exposed algae after 1-hr and 24-hr exposures. As shown in Fig. 6.11(a), there was already a significant increase in absorption in the UV-region (250–400 nm) after 1 hr for the uranium-exposed samples. Furthermore, the increased absorption persisted through 24 hrs of exposure as seen in Fig. 6.11(b).

To quantify the changes in the absorption spectra, we extract the pigments from the corresponding algae samples in 95% ethanol, and use the relations introduced by Lichtenthaler [120] to determine the concentration of Chl *a*, Chl *b*, and total Car. Representative spectra for the U-exposed and unexposed algae pigment extracts at 1-hr and 24-hr exposures are shown in Fig. 6.11(c) and (d). The results are shown in Fig. 6.12(a) and (c) for the 1-hr exposure and in Fig. 6.12(b) and (d) for the 24-hr exposure. After 1 hr of exposure, no change was observed in the Chl *a*, Chl *b*, and total

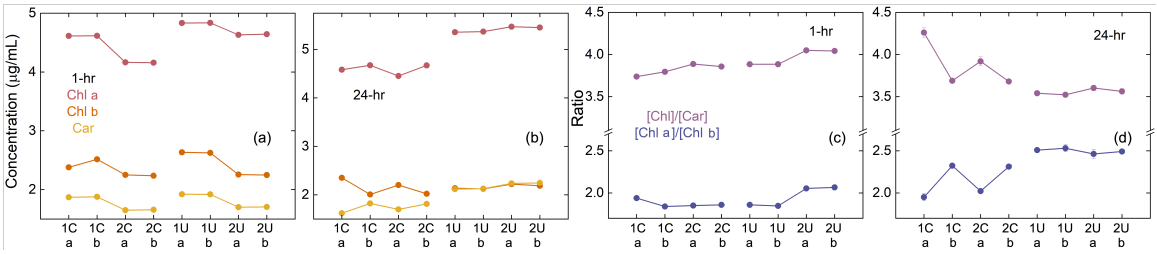

Figure 6.12: Pigment concentrations for each of the samples at (a) 1 hr and (b) 24 hrs after exposure to U. The mean Chl a, Chl b, and Car concentrations (µg/mL), respectively, of the control samples for 1 hr: 4.4, 2.4, and 1.8 & 24 hr: 4.6, 2.2, and 1.7. The mean concentrations of the U-exposed samples for 1 hr: 4.7, 2.4, and 1.8 & 24 hr: 5.4, 2.2, and 2.2. Relevant pigment ratios for each of the samples at (c) 1 hr and (d) 24 hrs after exposure to U. The mean [Chl a]/[Chl b] and [Chl]/[Car] ratios of the control samples for 1 hr: 1.8 and 3.7 & 24 hr: 2.2 and 3.8. The mean respective pigment ratios of the U-exposed samples for 1 hr: 1.9 and 3.9 & 24 hr: 2.6 and 3.4.

Car concentrations.The [Chl] notation represents the sum of the concentration of Chl *a* and Chl *b*. After 24 hrs of exposure, an increase in Chl *a* and Car concentration was observed for the uranium-exposed algae; furthermore, the [Chl]:[Car] ratio was lower for uranium exposed samples than unexposed samples, having decreased from ∼3.8 to 3.4. This trend suggests that the change in concentration of Car increases more than the total change in Chl concentration when compared to the control case after 24-hrs of exposure. It is important to note that any changes in the photosynthetic apparatus, such as pigment and protein composition or pigment degradation under stress, can influence the accuracy of pigment quantification [32].

6.2.2.4 Relationship between fluorescence and pigment content

The dependence of the fluorescence lifetime and intensity on the pigment concentrations is next examined. First, for both the control and the uranium case there was a decrease in $I_{675\ nm}$ with increasing [Car]. Similarly, this trend was observed for the 720-nm peak in (c) and (d). It is understood that Car assist in NPQ of ChlF to alleviate overly excited Chl from causing photosystem damage, which could explain the decrease in fluorescence intensity with increasing Car content. There was also

a decrease in $I_{675\ nm}$ with increasing [Chl *a*] due to reabsorption of the fluorescence emitted by Chl *a*, which was less apparent for the 720-nm peak due to the absence of absorption by Chl *a* at this wavelength. There may be absorption of fluorescence by the cell wall; the turbidity level is related to the cell density, and therefore may also be related to the decrease in fluorescence measured.

One way to assess the level of NPQ is to observe changes in the fluorescence lifetime and the relationship to [Car]. When comparing $\tau_{675\ nm}$ to the [Car], the control samples followed the expected trend of decreasing lifetime, as seen in Fig. 6.13(e). This is representative of increased NPQ, in which Chl *a* can dissipate of excess energy by transfer to Car. The other pathway of fluorescence quenching is through photosynthesis. On the other hand, with the uranium-exposed samples, the increase in [Car] generally resulted in a longer $\tau_{675\ nm}$. This implies decreased NPQ; a similar trend is observed for the $\tau_{720\ nm}$ peak. The fact that this correlation between [Car] and τ was apparent for both wavelengths suggests that neither PSII or PSI are predominantly attacked upon uranium exposure.

6.2.2.5 Remote sensing of uranium exposed algae

Femtosecond laser filamentation enables remote excitation of optical signatures. In order to assess the potential for remote sensing using this approach, it is important to determine the distance at which these optical signatures can be measured. The ChlF lifetimes of the uranium-exposed algae samples were distinct from the controls; therefore, the shape of the temporal profile is promising for identification of the stress. The performance of this discrimination method was assessed by comparing the temporal profiles recorded with the 675-nm BPF of the four control and uranium-exposed samples, as shown in Fig. 6.14(a). The profiles were normalized so that the shape can be compared. In order to quantify this difference, the ratio of two segments of the profile, labelled "*A*" and "*B*" in Fig. 6.14(a) were calculated. The start of

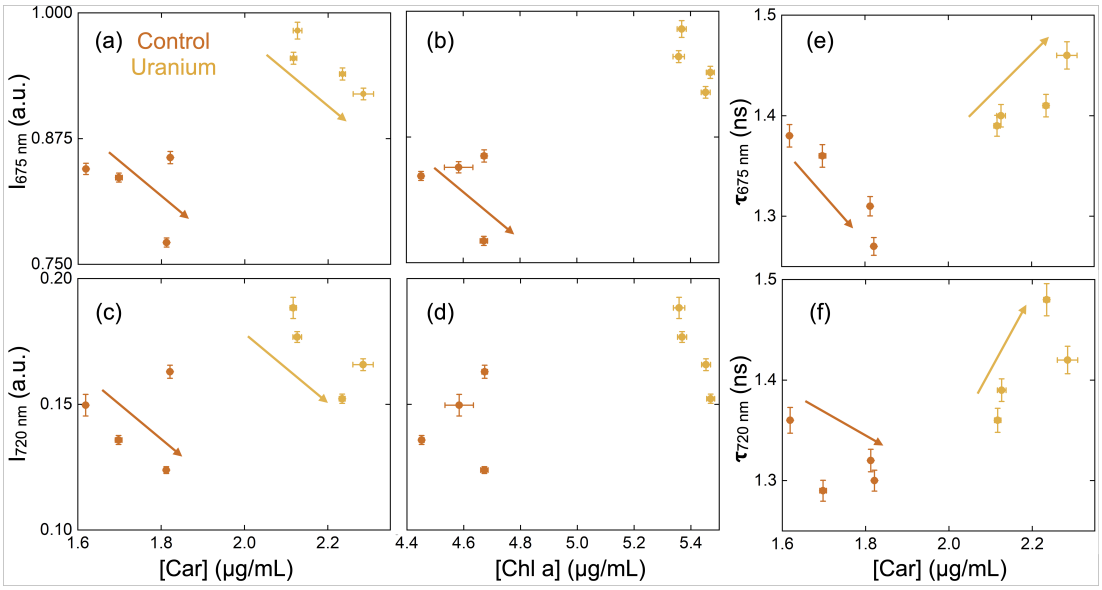

Figure 6.13: Time-integrated fluorescence intensity for the 675-nm peak as a function of (a) [Car] and (b) [Chl a]; similarly for the 720-nm peak in (c) and (d), respectively. The fluorescence lifetime as a function of [Car] for the (e) 675-nm peak and (f) 720-nm peak.

segment "B" is varied to maximize the distinction between the control and uranium-exposed profiles using a figure of merit (FOM) defined as FOM$= (\mu_U - \mu_C)/(\sigma_C + \sigma_U)$, where μ_U and μ_C are the mean B/A ratio and σ_U and σ_C are the standard deviations of this ratio for the uranium-exposed and control algae, respectively. The optimal start time for the segment "B" was found to be 1.5 ns. The detection probability was assessed by generating a normalized Gaussian distribution based on the mean B/A ratio and standard deviation for both the control and the uranium-exposed algae samples separately, setting a threshold of $B/A = 0.206$ above which positive detection was assumed. At the distance of 0.15 m where the temporal profiles were recorded, this resulted in a single-shot detection probability of 90% and a false alarm probability of 5%.

To evaluate the potential to discriminate uranium-exposed algae from the control at greater distances, an isotropic source is assumed and its intensity is scaled with

distance (r). The B/A ratio is defined as

$$B/A(r) = \frac{[B \times (r_0/r)^2 + BG \times (t_B/t_A)] - BG \times (t_B/t_A)}{[A \times (r_0/r)^2 + BG] - BG}, \tag{6.1}$$

where BG is the time-integrated ambient background, t_B is the total integration time for segment B, t_A is the total integration time for segment A, $r_0 = 0.15$ m is the reference distance, and r is the distance.

A and B have experimentally determined uncertainties, σ_A and σ_B. They are defined as the standard error of the measurements performed at the reference distance $r_0 = 0.15$ m for the four controls and four uranium-exposed samples. The standard error in the ambient background (σ_{BG}) that is subtracted from the signal is also taken into account, and was measured in the laboratory environment with identical detector settings. The uncertainties associated with A, B, and BG, also scale with the number of averaged laser shots n, and the final distance-dependent uncertainty is calculated as

$$\sigma_{B/A}(r,n) = \left\{ \left[\left(\frac{t_B/t_A}{A(r_0/r)^2} - \frac{B}{A^2(r_0/r)^2} \right)^2 \sigma_{BG}^2 + \left(\frac{B}{A^2(r_0/r)^2} - \frac{t_B/t_A}{A(r_0/r)^2} \right)^2 \sigma_{BG}^2 + \frac{B^2\sigma_A^2}{A^4} + \frac{\sigma_B^2}{A^2} \right] /n \right\}^{1/2}. \tag{6.2}$$

The distance-dependent uncertainty in B/A was calculated for both the control and uranium-exposed algae samples for a single-shot measurement, 100 shots averaged, and 500 shots averaged, as shown in Fig. 6.14(b). Above ∼35 m, a notable increase in the standard error is observed for the single-shot measurement. The impact of this change is also observed in Fig. 6.14(c), where the detection probability remains constant below ∼35 m, and at greater distances the differences between the two profiles cannot be be discerned. The detection probability decreases with distance until it equals the false alarm rate. The false alarm and detection probabilities

were calculated using the same critical limit set by the close-up measurement, which is denoted by the horizontal black line in Fig. 6.14(b). The detection distance can be increased by accumulating the signal from multiple laser shots. The Currie criterion for minimum level of detection states the false alarm rate must be $\leq$5% with associated detection probability of $\geq$95% [43] to be considered a true detection. The criterion is met up to 10 m for 2 shots, at 125 m with 100 shots, and at 150 m for 500 shots. With modern ultrafast laser systems having the ability to operate at $\sim$1-kHz repetition rate and assuming a comparable data acquisition system, the total measurement time of 1.6 s is required for 16 sample points across the time profile with accumulations of 100 shots. This analysis was based on the collection system used in the present experiment, the 500 µM uranium concentration, and 24-hr exposure period. Larger collection optics could improve the collection efficiency, and therefore the distance at which the signatures could be measured. Exposure that extends beyond the 24-hr time-frame studied here could influence the magnitude of the algae stress response, resulting in a greater discrimination capability between the uranium-exposed and control algae.

Another important aspect of remote detection is the delivery of excitation energy. An input energy of 80 µJ was found to be sufficient to generate a filament in the air over a distance of 1.25 m and excite ChlF in *C. reinhardtii* without causing noticeable damage to the sample. However, to generate a filament that will allow for confinement of the laser energy over much greater distances requires higher peak laser power. The formation of filaments on the order of kilometers away from the laser source has been demonstrated [154], and filament ablation has been performed at a distance of 90 m using 800-nm driving wavelength and 250-mJ input energy [156]. Multiphoton ionization at 395 nm occurs at a significantly higher rate than at 800 nm, which results in rapid loss of energy with extended propagation through the filament plasma. To avoid this, one can use a telescopic focusing system, dispersion control,

or a combination of both methods such that the filament formation distance can be controlled and formed much closer to the sample location [126]. Previous work exploring filamentation at various driving laser wavelengths and energies found that the energy loss after filamentation is about 25% at 0.5 mJ and 50% at an input energy for 4 mJ for filaments formed with $f/40$ focusing conditions [26]. Similar focusing conditions are used here for filament formation, but due to the low initial energy, the results from Ref. [26] were extrapolated to find approximately 10% energy loss at 80 µJ. Therefore ∼70 µJ of energy reached the algae samples in this experiment. Linear absorption through the atmosphere also needs to be accounted for in the extended delivery of laser energy. The predominant absorbing species in atmosphere for 395 nm light is NO_2, with a cross-section of 5×10^{-19} $cm^2molecule^{-1}$ [143]. With a propagation distance of ∼100 m for detection with 100 laser shots and an estimated concentration of 6.5×10^{14}molecules cm^{-3} [2], the absorbance is 3.25, resulting in ∼0.06% of the light transmitted over 100 m through the atmosphere. To provide ∼80 µJ for sample excitation, taking into account both the linear absorption and the filament energy loss of ∼50%, an initial energy of ∼260 mJ would be required. Air turbulence and scattering can influence the initial energy needed to have sufficient energy at the sample position.

Within the 24-hr exposure, there did not seem to be a decrease in photosynthetic efficiency, as signified by the increase in Chl *a* content. A potential reason for increased Chl a content, despite being exposed to a toxic heavy metal like uranium, is the addition of nitrate to the growth media. Nitrate is a known nutrient to plants that promotes photosynthetic activity, and may simultaneously have an influence with uranium uptake. However, the increase in [Car] is generally a sign of stress, in particular when the increase in [Car] is large such that [Chl]:[Car] is lower than that observed for the healthy case. A decrease in [Chl]:[Car] ratio is often observed in plant stress, especially associated with the production of ROS during drought stress

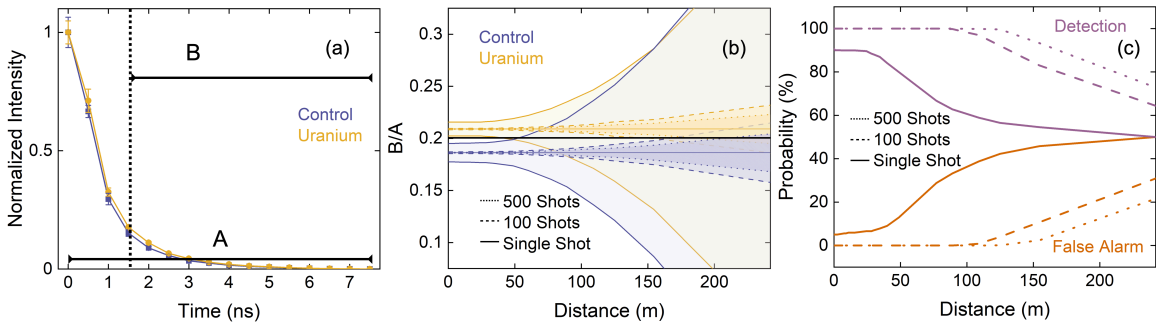

Figure 6.14: (a) Mean temporal profiles for the four control and four uranium-exposed algae samples, where the error bars represent 1-σ standard deviation in the intensity at that time step. Segment "B" begins at 1.5 ns and "A" is the integral of the entire time profile. (b) B/A calculated from the measured temporal profiles at 0.15 m, and the distance-dependent uncertainties for measurements made with a single shot, 100 shots, and 500 shots. The black horizontal line denotes the critical limit set for determining the detection and false alarm probabilities. (c) Detection and false alarm probabilities as a function of distance determined from integrating the Gaussian distributions formed from the B/A and 1-σ uncertainty calculated in (b).

or heavy-metal exposure [10]. In the case of drought, it has been observed that there is a substantial increase in NPQ due to the plants' need to dissipate excess energy held by Chl *a* when it has minimal access to water to process, primarily at PSII. Previous work by Shibata *et al.* [167] and Yamakawa *et al.* [195, 196] found that the time-integrated intensity and lifetime of the 675-nm peak was significantly decreased upon *in-vivo* fs-LIF of drought-tolerant moss as a result of increase NPQ. PSII is the main site involved in processing water in the photosynthetic chain [28], and this is the hypothesized reason for the observed decrease in 675-nm peak fluorescence intensity and lifetime, while the 720-nm peak did not exhibit as notable of a change.

Other than by disruption of the electron transport chain, there are several proposed mechanisms for uranium toxicity to plants, such as the substitution of Ca^{2+} and Mn^{2+} sites [5]. These chemical changes can influence the function of a photosystem. Since fs-LIF was able to identify a change in the fluorescence related to a specific photosystem under drought stress in previous experiments [167, 195, 196], the ratio of the lifetime of each peak was compared in this work in order to identify if one

photosystem is undergoing a greater amount of quenching than the other for uranium exposure, as shown in Fig. 6.10(c). It was observed, however, that despite having overall increased fluorescence lifetimes upon uranium exposure, the $\tau_{675\text{ nm}}/\tau_{720\text{ nm}}$ ratio was consistent with the control case. This may mean that one photosystem was not being affected more than another within the time-frame of this study. This does not necessarily indicate that uranium was not detrimentally influencing the electron transport chain. In previous work, replacement of Mn^{2+} in the water processing PSII by uranium was shown to influence the entire photosynthetic chain [5], and this may be the reason for the observed similar $\tau_{675\text{ nm}}/\tau_{720\text{ nm}}$ ratio between uranium-exposed and unexposed algae. The speciation of U in solution can affect uptake, and precipitation out of solution can occur under certain conditions [65, 89, 159, 184]. With elevated levels of U in solution, there is an increased likelihood of U precipitation, which can negatively impact uptake [52]. We note that no uranium precipitates were observed in solution or in the algal pellets during this study, and therefore assume that uranium remains in the aqueous form over the duration of the experiment.

Although comparing the two photosystems does not provide information about uranium stress, an increase in the lifetime of the 675-nm and 720-nm peaks upon exposure to uranium was observed. This implies a decrease in NPQ. Previous work by Vanhoudt *et al.* observed a similar response upon uranium exposure to *Arabidopsis thaliana*, along with an increase in photosynthetic efficiency as measured via PAM-F [184]. Despite this being the case, the authors report that uranium is still toxic to plants, especially with prolonged exposure. The decrease of NPQ is a sign that the Car produced with uranium-exposure are likely acting as antioxidants against the ROS produced, which is confirmed by the increase in absorption in the UV (250–400 nm), as shown in Fig. 6.11(a) and (b). The majority of photosynthetic pigments absorb in the range of 400–700 nm; however, ROS such as H_2O_2 and antioxidant proteins like glutathione and ascorbate absorb in the range of 250–400 nm. Several

previous studies that investigated plants' response to uranium confirmed that there are increased levels of H_2O_2, and that glutathione and ascorbate play a significant role in remediating the response produced from uranium stress [7, 183]. Furthermore, Vanhoudt *et al.* also observed a decrease in the ratio of [Chl]:[Car] in conjunction with the decreased NPQ [184]. Although these authors studied a different plant species, *C. reinhardtii* as a green algae contains similar photosynthetic pigments as higher plants like *Arabidopsis thaliana*. For this reason, it may be possible to have some similar responses between these two species to uranium-exposure, like decreased NPQ and [Chl]:[Car].

Previous work by Herlory *et al.* measured a decrease in photosynthetic activity and an increase in NPQ in *C. reinhardtii* upon exposure to uranium in various concentrations after 5 hrs of exposure [92]. In their study they used PAM-F, and the maximum uranium concentration was 10^4 µg of U/L (or ∼25 µM) with a density of 150,000 cells/mL. In the present work, a concentration of 500 µM $UO_2(NO_3)_2$ (∼1.9×10^5 µg of U/L) and a cell density of 300,000 cells/mL were used. If the difference in cell density is accounted for, the work by Herlory *et al.* would be the equivalent of approximately 50 µM uranium in exposure to the cell density used in this study, *i.e.*, 300,000, making their maximum concentration of uranium investigated an order of magnitude lower than in this study. The differences in cell concentration, photon flux density, uranium concentration, and the amount of uranium taken up by the algae cells can all play a role in the observed differences in measurements. Furthermore, Herlory *et al.* did not report pigment concentrations, and the concentrations and interactions of the pigments have an impact on the measured fluorescence parameters. Further work is needed to determine the limit of detection for uranium-induced changes in *C. reinhardtii* under similar conditions, as well as comparing the measurements made by F-IF with more established methods such as PAM-F.

6.3 Summary

In this chapter, the effects of various stressors, such as drought and uranium contamination, on the optical properties of *A. thaliana* were investigated using steady-state absorption and fs-LIF spectroscopy. A similar response was observed in the case of drought stress that was found previously in moss via fs-LIF, and this trend may also be correlated to a decrease in [Chl *a*]:[Chl *b*] and the corresponding changes in Car content. Fs-LIF to study uranium stress in *A. thaliana* was performed for the first time, to the best of our knowledge. A significant decrease in lifetime ratio at 24 hrs after uranium exposure was seen, with an increase and relatively consistent lifetime ratio from 48 hrs and later. This suggests a uranium-induced increase in NPQ at 24 hrs of exposure. Interestingly, the changes in lifetime ratios seem well-correlated with [Chl]:[Car], further supporting the relationship between NPQ of PSII with the lifetime ratio. The recovery after 24 hrs was proposed to be from phytostabilization by *A. thaliana*, but further work is needed to confirm this. These results show that fs-LIF has potential as a monitoring method for sensing of nuclear activities, such as uranium enrichment. Further work is needed to confirm this response, and investigate how *in-vivo* measurements of *A. thaliana* leaves may influence these previously observed changes in ChlF.

Further, filament excitation of live *C. reinhardtii* algae was demonstrated to be a promising method for remote, in-field monitoring of stress and plant health. Optical signatures that can be used to identify uranium-exposure were determined. The relationship between the pigment content calculated from the absorption spectrum and the F-IF measurements were investigated to better understand how uranium influences the plant processes. There is a notable increase in absorbance in the 250–400 nm region for the uranium-exposed algae. This is attributed to an increase in the production of ROS and other antioxidant-related enzymes, such as glutathione and ascorbate, which have been reported to be essential in responding to uranium stress.

This response occurs quickly, as early as one hour after exposure, demonstrating the sensitivity of *C. reinhardtii* and the ability to facilitate uranium detection shortly after exposure. The increased absorbance persists to 24 hours after exposure, when the fluorescence measurements were made. Interestingly, signs of cell death were not observed, deduced from the observed increase in Chl *a* concentration with uranium exposure. However, there is a decrease in [Chl]:[Car], signifying an increase in [Car] which may also be a response to production of ROS. The control samples followed the trend of increased [Car] corresponding to decreased fluorescence intensity and lifetime due to the NPQ contribution of Car. On the other hand, while the time-integrated intensity decreases with increasing [Car] for uranium exposure, there is also an increase in fluorescence lifetime, or a decrease in NPQ. The combination of increased [Car] and increased fluorescence lifetime may be a unique response of uranium stress, allowing it to be distinguished from other stresses; however, further work is needed for confirmation. Lastly, the potential for single-shot remote discrimination of uranium-exposed algae from the control at a distance of $\sim$35 m is calculated, and detection at 125 m distance is possible with 100 laser shots averaged per time step, or a measurement time of 1.6 s assuming a 1-kHz laser system and comparable data acquisition system. The results of this work are promising for rapid, remote, in-field assessment of plant health and may have broader implications for pollution monitoring and nuclear safeguards.

CHAPTER 7

Transient Absorption Spectroscopy to Study Non-Photochemical Quenching in Algae

In Chapter 6, fluorescence of Chl *a* in thylakoid membranes extracted from *Arabidopsis thaliana* and live cells of the green alga *Chlamydomonas reinhardtii* was explored to identify a response from uranium uptake that could distinguish it from other stressors. One potential signature of uranium exposure that was identified, in particular for *C. reinhardtii*, is an inverse relationship between τ, the fluorescence lifetime, and [Car] from that of the control. This trend signifies a reduction in NPQ in the uranium-exposed algae. Pulse amplitude modulated-fluorometry (PAM-F) is commonly used to assess the magnitude of NPQ. Upon excitation with an ultrashort pulse of the appropriate wavelength, more specific processes that dictate molecular dynamics involved in NPQ can be explored. Furthermore, the timescale over which different mechanisms occur can be measured with sufficient timing resolution. One technique commonly employed to study the rapid molecular dynamics is a type of pump-probe spectroscopy referred to as transient absorption spectroscopy. Transient absorption spectroscopy monitors the change in the absorbance at a specific wavelength at varying time delays after excitation of a sample. The purpose of the initial light pulse (or pump pulse) is to transition electrons in a specific molecule to an energy level of interest. In the case of NPQ in plant systems, the Q_y state of Chl *a* is inves-

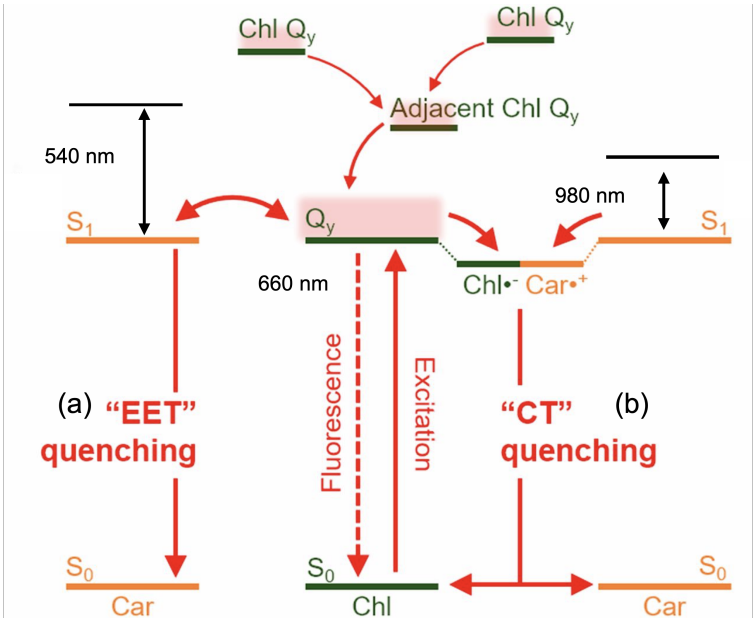

Figure 7.1: Diagram of the two dominant NPQ pathways in plants, (a) excited energy transfer (EET) and (b) charge transfer (CT). This figure is adapted from Ref. [147].

tigated because it can either directly transfer excited energy (EET) to a carotenoid energy level, or can couple with a carotenoid (zeaxanthin and lutein, primarily) to form a heterodimer which allows for charge transfer (CT) via recombination. A diagram demonstrating these energy transfer pathways is shown in Fig. 7.1. Only when Car and Chl *a* are in close proximity does the heterodimer form [146]. Therefore, a decrease in [Chl]:[Car] may result in an environment that favors CT quenching. By selecting a wavelength to excite the Chl *a* to the Q_y state, the S_1 state of the carotenoid shown in Fig. 7.1 will only be populated if the transfer from the Chl *a* Q_y state has occurred. Therefore, the purpose of the probe light pulse is to interrogate whether or not S_1 is populated. Delaying the probe pulse with respect to the pump pulse allows for the periods to populate and de-excite the relevant states to be resolved.

It can be seen from the diagram in Fig. 7.1 that the pump wavelength needs to be in the range of ∼660–665 nm, while the probe wavelength needs to be either ∼540 nm or ∼980 nm to explore two of the dominant energy transfer pathways

between Chl *a* and Car. There are other pathways that populate both states, which can be found in Ref. [174]; these other pathways are not investigated here. Specifically, in the case of plant photosystems, the cells will absorb light at the probe wavelengths even without the presence of the pump. At 980 nm, the primary absorbance is by the membrane, while at 540 nm there is absorption by carotenoid ground states. Therefore, the change in absorbance (ΔA) must be calculated by measuring $A_{\text{pump}} - A_{\text{no pump}}$ or $-\log(I_{\text{pump}}/I_{\text{no pump}})$. ΔA is dependent on several properties, such as the total pigment concentration, pigment-pigment and pigment-protein spacing, which pigments are present, and the pump and probe wavelengths used. In general, ΔA is small, usually $\lesssim$5%. Therefore, system noise, which can originate from laser energy instability, must be reduced.

Previous studies have reported the rise times of these transitions, and the lifetime of the S_1 states for the carotenoid in a few different species and isolated light harvesting complexes (LHCs) in plants [49, 95, 96, 139, 146, 147, 174]. It has been found that the EET pathway has a very rapid rise time (<150 fs), while the CT pathway is much slower ($\sim$600 fs) [146, 147, 174]. The decay constants for the EET and CT pathways are approximately 8 ps and 40 ps, respectively [147]. The goal of those studies was to better understand the molecular dynamics occurring in photosystems under extreme light exposure where NPQ is more active, under different pH gradients, and of PSI and PSII separately. Here, the overall magnitude in the two NPQ pathways will be explored for healthy and uranium-exposed *C. reinhardtii*. This work can be compared to the observations reported in Chapter 6 and help understand the mechanisms by which uranium-induced stress influences the stress response in plants.

7.1 Experiment and experimental design

7.1.1 Test species and growth

Live *Chlamydomonas reinhardtii* cells (UTEX #90) were propagated in Hoagland solution [94] for ∼4 weeks until a cell density of 3×10^5 ml^{-1} was achieved as a stock solution. During this time, the flasks containing the algae were placed under grow lights (390–730 nm) with a photon flux density of 120 µmol/s m^2 (25 W/m^2), a light cycle of 12-hr on:12-hr off, and agitated on an orbital shaker. The cells were centrifuged and suspended in a HEPES-KOH buffer (pH 7.8) to achieve a Chl *a* concentration of ∼100 µg/mL. The samples were contained in a 1 mm path length quartz cuvette.

7.1.2 Pump-probe transient absorption experiment

Figure 7.2 shows a schematic for the transient absorption experiment. The Ti:sapphire ultrafast regenerative amplifier described in Section 6.1.1 is used to pump an optical parametric amplifier (OPA) (Light Conversion TOPAS), capable of producing a 1160–2600 nm output (both signal and idler), $\lesssim$250 µJ/pulse, 0.7–1× the pump pulse duration (∼130 fs). The OPA is tuned to 1320 nm, and both residual 790 nm and 1320 nm are output from the OPA. A 790 nm reject filter is used to separate the two beams for the pump and probe arms. The residual 790 nm is first passed through a 3× beam expanding telescope and focused with a 5 cm focal length lens ($f/6$) onto a sapphire window to generate white light continuum. The sapphire window is on a translation stage, and an iris is placed before the focusing lens to control the light intensity on the sapphire window. A bandpass filter (BPF) (540 nm–10 nm FWHM or 980 nm–10 nm FWHM, Andover) is placed after the white light generation, followed by a collimating lens. A (70:30) beamsplitter is inserted so that a reference photodiode (Thorlabs DET36A, 14 ns rise time) can monitor shot-to-shot fluctuations in the

540 nm/980 nm beams. The remaining 540 nm/980 nm light is then focused onto the sample with a 10 cm focal length lens ($f/5$). For the pump arm, the 1320 nm light that passes through the 790 nm reject filter is delayed by a retroreflector on a delay stage controlled by a motorized actuator (Thorlabs Z825B) closed-loop feedback. After the retroreflector, a BBO crystal (Type I, 0.5 mm thick) is used to frequency double the 1320 nm pulse to 660 nm, and a 660 nm–10 nm FWHM BPF (Andover) is used to reject any residual 1320 nm light. The pulse energy at 660 nm is ∼1 µJ when the OPA produces maximum power output. The pulse energy at the sample target is adjusted to be ∼100 nJ, and the pump beam is focused with a 10 cm focal length lens ($f/5$). Cross-correlation measurements result in a time resolution of ∼300 fs. A signal photodiode (Thorlabs DET36A, 14 ns rise time) is placed after the sample to measure the probe beam intensity.

The samples are shaken regularly throughout the experiment to avoid settling of the algal cells. Concentration corrections are made by recording data with the pump blocked and pump present at each time step. The data acquisition system is a LeCroy 1-GHz bandwidth oscilloscope set to the 20-MHz bandwidth limit to reduce noise fluctuations in the recorded waveforms. The signal and reference photodiodes are triggered on the rising edge of a photodiode monitoring the output pulse from the Ti:sapphire regenerative amplifier. A total of 100 waveforms per photodiode per time step are recorded with and without the pump beam blocked.

7.2 Results and discussion

Transient absorption spectra can result from a convolution of multiple effects, for example excited state absorption (ESA), stimulated emission (SE), and energy transfer mechanisms [174]. Chl *a* is known to have ESA at 540 nm and 980 nm. Example transient absorption profiles are shown in Fig. 7.3(a) and (b), containing data digitized from previous work that investigated energy transfer mechanisms in

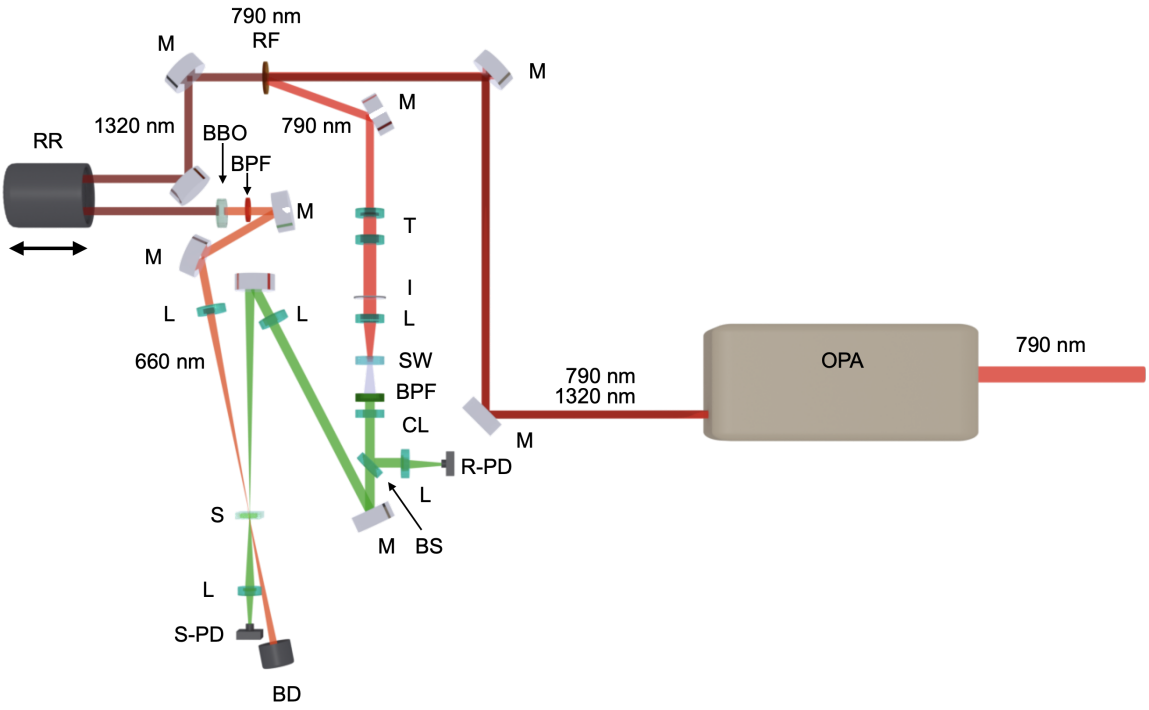

Figure 7.2: Experimental schematic for pump-probe transient absorption spectroscopy. OPA: optical parametric amplifier; M: mirror; 790 nm RF: 790 nm reject filter; L: lens; T: telescope; I: iris; SW: sapphire window; BPF: bandpass filter; CL: collimating lens; BS: beamsplitter; R-PD: reference photodiode; RR: retro-reflector; BBO: β-$Ba(BO_2)_2$ crystal; S: sample; S-PD: signal photodiode; BD: beam dump.

the green alga *Nannochloropsis oceanica* [147]. *N. oceanica* is another green, single-celled alga similar to *C. reinhardtii*, but *N. oceanica* has a smaller diameter, 2–3 µm compared to 10 µm for *C. reinhardtii*. Chl *a* only binds to violaxanthin, antheraxanthin, zeaxanthin, and vaucheriaxanthin in *N. oceanica*, whereas *C. reinhardtii* has a more complex pigment binding structure [147]. Previous studies report similar results on NPQ mechanisms in isolated LHCs of *C. reinhardtii* and extracted thylakoid membranes [49, 95, 96].

As shown in Fig. 7.3(a) and (b), ESA from Chl contributes to the recorded transient absorption traces shown in blue. Park *et al.* measured the traces in both dark and high-light (15 min of actinic light exposure to the samples) conditions so that the Chl ESA can be subtracted to obtain the red traces in Fig. 7.3(a) and (b). The ESA decay constant is approximately 35.5 ps when probed with 540-nm light and 180 ps when probed with 980-nm light. The results from both double exponential fits to the blue traces in Fig. 7.3(a) and (b) and the single exponential fits to the red traces result in similar decay constants for the EET and CT pathways. Park *et al.* report a 7.71-ps decay for the EET pathway and a 43-ps decay constant for the CT pathways [147]. The measured decay constants shown in Fig. 7.3(a) and (b) are slightly different, which could be due to the digitization and fewer data points than reported in Ref. [147].

Based on the results presented in Chapter 6, the effect of uranium exposure on *C. reinhardtii* NPQ is predicted. From Fig. 6.13, it was determined that NPQ decreases with increasing Chl *a* and Car concentration after 24 hrs of uptake. Therefore, assuming similar Chl *a* concentrations in the healthy and uranium exposed samples, the magnitude of NPQ in both EET and CT pathways may decrease. Figure 7.3(c) and (d) show transient absorption traces for healthy and uranium-exposed algae adapted from data digitized from Ref. [147]. However, it is also possible that one pathway may be preferred over the other, depending on how pigment degradation [32] or pigment-

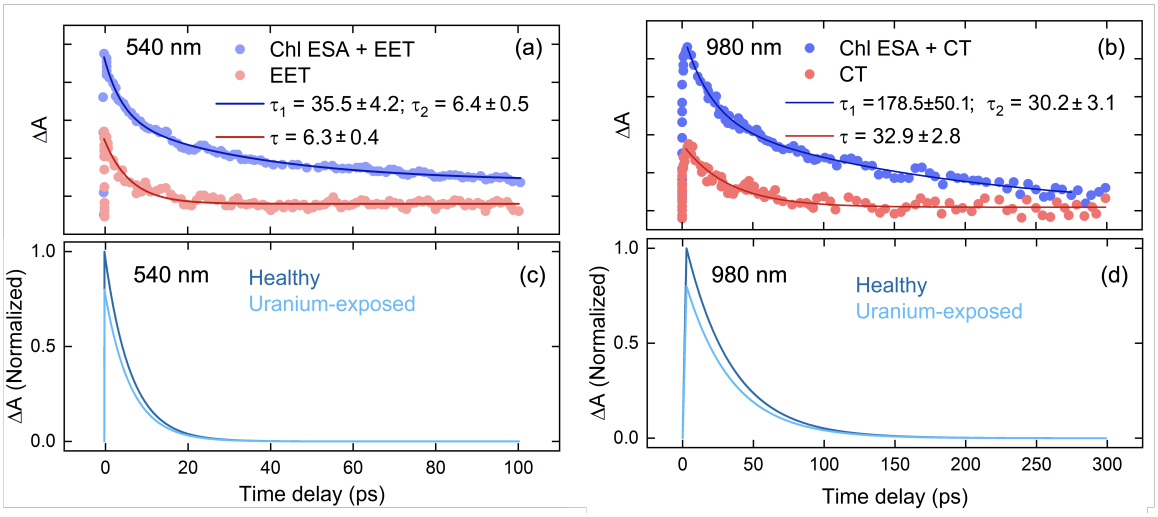

Figure 7.3: Example transient absorption traces for *N. oceanica* pumped with 665-nm light and probed at (a) 540 nm and (b) 980 nm. The data in these figures are adapted from Ref. [147], and the exponential fits were performed separately. Predicted result for unexposed and uranium-exposed algae after being pumped by 660-nm light and probed at (c) 540 nm, interrogating the EET pathway only, and (d) 980 nm for the CT pathway.

pigment separation is influenced by uranium uptake in *C. reinhardtii*. Heterodimer formation between Chl *a* and Car occurs when the two pigments are in close proximity; therefore, the decrease in [Chl]:[Car] found in Sec. 6.2 may imply a smaller gap between Chl and Car. In this case, the CT pathway may be preferred over EET. Lastly, it is possible that the rise times for both EET and CT may increase, signifying that NPQ cannot occur at the same rate as in healthy algae. One reason for these observations is the multi-functional role of carotenoids in both antioxidant properties and NPQ. As a result, many carotenoids may have oxidized through reacting with ROS to prevent damage to Chl *a*, making them less available for NPQ.

Experimental design and development has been done so far for the schematic shown in Fig. 7.2. The ΔA, which indicates EET and CT action, shows a small, around 5% change [146, 174]. A large scatter background is one of the main reasons that a signal is challenging to observe, in particular for large cells [147]. Therefore, noise and laser system fluctuations must be corrected for in order to observe the weak

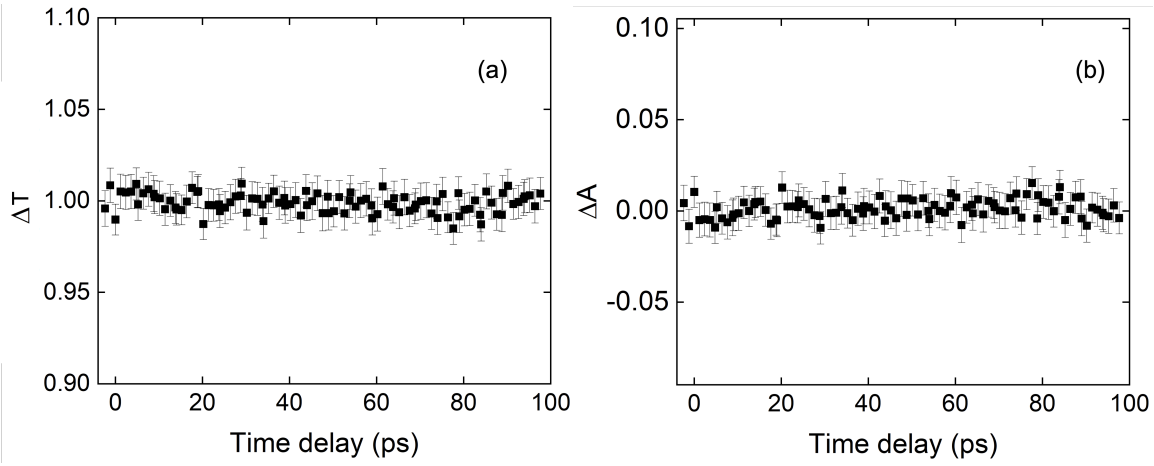

Figure 7.4: System variability for the experimental design shown in Figure 7.2, where (a) is ΔTransmittance and (b) is ΔA measured for no change in the sample. 100 waveforms are recorded twice per time step, per photodiode to simulate a scenario of no change in the system such that purely the system fluctuation can be determined.

signal. To reduce shot-to-shot fluctuations in the setup shown in Fig. 7.2, a reference photodiode is used to monitor the probe beam intensity. Furthermore, the algae cells can settle during a measurement. Therefore, a second reference measurement is made at each time step where the pump beam is blocked so as to account for changes in the signal intensity due solely to the sample concentration. The system fluctuation is characterized by blocking the pump beam during the entire measurement, and the waveforms are analyzed as if data were recorded for a real measurement. In this way, the fluctuation in the system when ΔA is expected to be 0 over the entire time delay can be determined. A total of 100 waveforms are recorded twice per time step per photodiode. The results are shown in Fig. 7.4(a) and (b), where (a) is ΔT and (b) is ΔA. The mean for ΔT and ΔA are 1.00 and 0.00, as expected. The average standard error at each time step is 0.9%. Further improvements in noise reduction can be made by recording more waveforms per time step.

7.3 Summary

Transient absorption spectroscopy can provide information on the individual NPQ pathways available to alleviate Chl *a* of excess energy. These pathways may be impacted when a plant undergoes stress and can manifest as changes in the ChlF lifetime. It is known that under drought stress and intense light exposure, the magnitude of NPQ increases to avoid photo-oxidative damage to the photosystems. The primary focus of most previous work investigating NPQ pathways has been to understand physiochemical parameters that influence the magnitude of NPQ, energy transfer dynamics, and which pigments are primarily involved [49, 146, 147, 174]. Metal stress may influence NPQ differently than natural stresses, and it is important to understand how toxic materials, like uranium, influence plants' stress remediation processes. A transient absorption spectroscopy experiment was designed and constructed. In this chapter, system characterization was performed and a $\sim$1% variability with 100 waveforms averaged per photodiode with concentration correction was determined. This variation could be further reduced with averaging more waveforms; however, it is suspected that this will be sufficient to observe a transient absorption profile in *Chlamydomonas reinhardtii*. The predicted experimental result is calculated, demonstrating a reduction in the magnitude of both NPQ pathways for uranium-exposure at 500 µM after 24 hrs with the same [Chl *a*] as the control. Further work is needed to confirm this hypothesis. The success of this work will support the identification of a unique uranium-induced response in *C. reinhardtii*, and help understand how uranium influences the alga's stress response.

CHAPTER 8

Conclusion and Future Work

8.1 Summary & Conclusion

The ability to rapidly monitor undeclared or declared nuclear activities is essential for international and domestic security and safety. Ionizing radiation methods are commonly employed in-field for nuclear material detection; however, one challenge is that they rely on signatures only from atoms which undergo nuclear decay. Furthermore, ionizing radiation is limited in the distance at which it can travel from the source, making these methods difficult to use remotely. Laser-based methods offer several benefits that can overcome these challenges. As discussed in Chapter 2, optical techniques can measure atomic, molecular, and isotopic signatures. This work applied LIBS and LIF to characterize uranium signatures both directly and indirectly through the use of biosensors. These methods combined with ultrafast laser filamentation enable remote sensing. In summary, the properties of filaments and the effects of controlling their formation conditions on the analytical capabilities were explored.

Chapter 4 examines the propagation of filaments in the multi-filament regime. In Sec. 4.1, OES is employed as a non-invasive method to investigate the excitation and relaxation dynamics in filaments formed with different driving wavelengths and peak powers. The electronic, vibrational, and rotational temperatures, electron density, and axial distribution of excited species are reported. The results from this section

can support the development of models that describe the propagation of filaments at high peak powers. In Sec. 4.2, the multi-filament structure is controlled via a GA using a deformable mirror which manipulates the spatial phase of the beam to enhance to optical emission intensity upon FIBS of metallic copper. An elliptical distribution of filaments from the application of astigmatism and enhanced characteristic signal intensity of 3× was found upon optimization. Spatial phase control with a GA can be applied without previously eliminating imperfections or aberrations from the optical system and demonstrates the potential to improve FIBS detection limits and distance over which these measurements can be conducted.

In Chapter 5, uranium atomic and molecular signatures were detected over 10 m distance using FIBS. Different external focusing conditions and the effect on the SBR of two uranium spectral signatures were explored. An unexpected result is reported, where the furthest ablation-collection scheme resulted in the highest SBR for the UO molecular signature. Furthermore, it was found that the presence of this UO feature could be identified in a $\lesssim$1 s measurement time. In previous work, it was found that the UO 593.55 nm feature is more promising for uranium isotopic measurements than atomic or ionic lines. Therefore, the results from this study further support the case for using FIBS in rapid, remote detection of uranium isotopic signatures.

While Chapter 5 focused on direct detection of uranium via FIBS, there has been recent interest in using plants' as biosensors for nuclear activity due to the sensitivity to their environment. Chapter 6 explores the feasibility of fs-LIF and F-IF to excite fluorescence of chlorophyll and identify potential signatures of uranium uptake that may different from natural stresses. In Sec. 6.1, *Arabidopsis thaliana* is hydroponically exposed to 500 µM $UO_2(NO_3)_2$, and the pigment concentrations and fluorescence lifetimes are recorded over a 5-day study. A shock response is observed for uranium followed by a recovery in the fluorescence lifetimes and pigment content. This is suspected to be a result of uranium precipitation out of solution over time,

either through phytostabilization by *A. thaliana* or water-mineral chemistry in the hydroponic solution. Sec. 6.2 explores the influence of uranium exposure on *Chlamydomonas reinhardtii* through filament-excitation of the live algae. Signs of stress were observed in the absorption spectra as both the formation of ROS and decreased [Chl]/[Car]. The potential for single-shot remote discrimination of uranium-exposed algae from the control at a distance of ∼35 m is determined from the temporal profiles of the fluorescence decay. Extrapolation of these results suggests that detection at a 125 m distance is possible within a measurement time of 1.6 s, assuming a 1-kHz laser system and a matching data acquisition system.

The increased fluorescence lifetime reported in Sec. 6.2 was found to be a promising signature for in-field detection of uranium exposure. The specific reaction to uranium uptake that causes this response is not well-understood; however, it is suspected to originate from reduced NPQ activity. Chapter 7 presents the design and construction of a transient absorption pump-probe spectroscopic system that will allow for specific NPQ pathways to be investigated. Characterization of the system was performed, and the shot-to-shot absorbance variation is found to be 1%. A predicted result is presented, where the magnitude of both excited-energy transfer and charge transfer mechanisms are reduced upon uranium exposure to *C. reinhardtii*. With the previously observed decreased [Chl]/[Car] from Sec. 6.2 compared to the control, another potential result is that the charge transfer pathway is favored upon uranium exposure, since this pathway occurs when Chl *a* and Car are within very close proximity. The results from this work would support further understanding how uranium uptake influences the optical properties of *C. reinhardtii*.

8.2 Future Work

Chapters 4 and 5 provide an investigation into filament properties and filament control for both atomic and molecular signal enhancement. In Sec. 4.2, the spatial

phase of the beam was controlled by integrating a GA and deformable mirror to increase atomic copper signal in the optical emission spectrum. While it was found that the application of astigmatism and coma to the beam lead to improved ablation efficiency, further work is needed to confirm this. One approach would be to incorporate single-shot diagnostics to image the crater produced upon ablation and record shadowgrams of the filament produced plasma during the GA optimization. Better resolution of the multi-filament structure and energy deposited to the target can be measured, respectively. By characterizing the filament structure and ablation efficiency, the processes which govern FIBS signal formation can be diagnosed. Furthermore, Chapter 5 investigated how external focusing conditions influence the SBR for the UO 593.55 nm spectral feature, and showed that 10 m ablation–collection resulted in the greatest SBR. It is determined, from the optical emission spectrum in Fig. 4.11, that the increased linewidth and intensity of ionic lines signify higher plasma density and temperature upon optimization. However, different plasma conditions may favor the formation of UO after filament ablation of uranium. By incorporating the GA for spatial phase control during filament ablation of uranium, the SBR of the UO 593.55 nm feature could be selected as the FOM. This investigation would inform on the filament-uranium target interactions and thermodynamics which lead to molecular formation in LPPs.

In Chapter 6, ultrashort pulse LIF is used to measure optical properties of plants in response to uranium exposure. Specifically in Sec. 6.2, filaments are used to excite ChlF in live algae for the first time. The pigment content, fluorescence intensity, and fluorescence lifetime provide a combination of signatures that are promising for identifying uranium exposure. In this work, a spectrophotometer was used to measure the absorption spectrum from which pigment concentration was derived. Due to the difficulty in instrumental set-up, absorption spectroscopy is more suited for lab-scale studies. Reflectance spectroscopy, on the other hand, is a commonly used in-field

method which can provide information on pigment content, as discussed in Chapter 3. One phenomenon which occurs in filamentation is spectral broadening upon filament collapse due to self-phase modulation over the propagation distance. This supercontinuum has already been shown to be useful in LIDAR applications [27, 200]; therefore, excitation of plant material with the broadened filament spectrum could allow for simultaneous measurement of pigment content and ChlF parameters. Further characterization of the relationship between the F-IF lifetime with other well-established techniques, such as PAM-F, are still needed. F-IF holds many benefits that show promise as remote, in-field environmental monitoring technique.

In this dissertation, only the influence of uranium uptake in plants has been investigated. In many scenarios where uranium is used, there may be a combination of other actinides and common industrial pollutants emitted from facilities. Therefore, the effects from a combination of metal exposures is needed to be able to (1) determine the ability to distinguish uranium from other actinides or (2) identify a signature which may be able to signify uranium uptake even in the presence of other toxic materials. Further, the focus on environmental monitoring herein has primarily been for nuclear nonproliferation purposes. The success of this work is promising for other applications, such as agricultural and pollution monitoring. Different metals have been known to cause a range of responses in plants [10, 29, 72] (see Chapter 3 for more details); therefore, it is possible that the observed F-IF parameters will be different than those reported in Sec. 6.2 for other toxic materials. For agricultural purposes, the rapid assessment of plant health is very promising for large area crop monitoring, either for determining the effectiveness of fertilizers or to assess effects of drastic climate changes during growing and harvesting seasons.

Transient absorption spectroscopy of plant photosystems can provide more information about how materials influence the specific quenching mechanisms. By identifying how various stressors specifically govern NPQ and PQ, the origin of changes

in the fluorescence lifetime can be understood. A multi-dimensional spectroscopic set-up, such as one that could scan multiple probe wavelengths, would acknowledge more NPQ and Chl de-excitation mechanisms and how they are influenced [174]. This experiment would allow for greater insight into how plants' respond to stress and how their usual responses are altered under different stress conditions.

The work presented in this dissertation shows promise for FIBS and F-IF to be used in rapid and remote environmental monitoring of nuclear activity and plant health by allowing for high spatial sensitivity and specificity. For plant health monitoring, SIF and hyperspectral imaging are the most common remote, in-field techniques. This technology is more developed than in-field use of filamentation for remote sensing, where both ground-based telescope systems and satellite systems are regularly used for SIF and hyperspectral imaging. Two drawbacks with these latter methods are the inhibition of measurement time from large solar-background and relatively poor spatial resolution. Furthermore, FIBS in direct detection of uranium holds promise over ionizing radiation methods because it is not limited in interrogation of radioactive materials. One current technological challenge for filament-supported remote sensing is the limited availability of compact, portable, and vibration-tolerant high-power ultrafast lasers. Recent advances in ultrashort Yb-doped fiber lasers may soon lead to realization of rugged and compact systems with gigawatt peak powers necessary for in-field filamentation studies [121]. Fiber-based technologies with integrated photonics promise robustness, power scalability and turn-key operation unavailable to the more common Ti:sapphire based systems. One potential method to employ fs-laser based spectroscopy in-field would be to install a fiber laser and collection system onto an unmanned areal vehicle allowing for rapid, wide-area surveillance over a $\sim$100 m range. Continued progress in source technology will improve the prospects for ultrafast laser filamentation to be employed for environmental and nuclear nonproliferation monitoring.

BIBLIOGRAPHY

BIBLIOGRAPHY

[1] SPECAIR (Version 3.0) Spectral Fitting Software, 2012.

[2] Nitrogen Dioxide Trends, United States Environmental Protection Agency, 2021.

[3] Junior-PAM chlorophyll fluorometer, Grupo EIC Iberia, 2022.

[4] U.S. Energy Information Administration. U.S. Nuclear Energy Overview, 2021.

[5] G. M. Ananyev, A.Murphy, Y. Abe, and G. C. Dismukes. Remarkable affinity and selectivity for cs+ and uranyl (uo22+) binding to the manganese site of the apo-water oxidation complex of photosystem ii. *Biochemistry*, 38(22):7200–7209, 1999.

[6] M. S. Antunes, S.-B. Ha, N. Tewari-Singh, K. J. Morey, A. M. Trofka, P. Kugrens, M. Deyholos, and J. I. Medford. A synthetic de-greening gene circuit provides a reporting system that is remotely detectable and has a re-set capacity. *Plant Biotechnology Journal*, 4(6):605–622, 2006.

[7] I. Aranjuela, F. Doustaly, J. Cela, R. Porcel, M. Müller, R. Aroca, S. Munné-Bosch, and J. Bourguignon. Glutathione and transpiration as key factors conditioning oxidative stress in arabidopsis thaliana exposed to uranium. *Planta*, 239:817–830, 2014.

[8] P. Arellano, K. Tansey, H. Balzter, and D. S. Boyd. Detecting the effects of hydrocarbon pollution in the amazon forest using hyperspectral satellite images. *Environmental Pollution*, 205:225–239, 2015.

[9] P. Atkins and J. De Paula. *Physical Chemistry Thermodynamics, Structure, and Change*. W. H. Freeman and Company, 10th edition, 2014.

[10] S.-A. Baek, T. Han, S.-K. Ahn, H. Kang, M. R. Cho, S.-C. Lee, and K.-H. Im. Effects of heavy metals on plant growths and pigment contents in arabidopsis thaliana. *The Plant Pathology Journal*, 28(4):446–452, 2012.

[11] J.E. Barefield, E.J. Judge, K.R. Campbell, J.P. Colgan, D.P. Kilcrease, H.M. Johns, R.C. Wiens, R.E. McInroy, R.K. Martinez, and S.M. Clegg. Analysis of geological materials containing uranium using laser-induced breakdown spectroscopy. *Spectrochimica Acta Part B: Atomic Spectroscopy*, 120:1 – 8, 2016.

[12] A. Becker, N. Aközbek, K. Vijayalakshmi, E. Oral, C.M. Bowden, and S.L. Chin. Intensity clamping and re-focusing of intense femtosecond laser pulses in nitrogen molecular gas. *Applied Physics B*, 73:287–290, 2001.

[13] L. Bérge. Boosted propagation of femtosecond filaments in air by double-pulse combination. *Physical Review E: Statistical, Nonlinear, & Soft Matter Physics*, 69(6):1–65601, 2004.

[14] L. Bergé and A. Couairon. Gas-induced solitons. *Phys. Rev. Lett.*, 86:1003–1006, Feb 2001.

[15] L. Bergé, S. Skupin, F. Lederer, G. Méjean, J. Yu, J. Kasparian, E. Salmon, J. P. Wolf, M. Rodriguez, L. Wöste, R. Bourayou, and R. Sauerbrey. Multiple filamentation of terawatt laser pulses in air. *Physical Review Letters*, 92:225002, 2004.

[16] J. Bernhardt, W. Liu, F. Théberge, H. L. Xu, J. F. Daigle, M. Châteauneuf, J. Dubois, and S. L. Chin. Spectroscopic analysis of femtosecond laser plasma filament in air. *Optics Communications*, 281(5):1268–1274, 2008.

[17] V. I. Bespalov and V. I. Talanov. Filamentary structure of light beams in nonlinear liquids. *JETP Lett.*, 3:307, 1966.

[18] G. A. Blackburn. Spectral indices for estimating photosynthetic pigment concentrations: A test using senescent tree leaves. *International Journal of Remote Sensing*, 19(4):657–675, 1998.

[19] A. Boghi, T. Roose, and G. J. D. Kirk. A model of uranium uptake by plant roots allowing for root-induced changes in the soil. *Environmental Science & Technology*, 52(6):3536–3545, 2018. PMID: 29466669.

[20] R. Borrego-Varillas, J. Pérez-Vizcaíno, O. Mendoza-Yero, G. Mínguez-Vega, J. R. V. de Aldana, and J. Lancis. Controlled multibeam supercontinuum generation with a spatial light modulator. *IEEE Photonics Technology Letters*, 26(16):1661–1664, 2014.

[21] S. J. Bourlat, A. Borja, J. Gilbert, M. I. Taylor, N. Davies, S. B. Weisberg, J. F. Griffith, T. Lettieri, D. Field, J. Benzie, F. O. Glöckner, N. Rodríguez-Ezpeleta, D. P. Faith, T. P. Bean, and M. Obst. Genomics in marine monitoring: New opportunities for assessing marine health status. *Marine Pollution Bulletin*, 74(1):19–31, 2013.

[22] A. Braun, G. Korn, X. Liu, D. Du, J. Squier, and G. Mourou. Self-channeling of high-peak-power femtosecond laser pulses in air. *Optics Letters*, 20(1):73–75, 1995.

[23] M. D. Brooks and K. K. Niyogi. Use of a pulse-amplitude modulated chlorophyll fluorometer to study the efficiency of photosynthesis in arabidopsis plants. In *Chloroplast Research in Arabidopsis*, pages 299–310. Springer, 2011.

[24] M. Burger, L. A. Finney, L. Garrett, S. S. Harilal, K. C. Hartig, J. Nees, P. J. Skrodzki, X. Xiao, and I. Jovanovic. Laser ablation spectrometry for studies of uranium plasmas, reactor monitoring, and spent fuel safety. *Spectrochimica Acta Part B: Atomic Spectroscopy*, 179:106095, 2021.

[25] M. Burger, P. J. Skrodzki, L. A. Finney, J. Nees, and I. Jovanovic. Remote detection of uranium using self-focusing intense femtosecond laser pulses. *Remote Sensing*, 12(8):1281, 2020.

[26] M. Burger, P. J. Skrodzki, J. Lin, J. Nees, K. Krushelnick, and I. Jovanovic. Intense laser filament-solid interactions from near-ultraviolet to mid-infrared. *Optics Express*, 26(13):16456–16465, 2018.

[27] A. V. Burnashov, A. N. Iglakova, S. F. Kovaleva, G. G. Matvienko, I. A. Medvedenko, V. K. Oshlakov, and V. I. Timofeev. Development of experimental methods of ecological monitoring using femtosecond lidar systems. In Gennadii G. Matvienko and Oleg A. Romanovskii, editors, *22nd International Symposium on Atmospheric and Ocean Optics: Atmospheric Physics*, volume 10035, pages 428 – 433. International Society for Optics and Photonics, SPIE, 2016.

[28] C. Buschmann. Variability and application of the chlorophyll fluorescence emission ratio red/far-red of leaves. *Photosynthesis Research*, 92:261–271, 2007.

[29] M. T. Cabrita, C. Gameiro, A. B. Utkin, B. Duarte, I. Cçador, and P. Cartaxana. Photosynthetic pigment laser-induced fluorescence indicators for the detection of changes associated with trace element stress in the diatom model species phaeodactylum tricornutum. *Environmental Monitoring Assessment*, 188(285):3–13, 2016.

[30] B. Campanella, S. Legnaioli, S. Pagnotta, F. Poggialini, and V. Palleschi. Shock waves in laser-induced plasmas. *Atoms*, 7(2), 2019.

[31] M. Châteauneuf, S. Payeur, J. Dubois, and J.-C. Kieffer. Microwave guiding in air by a cylindrical filament array waveguide. *Applied Physics Letters*, 92(9):091104, 2008.

[32] M. Chazaux, C. Schiphorst, G. Lazzari, and S. Caffri. Precise estimation of chlorophyll a, b and carotenoid content by deconvolution of the absorption spectrum and new simultaneous equations for chl determination. *The Plant Journal*, pages 1–19, 2021.

[33] L. Chen, C. Long, D. Wang, and J. Yang. Phytoremediation of cadmium (cd) and uranium (u) contaminated soils by brassica juncea l. enhanced with exogenous application of plant growth regulators. *Chemosphere*, 242:125112, 2020.

[34] S. Chen, X.-L. Liu, X. Lu, J. Ma, J. Wang, B. Zhu, L. Chen, and Y. Li. Temporal evolution of femtosecond laser filament detected via magnetic field around plasma current. *Opt. Express*, 25(26):32514–32521, Dec 2017.

[35] Y.-E. Chen, S. Yuan, and W. P. Schröder. Comparison of methods for extracting thylakoid membranes of arabidopsis plants. *Physiologia Plantarum*, 156(1):3–12, 2016.

[36] B. N. Chichkov, C. Momma, S. Nolte, F. Von Alvensleben, and A. Tunnermann. Femtosecond, picosecond and nanosecond laser ablation of solids. *Applied Physics A: Materials Science & Processing*, 63(2):109–115, 1996.

[37] S. L. Chin. *Femtosecond Laser Filamentation*, volume 55. Springer, 2009.

[38] R. C. Chinni, D. A. Cremers, L. J. Radziemski, M. Bostian, and C. Navarro-Northrup. Detection of uranium using laser-induced breakdown spectroscopy. *Applied Spectroscopy*, 63(11):1238–1250, 2009.

[39] I. Choi, G.C.-Y. Chan, X. Mao, D.L. Perry, and R.E. Russo. Line selection and parameter optimization for trace analysis of uranium in glass matrices by laser-induced breakdown spectroscopy (libs). *Appl. Spectrosc.*, 67(11):1275–1284, Nov 2013.

[40] Ma. Clerici, Y. Hu, P. Lassonde, C. Milián, A. Couairon, D. N. Christodoulides, Z. Chen, L. Razzari, F. Vidal, F. Légaré, D. Faccio, and R. Morandotti. Laser-assisted guiding of electric discharges around objects. *Science Advances*, 1(5), 2015.

[41] K. Cook, A. K. Kar, and R. A. Lamb. White-light filaments induced by diffraction effects. *Optics Express*, 13:2025–2031, March 2005.

[42] G. Cristoforetti, A. De Giacomo, M. Dell'Aglio, S. Legnaioli, E. Tognoni, V. Palleschi, and N. Omenetto. Local thermodynamic equilibrium in laser-induced breakdown spectroscopy: Beyond the mcwhirter criterion. *Spectrochimica Acta Part B: Atomic Spectroscopy*, 65(1):86–95, 2010.

[43] L.A. Currie. Limits for qualitative detection and quantitative determination. application to radiochemistry. *Analytical Chemistry*, 40:586–593, 1968.

[44] P. Cvjetko, M. Zovko, and B. Balen. Proteomics of heavy metal toxicity in plants. *Archives of Industrial Hygiene and Toxicology*, 65:1–18, 2014.

[45] J.-F Daigle, A Jaroń-Becker, S Hosseini, T.-J Wang, Y Kamali, G Roy, A Becker, and S. L Chin. Intensity clamping measurement of laser filaments in air at 400 and 800 nm. *Physical Review A: Atomic, Molecular, & Optical Physics*, 82(2), 2010.

[46] J.-F. Daigle, Y. Kamali, M. Châteauneuf, G. Tremblay, F. Théberge, J. Dubois, G. Roy, and S. L. Chin. Remote sensing with intense filaments enhanced by adaptive optics. *Applied Physics B: Lasers & Optics*, 97(3):701–713, 2009.

[47] J.-F. Daigle, G. Méjean, W. Liu, F. Théberge, H. L. Xu, Y. Kamali, J. Bernhardt, A. Azarm, Q. Sun, P. Mathieu, G. Roy, J.-R. Simard, and S. L. Chin. Long range trace detection in aqueous aerosol using remote filament-induced breakdown spectroscopy. *Applied Physics B: Lasers & Optics*, 87:749–754, 2007.

[48] J. Davis, J. Browne, P. Lewis, C. Pura, A. Sessoms, T. Shea, F. Slakely, B. Tannenbaum, J. Tape, J. Taylor, and P.D. Zimmerman. Tehnical steps to support nuclear arsenal downsizing. Technical report, American Physical Society, 2010.

[49] G. de la Cruz Valbuena, F.V.A. Camargo, R. Borrego-Varillas, F. Perozeni, C. D'Andrea, M. Ballottari, and G. Cerullo. Molecular mechanisms of nonphotochemical quenching in the lhcsr3 protein of chlamydomonas reinhardtii. *Journal of Physical Chemistry Letters*, 10(10):2500–2505, 2019.

[50] A. A. Dergachev, A. A. Ionin, V. P. Kandidov, D. V. Mokrousova, L. V. Seleznev, D. V. Sinitsyn, E. S. Sunchugasheva, S. A. Shlenov, and A. P. Shustikova. Plasma channels during filamentation of a femtosecond laser pulse with wavefront astigmatism in air. *Quantum Electronics*, 44(12):1085–1090, dec 2014.

[51] D. Ding, Z. Zhang, Z. Lei, Y. Yang, and T. Cai. Remediation of radiocesium-contaminated liquid waste, soil, and ash: a mini review since the fukushima daiichi nuclear power plant accident. *Environmental Science and Pollution Research*, 23:2249–2263, 2016.

[52] S. D. Ebbs, D. J. Brady, and L. V. Kochian. Role of uranium speciation in the uptake and translocation of uranium by plants. *Journal of Experimental Botany*, 49(324):1183–1190, 07 1998.

[53] A. C. Englesbe, Z. He, J. A. Nees, A. G. R. Thomas, A. Schmitt-Sody, and K. Krushelnick. Control of the configuration of multiple femtosecond filaments in air by adaptive wavefront manipulation. *Optics Express*, 24(6):6071–6082, 2016.

[54] D. Faccio, A. Lotti, A. Matijosius, F. Bragheri, V. Degiorgio, A. Couairon, and P. Di Trapani. Experimental energy-density flux characterization of ultrashort laser pulse filaments. *Optics Express*, 17(10):8193–8200, 2009.

[55] Z. Farooq, D. A. Chestakov, B. Yan, G. C. Groenenboom, W. J. van der Zande, and D. H. Parker. Photodissociation of singlet oxygen in the UV region. *Physical Chemistry Chemical Physics*, 16(7):3305–3316, 2014.

[56] G. Fibich, S. Eisenmann, B. Ilan, and A. Zigler. Control of multiple filamentation in air. *Opt. Lett.*, 29(15):1772–1774, Aug 2004.

[57] M. S. Finko and D. Curreli. Simulation of uranium plasma plume dynamics in atmospheric oxygen produced via femtosecond laser ablation. *Physics of Plasmas*, 25(8):083112, 2018.

[58] M. S. Finko, D. Curreli, D. G. Weisz, J. C. Crowhurst, T. P. Rose, B. Koroglu, H. B. Radousky, and M. R. Armstrong. A model of early formation of uranium molecular oxides in laser-ablated plasmas. *Journal of Physics D: Applied Physics*, 50(48):485201, 2017.

[59] L. A. Finney, J. Lin, P. J. Skrodzki, M. Burger, J. Nees, K. Krushelnick, and I. Jovanovic. Adaptive wavefront manipulation for remote detection via filamentation. In *2020 Conference on Lasers and Electro-Optics (CLEO)*, pages 1–2, 2020.

[60] L. A. Finney, J. Lin, P. J. Skrodzki, M. Burger, J. Nees, K. Krushelnick, and I. Jovanovic. Filament-induced breakdown spectroscopy signal enhancement using optical wavefront control. *Optics Communications*, 490:126902, 2021.

[61] L. A. Finney, N. Peskosky, P. J. Skrodzki, M. Burger, K. Krushelnick, and I. Jovanovic. Identification of Stress in Plants via Femtosecond Laser-Induced Fluorescence and Steady-State Absorption Spectroscopy. In *2021 Institute for Nuclear Materials Managements Joint Meeting & European Safeguards Research and Development Association*, pages 1 – 8. Institute for Nuclear Materials Managements, 2021.

[62] L. A. Finney, P. J. Skrodzki, M. Burger, J. Nees, S. S. Harilal, and I. Jovanovic. Single-shot, multi-signature remote detection of uranium by filament-induced breakdown spectroscopy. *Optics Letters*, 44(11):2783–2786, 2019.

[63] L. A. Finney, P. J. Skrodzki, M. Burger, J. Nees, and I. Jovanovic. Remote detection of uranium with filament ablation spectroscopy. In *2019 Conference on Lasers and Electro-Optics (CLEO)*, pages 1–2, 2019.

[64] L. A. Finney, P. J. Skrodzki, M. Burger, X. Xiao, J. Nees, and I. Jovanovic. Optical emission from ultrafast laser filament-produced air plasmas in the multiple filament regime. *Optics Express*, 26(22):29110–29122, 2018.

[65] C. Fortin, F. H. Denison, and J. Garnier-Laplace. Metal-phytoplankton interactions: Modeling the effect of competing ions (h+, ca2+, and mg2+) on uranium uptake. *Environmental Toxicology and Chemistry*, 26(2):242–248, 2009.

[66] N. M. Franklin, J. L. Stauber, S. J. Markich, and R. P. Lim. ph-dependent toxicity of copper and uranium to a tropical freshwater alga (chlorella sp.). *Aquatic Toxicology*, 48(2):275–289, 2000.

[67] C. Gameiro, A.B. Utkin, P. Cartaxana, J. Marques da Silva, and A.R. Matos. The use of laser induced chlorophyll fluorescence (lif) as a fast and non-destructive method to investigate water deficit in arabidopsis. *Agricultural Water Management*, 164:127–136, 2016. Enhancing plant water use efficiency to meet future food production.

[68] C. García-Balboa, B. Baselga-Cervera, A. García-Sanchez, J.M. Igual, V. Lopez-Rodas, and E. Costas. Rapid adaptation of microalgae to bodies of water with extreme pollution from uranium mining: An explanation of how mesophilic organisms can rapidly colonise extremely toxic environments. *Aquatic Toxicology*, 144-145:116–123, 2013.

[69] C. Gerlein-Safdi, G. Keppel-Aleks, F. Wang, S. Frolking, and D.L. Mauzerall. Satellite monitoring of natural reforestation efforts in china's drylands. *One Earth*, 2(1):98–108, 2020.

[70] I. Ghebregziabher, K. C. Hartig, and I. Jovanovic. Propagation distance-resolved characteristics of filament-induced copper plasma. *Optics Express*, 24(5):5263–5276, 2016.

[71] A. Gitelson and A. Solovchenko. Non-invasive quantification of foliar pigments: Possibilities and limitations of reflectance- and absorbance-based approaches. *Journal of Photochemistry and Photobiology B: Biology*, 178:537–544, 2018.

[72] R. Gopal, K.B. Mishra, M. Zeeshan, S.M. Prasad, and M.M. Joshi. Laser-induced chlorophyll fluorescence spectra of mung plants growing under nickel stress. *Current Science*, 83(7):880–884, 2002.

[73] M. Govender, H. Bulcock, and K. T. Chetty. A review of hyperspectral remote sensing and its application in vegetation and water resource studies. *Water SA*, 33(2):145–151, 2007.

[74] J. W. Grantham, H. M. Gibbs, G. Khitrova, J. F. Valley, and Xu Jiajin. Kaleidoscopic spatial instability: Bifurcations of optical transverse solitary waves. *Phys. Rev. Lett.*, 66:1422–1425, Mar 1991.

[75] H. R. Griem. *Plasma Spectroscopy*. Academic Press, 1964.

[76] H. R. Griem. *Spectral Line Broadening by Plasmas*. Academic Press, 1974.

[77] K. Grossmann, C. Frankenberg, T.S. Magney, S.C. Hurlock, U. Seibt, and J. Stutz. Photospec: A new instrument to measure spatially distributed red and far-red solar-induced chlorophyll fluorescence. *Remote Sensing of Environment*, 216:311–327, 2018.

[78] R. I. Grynko, D. L. Weerawarne, X. Gao, H. Liang, H. J. Meyer, K.-H. Hong, A. L. Gaeta, and B. Shim. Inhibition of multi-filamentation of high-power laser beams. *Opt. Lett.*, 41(17):4064–4067, Sep 2016.

[79] S. S. Harilal, C. V. Bindhu, M. S. Tillack, F. Najmabadi, and A. C. Gaeris. Plume splitting and sharpening in laser-produced aluminium plasma. *Journal of Physics D: Applied Physics*, 35(22):2935, 2002.

[80] S. S. Harilal, C. V. Bindhu, M. S. Tillack, F. Najmabadi, and A. C. Gaeris. Internal structure and expansion dynamics of laser ablation plumes into ambient gases. *Journal of Applied Physics*, 93(5):2380–2388, 2003.

[81] S. S. Harilal, B. E. Brumfield, N. L. LaHaye, K. C. Hartig, and M. C. Phillips. Optical spectroscopy of laser-produced plasmas for standoff isotopic analysis. *Applied Physics Reviews*, 5:021301, 2018.

[82] S. S. Harilal, J. R. Freeman, P. K. Diwakar, and A. Hassanein. *Femtosecond Laser Ablation: Fundamentals and Applications*, pages 143–166. Springer Berlin Heidelberg, Berlin, Heidelberg, 2014.

[83] S. S. Harilal, E. J. Kautz, B. E. Bernacki, M. C. Phillips, P. J. Skrodzki, M. Burger, and I. Jovanovic. Physical conditions for UO formation in laser-produced uranium plumes. *Physical Chemistry Chemical Physics*, 21(29):16161–16169, 2019.

[84] S. S. Harilal, J. Yeak, B. E. Brumfield, and M. C. Phillips. Consequences of femtosecond laser filament generation conditions in standoff laser induced breakdown spectroscopy. *Optics Express*, 24(16):17941–17949, 2016.

[85] S.S. Harilal, B.E. Brumfield, N. Glumac, and M.C. Phillips. Elucidating uranium monoxide spectral features from a laser-produced plasma. *Opt. Express*, 26(16):20319–20330, Aug 2018.

[86] K. C. Hartig, I. Ghebregziabher, and I. Jovanovic. Standoff detection of uranium and its isotopes by femtosecond filament laser ablation molecular isotopic spectrometry. *Scientific Reports*, 7(1):43852, 2017.

[87] K. C. Hartig, S. S. Harilal, M. C. Phillips, B. E. Brumfield, and I. Jovanovic. Evolution of uranium monoxide in femtosecond laser-induced uranium plasmas. *Optics Express*, 25(10):11477–11490, 2017.

[88] C.P. Hauri, J. Gautier, A. Trisorio, E. Papalazarou, and P. Zeitoun. Two-dimensional organization of a large number of stationary optical filaments by adaptive wave front control. *Applied Physics B*, 90(3):391–394, Mar 2008.

[89] E. E. Hayek, C. Torres, L. Rodriguez-Freire, J. M. Blake, C. L. De Vore, A. J. Brearley, M. N. Spilde, S. Cabaniss, A.-M. S. Ali, , and J. M. Cerrato. Effect of calcium on the bioavailability of dissolved uranium (vi) in plant roots under circumneutral ph. *Environmental Science and Technology*, 52(22):13089–13098, 2018.

[90] G. Heck, J. Sloss, and R.J. Levis. Adaptive control of the spatial position of white light filaments in an aqueous solution. *Optics Communications*, 259(1):216 – 222, 2006.

[91] S. Henin, Y. Petit, J. Kasparian, J.-P. Wolf, A. Jochmann, S. D. Kraft, S. Bock, U. Schramm, R. Sauerbrey, and W. M. Nakaema. Saturation of the filament density of ultrashort intense laser pulses in air. *Applied Physics B: Lasers & Optics*, 100(1):77–84, 2010.

[92] O. Herlory, J.-M. Bonzom, and R. Gilbin. Sensitivity evaluation of the green alga chlamydomonas reinhardtii to uranium by pulse amplitude modulated (pam) fluorometry. *Aquatic Toxicology*, 140-141:288–294, 2013.

[93] K.F. Herzfeld. The rate and mechanism of the thermal dissociation of oxygen. *Symposium (International) on Combustion*, 7(1):27–33, 1958.

[94] D. R. Hoagland and D. I. Arnon. Composition of nutrient solutions. In *The Water-Culture Method for Growing Plants Without Soil*, pages 23–24. Berkeley, Calif.: College of Agriculture, University of California, 1938.

[95] A.R. Holzwarth, M.G. Müller, J. Niklas, and W. Lubitz. Charge recombination fluorescence in photosystem i reaction centers from chlamydomonas reinhardtii. *Journal of Physical Chemistry B*, 109(12):5903–5911, 2005.

[96] A.R. Holzwarth, M.G. Müller, J. Niklas, and W. Lubitz. Ultrafast transient absorption studies on photosystem i reaction centers from chlamydomonas reinhardtii. 2: Mutations near the p700 reaction center chlorophylls provide new insight into the nature of the primary electron donor. *Biophysical Journal*, 90(2):552–565, 2006.

[97] H. Hou, G.C.-Y. Chan, X. Mao, R. Zheng, V. Zorba, and R.E. Russo. Femtosecond filament-laser ablation molecular isotopic spectrometry. *Spectrochimica Acta Part B: Atomic Spectroscopy*, 113:113 – 118, 2015.

[98] H. Hou, B. Yang, X. Mao, V. Zorba, P. Ran, and R. E. Russo. Characteristics of plasma plume in ultrafast laser ablation with a weakly ionized air channel. *Optics Express*, 26(10):13425–13435, 2018.

[99] A. A. Ilyin, S. S. Golik, and K. A. Shmirko. Absorption and emission characteristics of femtosecond laser plasma filaments in the air. *Spectrochimica Acta Part B: Atomic Spectroscopy*, 112:16–22, 2015.

[100] A. A. Ionin, N. G. Iroshnikov, O. G. Kosareva, A. V. Larichev, D. V. Mokrousova, N. A. Panov, L. V. Seleznev, D. V. Sinitsyn, and E. S. Sunchugasheva. Filamentation of femtosecond laser pulses governed by variable wavefront distortions via a deformable mirror. *J. Opt. Soc. Am. B*, 30(8):2257–2262, Aug 2013.

[101] A. Iriel, G. Dundas, A. Fernández Cirelli, and M. G. Lagorio. Effect of arsenic on reflectance spectra and chlorophyll fluorescence of aquatic plants. *Chemosphere*, 119:697–703, 2015.

[102] J. D. Jackson. *Classical Electrodynamics*. John Wiley & Sons, 3rd edition, 1999.

[103] N. Jhajj, J. K. Wahlstrand, and H. M. Milchberg. Optical mode structure of the air waveguide. *Optics Letters*, 39(21):6312–6315, 2014.

[104] A. J. Jinia, T. E. Maurer, C. A. Meert, M. Y. Hua, S. D. Clarke, H.-S. Kim, D. D. Wentzloff, and S. A. Pozzi. An artificial neural network system for photon-based active interrogation applications. *IEEE Access*, 9:119871–119880, 2021.

[105] I. Jovanovic and A. S. Erickson. *Active Interrogation in Nuclear Security*. Springer, Cham, 1st edition, 2018.

[106] V.P. Kandidov, N. Akozbek, M. Scalora, O.G. Kosareva, A.V. Nyakk, Q. Luo, S.A. Hosseini, and S.L. Chin. Towards a control of multiple filamentation by spatial regularization of a high-power femtosecond laser pulse. *Applied Physics B*, 80(2):267–275, Feb 2005.

[107] S. Kaur and S. J. S. Flora. Quenching action of monofunctional sulfur mustard on chlorophyll fluorescence: Towards an ultrasensitive biosensor. *Applied Biochemistry and Biotechnology*, 171:1405–1415, 2013.

[108] E. J. Kautz, P. J. Skrodzki, M. Burger, B. E. Bernacki, I. Jovanovic, M. C. Phillips, and S. S. Harilal. Time-resolved imaging of atoms and molecules in laser-produced uranium plasmas. *Journal of Analytical Atomic Spectrometry*, 34(11):2236–2243, 2019.

[109] R. S. Kemp. Initial analysis of the detectability of UO_2F_2 aerosols produced by UF_6 released from uranium conversion plants. *Science & Global Security*, 16(3):115–125, 2008.

[110] K. Klubicová, M. Danchenko, L. Skultety, V. V. Berezhna, A. Hricová, N. M. Rashydov, and M. Hajduch. Agricultural recovery of a formerly radioactive area: Ii. systematic proteomic characterization of flax seed development in the remediated chernobyl area. *Journal of Proteomics*, 74(8):1378–1384, 2011. Plant Proteomics in Europe.

[111] G. F. Knoll. *Radiation Detection and Measurement*. John Wiley & Sons, 3rd edition, 2000.

[112] O.G. Kosareva, N.A. Panov, N. Akozbek, V.P. Kandidov, Q. Luo, S.A. Hosseini, W. Liu, J.-F. Gravel, G. Roy, and S.L. Chin. Controlling a bunch of multiple filaments by means of a beam diameter. *Applied Physics B*, 82(1):111–122, Jan 2006.

[113] A. Kramida, Y. Ralchenko, and J. Reader. National Institute of Standards and Technology (NIST) Atomic Spectra Database, 2018.

[114] J. Kromdijk, K. Głowacka, L. Leonelli, S. T. Gabilly, M. Iwai, K. K. Niyogi, and S. P. Long. Improving photosynthesis and crop productivity by accelerating recovery from photoprotection. *Science*, 354(6314):857–861, 2016.

[115] D. LaGraffe. *Nuclear Security Science*, pages 1–34. Springer, 2018.

[116] O. Lahav, L. Levi, I. Orr, R. A. Nemirovsky, J. Nemirovsky, I. Kaminer, M. Segev, and O. Cohen. Long-lived waveguides and sound-wave generation by laser filamentation. *Physical Review A: Atomic, Molecular, & Optical Physics*, 90:021801, 2014.

[117] J. R. Lamarsh and A. J. Baratta. *Introduction to Nuclear Engineering*. U.S.A:Prentice Hall, 3rd edition, 2001.

[118] J. J. Laserna, R. Fernández Reyes, R. González, L. Tobaria, and P. Lucena. Study on the effect of beam propagation through atmospheric turbulence on standoff nanosecond laser induced breakdown spectroscopy measurements. *Optics Express*, 17(12):10265–10276, 2009.

[119] N. Lemos, L. Cardoso, J. Geada, F. Albert G. Figueira, and J. M. Dias. Guiding of laser pulses in plasma waveguides created by linearly-polarized femtosecond laser pulses. *Scientific Reports*, 8(3165):1–9, 2018.

[120] H. K. Lichtenthaler. [34] chlorophylls and carotenoids: Pigments of photosynthetic biomembranes. In *Plant Cell Membranes*, volume 148 of *Methods in Enzymology*, pages 350–382. Academic Press, 1987.

[121] J. Limpert, F. Roser, T. Schreiber, and A. Tunnermann. High-power ultrafast fiber laser systems. *IEEE Journal of Selected Topics in Quantum Electronics*, 12(2):233–244, 2006.

[122] L. Liu, Yo. Zhang, J. Wang, and C. Zhao. Detecting solar-induced chlorophyll fluorescence from field radiance spectra based on the fraunhofer line principle. *IEEE Transactions on Geoscience and Remote Sensing*, 43(4):827–832, 2005.

[123] W. Liu, J. Bernhardt, F. Théberge, S. L. Chin, M. Châteauneuf, and J. Dubois. Spectroscopic characterization of femtosecond laser filament in argon gas. *Journal of Applied Physics*, 102(3):033111, 2007.

[124] W. Liu, J.-F. Gravel, F. Théberge, A. Becker, and S. L. Chin. Background reservoir: Its crucial role for long-distance propagation of femtosecond laser pulses in air. *Applied Physics B: Lasers & Optics*, 80(7):857–860, 2005.

[125] W. Liu, F. Théberge, E. Arevalo, J.-F. Gravel, A. Becker, and S. L. Chin. Experiment and simulations on the energy reservoir effect in femtosecond light filaments. *Optics Letters*, 30(19):2602–2604, 2005.

[126] W. Liu, F. Théberge, J.-F. Daigle, P. T. Simard, S. M. Sarifi, Y. Kamali, H. L. Xu, and S. L. Chin. An efficient control of ultrashort laser filament location in air for the purpose of remote sensing. *Applied Physics B*, 85:55–58, 2006.

[127] W. Liu, H. L. Xu, G. Méjean, Y. Kamali, J.-F. Daigle, A. Azarm, P. T. Simard, P. Mathieu, G. Roy, and S. L. Chin. Efficient non-gated remote filament-induced breakdown spectroscopy of metallic sample. *Spectrochimica Acta Part B: Atomic Spectroscopy*, 62(1):76–81, 2007.

[128] X.-L. Liu, W. Cheng, M. Petrarca, and P. Polynkin. Measurements of fluence profiles in femtosecond laser filaments in air. *Optics Letters*, 41(20):4751–4754, 2016.

[129] Q. Luo, W. Liu, and S. L. Chin. Lasing action in air induced by ultra-fast laser filamentation. *Applied Physics B: Lasers & Optics*, 76(3):337–340, 2003.

[130] P. Maioli, R. Salamé, N. Lascoux, E. Salmon, P. Béjot, J. Kasparian, and J.-P. Wolf. Ultraviolet-visible conical emission by multiple laser filaments. *Optics Express*, 17(6):4726–4731, 2009.

[131] W. Maksymiec, M. Wójcik, and Z. Krupa. Variation in oxidative stress and photochemical activity in arabidopsis thaliana leaves subjected to cadmium and excess copper in the presence or absence of jasmonate and ascorbate. *Chemosphere*, 66(3):421–427, 2007.

[132] X. Mao, G.C.-Y. Chan, I. Choi, V. Zorba, and R.E. Russo. Combination of atomic lines and molecular bands for uranium optical isotopic analysis in laser induced plasma spectrometry. *Journal of Radioanalytical and Nuclear Chemistry*, 312(1):121–131, Apr 2017.

[133] R. W. P. McWhirter. *Plasma Diagnostic Techniques*. Academic Press, 1965.

[134] S. Mihai, A. Marcu, and N. N. Puscas. *Pulsed Laser Ablation of Solids: Basics, Theory, and Applications*, volume 53. Springer, 2013.

[135] A. V. Mitrofanov, A. A. Voronin, D. A. Sidorov-Biryukov, A. Pugžlys, E. A. Stepanov, G. Andriukaitis, T. Flöry, S. Ali{vsauskas, A. B. Fedotov, and A. Baltu{vska. Mid-infrared laser filaments in the atmosphere. *Scientific Reports*, 5(1):8368, 2015.

[136] M. Mlejnek, M. Kolesik, J. V. Moloney, and E. M. Wright. Optically turbulent femtosecond light guide in air. *Phys. Rev. Lett.*, 83:2938–2941, Oct 1999.

[137] G. H. Mohammed, R. Colombo, E. M. Middleton, U. Rascher, C. van der Tol, L. Nedbal, Y. Goulas, O. Pérez-Priego, A. Damm, M. Meroni, J. Joiner, S. Cogliati, W. Verhoef, Z. Malenovský, J.-P. Gastellu-Etchegorry, J. R. Miller,

L. Guanter, J. Moreno, I. Moya, J. A. Berry, C. Frankenberg, and P. J. Zarco-Tejada. Remote sensing of solar-induced chlorophyll fluorescence (sif) in vegetation: 50 years of progress. *Remote Sensing of Environment*, 231:111177, 2019.

[138] E.H. Murchie and T. Lawson. Chlorophyll fluorescence analysis: a guide to good practice and understanding some new applications. *Journal of Experimental Botany*, 64(13):3983–3998, 08 2013.

[139] M.G. Müller, J. Niklas, W. Lubitz, and A.R. Holzwarth. Ultrafast transient absorption studies on photosystem i reaction centers from chlamydomonas reinhardtii. 1. a new interpretation of the energy trapping and early electron transfer steps in photosystem i. *Biophysical Journal*, 85(6):3899–3922, 2003.

[140] M. B. D. Nikitin, A. Andrews, and M. Holt. *Managing the Nuclear Fuel Cycle: Policy Implications of Expanding Global Access to Nuclear Power*. Library of Congress: Congressional Research Service. Diane Publishing [for the Congressional Research Service], 2010.

[141] S. P. O'Connor, C. B. Marble, D. T. Nodurft, G. D. Noojin, A. R. Boretsky, A. W. Wharmby, M. O. Scully, and V. V. Yakovlev. Filamentation in atmospheric air with tunable 1100–2400 nm near-infrared femtosecond laser source. *Scientific Reports*, 9(12049):1–7, 2019.

[142] OKO Technologies. Frontsurfer wavefront analysis and control system, May 2011.

[143] J. Orphal and K. Chance. Ultraviolet and visible absorption cross-sections for hitran. *Journal of Quantitative spectroscopy and Radiative Transfer*, 82:491–504, 2003.

[144] B. A. Palmer, R. A. Keller, and R. Engleman. Report No. LA 8251-MS: An atlas of uranium emission intensities in a hollow cathode discharge. Technical report, Los Alamos National Laboratory, 1980.

[145] J. Papeer, R. Bruch, E. Dekel, O. Pollak, M. Botton, Z. Henis, and A. Zigler. Generation of concatenated long high-density plasma channels in air by a single femtosecond laser pulse. *Applied Physics Letters*, 107(12):124102, 2015.

[146] S. Park, A.L. Fischer, C.. Steen, M.Iwai, J.M. Morris, P.J. Walla, K.K. Niyogi, and G.R. Fleming. Charge recombination fluorescence in photosystem i reaction centers from chlamydomonas reinhardtii. *Journal of the American Chemical Society*, 140(38):11965–11973, 2018.

[147] S. Park, C. J. Steen, D. Lyska, A. L. Fischer, B. Endelman, M. Iwai, K. K. Niyogi, and G. R. Fleming. Chlorophyll–carotenoid excitation energy transfer and charge transfer in nannochloropsis oceanica for the regulation of photosynthesis. *Proceedings of the National Academy of Sciences*, 116(9):3385–3390, 2019.

[148] W. Pietsch, A. Petit, and A. Briand. Isotope ratio determination of uranium by optical emission spectroscopy on a laser-produced plasma - basic investigations and analytical results. *Spectrochimica Acta Part B: Atomic Spectroscopy*, 53(5):751–761, 1998.

[149] G. Point, Y. Brelet, A. Houard, V. Jukna, C. Milián, J. Carbonnel, Y. Liu, A. Couairon, and A. Mysyrowicz. Superfilamentation in air. *Phys. Rev. Lett.*, 112:223902, Jun 2014.

[150] P. Polynkin and Y. Cheng. *Air Lasing*. Springer, 2017.

[151] R.J. Porra, W.A. Thompson, and P.E. Kriedemann. Determination of accurate extinction coefficients and simultaneous equations for assaying chlorophylls a and b extracted with four different solvents: verification of the concentration of chlorophyll standards by atomic absorption spectroscopy. *Biochimica et Biophysica Acta (BBA) - Bioenergetics*, 975(3):384–394, 1989.

[152] F. V. Potemkin, E. I. Mareev, A. A. Podshivalov, and V. M. Gordienko. Highly extended high density filaments in tight focusing geometry in water: from femtoseconds to microseconds. *New Journal of Physics*, 17(5):053010, may 2015.

[153] C.A. Raines. The calvin cycle revisited. *Photosynthesis Research*, 75:1–10, 2003.

[154] M. Rodriguez, R. Bourayou, G. Méjean, J. Kasparian, J. Yu, E. Salmon, A. Scholz, B. Stecklum, J. Eislöffel, U. Laux, A. P. Hatzes, R. Sauerbrey, L. Wöste, and J.-P. Wolf. Kilometer-range nonlinear propagation of femtosecond laser pulses. *Physical Review E: Statistical, Nonlinear, Biological, & Soft Matter Physics*, 69:036607, 2004.

[155] P. Rohwetter, K. Stelmaszczyk, L. Wöste, R. Ackermann, G. Méjean, E. Salmon, J. Kasparian, J. Yu, and J.-P. Wolf. Filament-induced remote surface ablation for long range laser-induced breakdown spectroscopy operation. *Spectrochimica Acta Part B: Atomic Spectroscopy*, 60(7):1025–1033, 2005.

[156] Ph. Rohwetter, K. Stelmaszczyk, L. Wöste, R. Ackermann, G. Méjean, E. Salmon, J. Kasparian, J. Yu, and J.-P. Wolf. Filament-induced remote surface ablation for long range laser-induced breakdown spectroscopy operation. *Spectrochimica Acta Part B: Atomic Spectroscopy*, 60(7):1025 – 1033, 2005. Laser Induced Plasma Spectroscopy and Applications (LIBS 2004) Third International Conference.

[157] A. Rosema, J.F.H. Snel, H. Zahn, W.F. Buurmeijer, and L.W.A. Van Hove. The relation between laser-induced chlorophyll fluorescence and photosynthesis. *Remote Sensing of Environment*, 65(2):143–154, 1998.

[158] E. W. Rosenthal, N. Jhajj, J. K. Wahlstrand, and H. M. Milchberg. Collection of remote optical signals by air waveguides. *Optica*, 1(1):5–9, 2014.

[159] E. Saenen, N. Horemans, N. Vanhoudt, H. Vandenhove, G. Biermans, M. Van Hees, J. Wannijn, J. Vangronsveld, and A. Cuypers. The ph strongly influences the uranium-induced effects on the photosynthetic apparatus of arabidopsis thaliana plants. *Plant Physiology and Biochemistry*, 82:254–261, 2014.

[160] M. M. Samoza. Franck-Condon-Diagram, Wikimedia, 2006. CC BY-SA 2.5.

[161] M. M. Samoza. Vibration-Fluor-Abs, Wikimedia, 2006. CC-BY-SA 2.5.

[162] S. Sankaran, A. Mishra, R. Ehsani, and C. Davis. A review of advanced techniques for detecting plant diseases. *Computers and Electronics in Agriculture*, 72(1):1–13, 2010.

[163] L. I. Sedov. *Similarity and Dimensional Methods in Mechanics*. Academic Press, 1959.

[164] P. Sharma, A. B. Jha, R. S. Dubey, and M. Pessarakli. Reactive oxygen species, oxidative damage, and antioxidative defense mechanism in plants under stressful conditions. *Jounral of Botany*, (217037):1–26, 2012.

[165] Y. R. Shen. *The Principles of Nonlinear Optics*. John Wiley & Sons, 1st edition, 2003.

[166] Z. Shi, S.-Y. Li, H. Zhang, H. Li, A.-M. Chen, and M.-X. Jin. Formation of plasma channels in ambient air by axicon-focused femtosecond laser pulse. *Optik*, 164:590 – 595, 2018.

[167] Y. Shibata, A. Mohamed, K. Taniyama, K. Kanatani, M. Kosugi, and H. Fukumura. Red shift in the spectrum of a chlorophyll species is essential for the drought-induced dissipation of excess light energy in a poikilohydric moss, bryum argenteum. *Photosynthesis Research*, 136:229–243, 2018.

[168] P. J. Skrodzki, M. Burger, L. A. Finney, R. Nawara, J. Nees, and I. Jovanovic. Millisecond-long suppression of spectroscopic optical signals using laser filamentation. *Opt. Lett.*, 46(15):3777–3780, Aug 2021.

[169] P. J. Skrodzki, M. Burger, and I. Jovanovic. Transition of femtosecond-filament-solid interactions from single to multiple filament regime. *Scientific Reports*, 7(1):12740–8, 2017.

[170] P. J. Skrodzki, M. Burger, I. Jovanovic, M. C. Phillips, B. E. Brumfield, and S. S. Harilal. Tracking of oxide formation in laser-produced uranium plasmas. *Optics Letters*, 43(20):5118–5121, 2018.

[171] P. J. Skrodzki, M. Burger, I. Jovanovic, M. C. Phillips, J. Yeak, B. E. Brumfield, and S. S. Harilal. Plume dynamics and gas-phase molecular formation in transient laser-produced uranium plasmas. *Physics of Plasmas*, 26(8):83508, 2019.

[172] Somepics. Thylakoid membrane 3, Wikimedia, 2015. CC BY-SA 4.0.

[173] G. Spindler and G. Paunescu. Multifilamentation of femtosecond laser pulses propagating in turbulent air near the ground. *Applied Physics B*, 96:185–191, 2009.

[174] H. Staleva, J. Komenda, M.K. Shukla, V. Šlouf, R. Kaňa, T. Polívka, and R. Sobotka. Mechanism of photoprotection in the cyanobacterial ancestor of plant antenna proteins. *Nature Chemical Biology*, 11:287–291, 2015.

[175] K. Stelmaszczyk, P. Rohwetter, G. Méjean, J. Yu, E. Salmon, J. Kasparian, R. Ackermann, J.-P. Wolf, and L. Wöste. Long-distance remote laser-induced breakdown spectroscopy using filamentation in air. *Applied Physics Letters*, 85(18):3977–3979, 2004.

[176] D. Strickland and G. Mourou. Compression of amplified chirped optical pulses. *Optics Communications*, 55(6):447–449, 1985.

[177] N. Subhash, C. N. Mohanan, R. J. Mallia, and V. Muralidharan. Quantification of stress adaptation by laser-induced fluorescence spectroscopy of plants exposed to engine exhaust emission and drought. *Functional Plant Biology*, 31:709–719, 2004.

[178] Z. Sun, J. Chen, and W. Rudolph. Determination of the transient electron temperature in femtosecond laser-induced air plasmas. In *Conference on Lasers and Electro-Optics 2010*, page CTuPP5. Optical Society of America, 2010.

[179] F. Théberge, W. Liu, P. T. Simard, A. Becker, and S. L. Chin. Plasma density inside a femtosecond laser filament in air: Strong dependence on external focusing. *Physical Review E: Statistical, Nonlinear, Biological, & Soft Matter Physics*, 74:036406, 2006.

[180] D. B. Thomsom. A guide to the nuclear arms control treaties. *Tech. Rep. LA-UR-99-3173*, 1999.

[181] S. Tzortzakis, D. Anglos, and D. Gray. Ultraviolet laser filaments for remote laser-induced breakdown spectroscopy (LIBS) analysis: applications in cultural heritage monitoring. *Optics Letters*, 31(8):1139–1141, 2006.

[182] S. L. Ustin, A.A. Gitelson, S. Jacquemoud, M. Schaepman, G. P. Asner, J. A. Gamon, and P. Zarco-Tejada. Retrieval of foliar information about plant pigment systems from high resolution spectroscopy. *Remote Sensing of Environment*, 113:S67–S77, 2009. Imaging Spectroscopy Special Issue.

[183] N. Vanhoudt, A. Cuypers, N. Horemans, T. Remans, K. Opdenakker, K. Smeets, D. M. Bello, M. Havaux, J. Wannijn, M. Van Hees, J. Vangronsveld, and H. Vandenhove. Unraveling uranium induced oxidative stress related responses in arabidopsis thaliana seedlings. part ii: responses in the leaves and

general conclusions. *Journal of Environmental Radioactivity*, 102(6):638–645, 2011.

[184] N. Vanhoudt, N. Horemans, G. Biermans, E. Saenen, J. Wannijn, R. Nauts, M. Van Hees, and H. Vandenhove. Uranium affects photosynthetic parameters in arabidopsis thaliana. *Environmental and Experimental Botany*, 97:22–29, 2014.

[185] N. Vanhoudt, H. Vandenhove, K. Smeets, T. Remans, M. Van Hees, J. Wannijn, J. Vangronsveld, and A. Cuypers. Effects of uranium and phosphate concentrations on oxidative stress related responses induced in arabidopsis thaliana. *Plant Physiology and Biochemistry*, 46(11):987–996, 2008.

[186] J. Wang, J. Sun, Y. Song, Y.and Xu, X. Pan, Y. Sun, and D. Li. A label-free microfluidic biosensor for activity detection of single microalgae cells based on chlorophyll fluorescence. *Sensors*, 13(12):16075–16089, 2013.

[187] T.-J. Wang, J. Ju, Y. Wei, R. Li, Z. Xu, and S. L. Chin. Longitudinally resolved measurement of plasma density along femtosecond laser filament via terahertz spectroscopy. *Applied Physics Letters*, 105(5):051101, 2014.

[188] Y Wang, L Xu, Y Chen, H Shen, Y Gong, C Limera, and L Liu. Transcriptome profiling of radish (raphanus sativus l.) root and identification of genes involved in response to lead (pb) stress with next generation sequencing. *PLOS ONE*, 8(6):e66539, 2013.

[189] Z. Wang, G. Li, H. Sun, L. Ma, Y. Guo, Z. Zhao, H. Gao, and L. Mei. Effects of drought stress on photosynthesis and photosynthetic electron transport chain in young apple tree leaves. *Biology Open*, 7(11):1–9, 2018.

[190] E. N. Weerakkody and N. G. Glumac. Quantitative absorption spectroscopy of laser-produced plasmas. *Journal of Physics D: Applied Physics*, 54(12), 2021.

[191] E. N. Weerakkody, D. G. Weisz, J. Crowhurst, B. Koroglu, T. Rose, H. Radousky, R. L. Stillwell, J. R. Jeffries, and N. G. Glumac. Time-resolved formation of uranium and silicon oxides subsequent to the laser ablation of U_3Si_2. *Spectrochimica Acta Part B: Atomic Spectroscopy*, 170:105925, 2020.

[192] D. G. Weisz, J. C. Crowhurst, W. J. Siekhaus, T. P. Rose, B. Koroglu, H. B. Radousky, J. M. Zaug, M. R. Armstrong, B. H. Isselhardt, M. R. Savina, M. Azer, M. S. Finko, and D. Curreli. Formation of $^{238}U^{16}O$ and $^{238}U^{18}O$ observed by time-resolved emission spectroscopy subsequent to laser ablation. *Applied Physics Letters*, 111(3):034101, 2017.

[193] H. L. Xu, P. T. Simard, Y. Kamali, J.-F. Daigle, C. Marceau, J. Bernhardt, J. Dubois, M. Châteauneuf, F. Théberge, and G. Roy. Filament-induced breakdown remote spectroscopy in a polar environment. *Laser Physics*, 22(12):1767–1770, 2012.

[194] H.L. Xu, A. Azarm, J. Bernhardt, Y. Kamali, and S.L. Chin. The mechanism of nitrogen fluorescence inside a femtosecond laser filament in air. *Chemical Physics*, 360(1):171–175, 2009.

[195] H. Yamakawa, Y. Fukushima, S. Itoh, and U. Heber. Three different mechanisms of energy dissipation of a desiccation-tolerant moss serve one common purpose: to protect reaction centres against photo-oxidation*. *Journal of Experimental Botany*, 63(10):3765–3775, 03 2012.

[196] H. Yamakawa and S. Itoh. Dissipation of excess excitation energy by drought-induced nonphotochemical quenching in two species of drought-tolerant moss: Desiccation-induced acceleration of photosystem ii fluorescence decay. *Biochemistry*, 52(26):4451–4459, 2013. PMID: 23750703.

[197] T. Young. I. the bakerian lecture. experiments and calculations relative to physical optics. *Philosophical Transactions of The Royal Society*, 94:1–16, 1804.

[198] P.J Zarco-Tejada, J.C Pushnik, S Dobrowski, and S.L Ustin. Steady-state chlorophyll a fluorescence detection from canopy derivative reflectance and double-peak red-edge effects. *Remote Sensing of Environment*, 84(2):283–294, 2003.

[199] Y. B. Zeldovich and Y. P. Raizer. *Physics of Shock Waves and High-Temperature Hydrodynamic Phenomena*. Academic Press, 1966.

[200] B. Zeng, T.-J. Wang, S. Hosseini, Y. Cheng, Z. Xu, W. Liu, and S. L. Chin. Enhanced remote filament-induced breakdown spectroscopy with spatio-temporally chirped pulses. *J. Opt. Soc. Am. B*, 29(12):3226–3230, Dec 2012.

[201] T. Zeng, S. Zhu, S. Zhou, and Y. He. Spatial evolution of laser filaments in turbulent air. *Optics Communications*, 412:161–165, 2018.

[202] X. Zeng, X.L. Mao, R. Greif, and R.E. Russo. Experimental investigation of ablation efficiency and plasma expansion during femtosecond and nanosecond laser ablation of silicon. *Scientific Reports*, 80:237–241, 2005.

[203] Z. Zgorelec, N. Bilandzija, K. Knez, M. Galic, and S. Zuzul. Cadmium and mercury phytostabilization from soil using miscanthus × giganteus. *Scientific Reports*, 10(6685), 2020.

[204] L. Zhang, N. Qiao, C. Huang, and S. Wang. Monitoring drought effects on vegetation productivity using satellite solar-induced chlorophyll fluorescence. *Remote Sensing*, 11(4), 2019.

[205] Y-G. Zhu and E. Smolders. Plant uptake of radiocaesium: a review of mechanisms, regulation and application. *Journal of Experimental Botany*, 51(351):1635–1645, 10 2000.